Politecnico di Torino

ScuDo
Scuola di Dottorato ~ Doctoral School
WHAT YOU ARE, TAKES YOU FAR

Doctoral Dissertation
Doctoral Program in Civil Engineering (34^{th}cycle)

A novel methodology for the evaluation of low temperature failure properties of asphalt binders

The Monotonic Torsional Loading (MTL) test

Chiara Tozzi
******

Supervisors:
Prof. Orazio Baglieri, Supervisor
Prof. Davide Dalmazzo, Co-Supervisor

Politecnico di Torino
2022

Declaration

I hereby declare that, the contents and organization of this dissertation constitute my own original work and does not compromise in any way the rights of third parties, including those relating to the security of personal data.

Chiara Tozzi
2022

* This dissertation is presented in partial fulfillment of the requirements for **Ph.D. degree** in the Graduate School of Politecnico di Torino (ScuDo).

For a successful technology, reality must take precedence over public relations, for Nature cannot be fooled. — Richard P. Feynman

Abstract

Low temperature cracking represents one of the main distress modes affecting flexible pavements, particularly in cold regions. Thermally induced stresses arise inside the mixture, when the temperature decreases, leading the pavement structure to prematurely fail, when exceed the mixture strength. The asphalt binder plays a key role in controlling and preventing the crack initiation and propagation, since its response can change from a ductile to an extremely brittle one, within the temperature range the pavement experiences during its service life. Therefore, a proper selection of the binder, considering low temperature cracking resistance, represents a critical issue to consider for the mix design of the mixtures. The SuperPave Performance Grade (PG), developed during the Strategic Highway Research Project (SHRP), is one of the most used parameter to address low temperature cracking performance of binders. However, the methodology may not be always reliable to represent the materials field performance, in particular for the increasingly new modified binders. In such context, there is the need of a simple and reliable procedure to address the binders failure properties at low temperatures, both in terms of strength and brittleness. A novel methodology, involving the use of the DSR, is proposed in this thesis. The use of the DSR has been limited to high and intermediate temperatures during the SHRP project, due to the arise of significant compliance errors for low temperatures. This limitation was recently overcome for linear viscoelastic measurements by the introduction of a new measurement system of 4 mm diameter. The Monotonic Torsional Loading (MTL) test proposed in this research project aims to extend the use of the 4 mm DSR to the high strain domain, leading the specimen to its failure point. A cylindrical specimen, designed to be higher than the standard geometry to reduce the torsional stiffness, is subjected to a torsional load, which increases monotonically at a fixed strain rate until failure, while the temperature is kept constant. A simple parameter was proposed to synthetically characterize each material in terms of brittleness, for a selected combination of temperature and strain rate, allowing to determine a representative cracking temperature. The methodology developed was successfully applied to characterize a set of unaged binders, three unmodified and one SBS-modified. The same materials were, subsequently, characterized through the Local Fracture Test (LFT) methodology, which involves subjecting a thin film of asphalt binder placed between two steel protuberances to a tensile load, applying a constant displacement rate, until failure. The LFT results were compared to the MTL results, showing that the two procedures lead to the same results in terms of materials ranking for thermal cracking performance. Even though further investigations on the proposed protocol are certainly needed, it appears to be a promising methodology to characterize binders at low temperatures through easy and short laboratory testing.

Preface

Low temperature (or thermal) cracking represents one of the main distress modes affecting flexible pavements built up in cold regions. This distress occurs in the form of the typical regularly spaced transverse cracks, which in some cases (when the crack spacing is smaller than the width of the pavement) are followed by longitudinal cracks that lead to generate block patterns. The presence of the cracks undermines the structural integrity of the pavement, creating pathways for the intrusion of water into the lower layers, with consequent detrimental effects associated to moisture damage [1, 2]. In general, the cracking mechanism is a function of several factors that are material-, structure-, and environment-related. It has been widely observed that low temperature properties of the asphalt binder play a major role in controlling and preventing crack initiation and propagation, since the material appears highly sensitive to temperature [3, 4]. In fact, the material response can change, when the temperature is decreased, from a ductile to an elastic extremely brittle one, within the temperature range of applications in road pavements. Thermally induced stresses can be dissipated when the binder is soft enough to be capable of stress relaxation through viscous flow; whereas they may lead to crack more likely if the material becomes stiffer, since it reduces its capability to relax stresses. The selection of the binder with an adequate low temperature cracking resistance is then a critical issue in the mix design of asphalt mixtures. The low limiting Performance Grade (PG) temperature [5], embodied in the SuperPave grading system, is one of the most used parameter to address low temperature cracking performance of binders. Such an approach, was proposed during the Strategic Highway Research Project (SHRP) as an alternative to the empirical Penetration Grade (PEN) [6]. The low temperature PG is based on the binder creep properties, determined through the Bending Beam Rheometer (BBR) 3-point bending creep test. The criteria adopted entail the determination of the creep stiffness ($S(t)$) and the creep rate ($m-value$) at a predefined loading time. Specific thresholds are imposed to both these parameters to ensure the binder to show a sufficiently low stiffness along with a high relaxation capability. However, the methodology may not always be reliable to address low temperature thermal cracking performance, in particular with the increasing use of modified binders. In fact, it has been shown that some materials with the same low limiting PG temperature may exhibit significant differences in terms of actual performance in the field [7]. This can be mostly addressed to the fact that the BBR test is not a failure test and the indirect prediction of cracking resistance from the LVE response may be inaccurate, in particular for modified binders, for which the stiffness is not equivalent to the brittleness. In addition, some minor experimental issues can be also highlighted. The standard BBR instrument can be used to run only the predefined creep tests since the load cannot be modified or increased

during the test. The experimental testing procedure requires a lot of efforts, in particular for the specimen preparation, due to the high sensitivity of the binder to the temperature and a lot of material is needed to prepare the specimens. These issues can be overcome with the recently proposed extended use of the Dynamic Shear Rheometer (DSR) for low temperatures, by the introduction of a new measurement system with a smaller diameter of 4 mm [8]. This approach has been successfully used in several studies [9, 10, 11, 12] and a strong correspondence was observed with the BBR results [13, 14]. The DSR is a convenient, versatile and easy-to-use device which requires a very little amount of material. Furthermore, it is already adopted to characterize the LVE properties of binders for high and intermediate temperatures. However, also DSR measurements remain within the LVE domain, without leading the specimen to fail and for the purpose, several alternative test methods have been proposed by researchers. The Asphalt Binder Cracking Device (ABCD) [15] was developed to determine binders fracture strength. A thin film of binder is placed outside a metal ring and inserted into a conditioning chamber, used to decrease the temperature under controlled conditions. As the system is cooled, the differential thermal contraction between the binder and the ABCD ring results in the development of thermal stresses that, increasing until the material's strength, lead the sample to fail. The Local Fracture Test (LFT) [16] was also studied to evaluate crack initiation and growth of asphalt binders in thin film. Two steel protuberances are used to simulate aggregates and a film of material is placed between them. The specimen is then pulled using a fixed displacement rate, for a constant test temperature. The fracture energy can be determined for each test. The Double Edge Notched Tension (DENT) test [17] and the Single Edge Notched Beam (SENB) test [18] were proposed based on fracture mechanics principles. Both tests involve the determination of the binders fracture toughness by leading a cracked specimen to fail and they differ in terms of specimen geometry and test equipment. The DENT test entails the use of the Direct Tension (DT) equipment to subject a dog-bone cracked specimen to tensile load until failure. The SENB test requires the use of a modified BBR device, which allows to increase the load on a notched beam until failure. All of these methodologies may represent a successful alternative to the current specifications and have shown promising results. In particular, the use of fracture mechanics seems to be a powerful tool to address the material resistance to crack propagation. However, it has to highlight that all of these methodologies require specific equipments to be performed, which may imply an increase in experimental complexity. In such context, it is clear that there is a need for a simple and reliable procedure to address the binders failure properties at low temperatures, both in terms of strength and brittleness. A novel methodology based on the use of the DSR, is proposed in this thesis. The procedure involves to subject a cylindrical specimen, 5 mm high to a Monotonic Torsional Load (thus MTL test) until failure. The core idea was to address the failure shear strength and the corresponding brittleness, under carefully controlled temperature conditions, by making use of a simple testing procedure and of an equipment already widely used for binders characterization. The objectives of this research study are summarized as follows:

- develop a novel experimental protocol, to test asphalt binders at low temperatures until failure, by means of the DSR;

- propose a modelling approach, that allows to analyse the experimental output and characterize each material in a reliable way, using a simple and synthetic index;
- apply the proposed methodology to a set of binders;
- compare the results obtained with an other existing approach addressing binders failure properties at low temperatures.

Thesis outline

The thesis is divided into three main parts, following the research approach adopted: (1) introductory concepts, (2) development of the methodology and (3) comparative analysis of results.
Part I refers to the theoretical background and literature review needed for the thesis discussion which could potentially include a multitude of topics. For the sake of simplicity, two chapter has been structured. Chapter 1 focuses on the characterization of asphalt binders failure properties at low temperatures, including the current specifications and the newly proposed methodologies. Chapter 2 discusses briefly the theoretical aspects related to the linear viscoelastic response, giving the proper background to the modelling part.
Part II treats the development of the Monotonic Torsional Loading (MTL) test, describing the experimental procedure and the modelling approach proposed. Several attempts have been made to define the procedure, and only the final version is reported. Chapter 3 deals with the development of the experimental protocol through a preliminary investigation involving four unaged binders, three of which unmodified and one SBS modified. The experimental results are analysed and discussed, using a novel modelling approach in Chapter 4, which allows the determination of a critical temperature characterizing each material. Chapter 5 reports the experimental investigation designed to statistically analyse the test results and to estimate a preliminary test precision in terms of repeatability. Chapter 6 discusses a first application of the proposed MTL methodology, to address low temperature failure properties of a set of aged binders, both in their short- and long-term ageing state.
Part III is dedicated to the work carried out in collaboration with the "Université Gustave Eiffel" of Nantes (FR), supervised by prof. Ferhat Hammoum. The scope of the collaboration was to compare the MTL test procedure with the Local Fracture Test (LFT), developed in the Department of Materials and Structures of the Université Gustave Eiffel. Chapter 7 reports the experimental investigation carried out, involving materials and test methods. The following analysis of results is separated into two chapter. Chapter 8 refers to the numerical model needed for the data analysis. The model was built using the Finite Element Method (FEM), through the software FREEFEM++ [19]. The chapter describes in details how the model was built, in terms of geometry and mesh, materials properties, load and boundary conditions and problem formulation. Chapter 9 reports the LFT results and describes the corresponding analysis to determine for each material investigated a critical parameter. Lastly, the results coming from the LFT methodology are compared with that resulting from MTL approach.
The thesis ends with the conclusions, summarizing the main goals achieved through the research activity and reporting final remarks for future studies.

Contents

Part I

Introductory concepts

Preamble

This part I focuses on the theoretical background and literature review needed to develop the thesis discussion. The objective of this study is to develop a novel procedure for the low temperature characterization of asphalt binders at failure, both involving experimental procedures and analysis of results. Therefore, the first chapter provides an overview of the low temperature response of asphalt binders and how it is evaluated from laboratory measurements. To summarize the state of art, both current specifications and newly proposed test methods are included. The second chapter discusses the main theoretical aspects of linear viscoelasticity and aims to be a brief and concise introduction to the analysis of results and not a detailed theoretical description. For the purpose, mainly linear viscoelasticity is discussed and some assumption have been considered.

Chapter 1

Low temperature response of asphalt binders

The response of asphalt binders to external solicitation is extremely dependent on temperature. At low temperatures (i.e. temperatures below 0 °C), the material shows, in general, a solid-like, high stiffness, glassy response, loosing its capability to dissipate stresses as the temperature decreases. Consider to subject a sample of bitumen to a monotonic shear strain, increasing with a constant rate, selecting a constant temperature within the range of low temperatures. The general response is similar to that shown in the stress-strain space of Fig. 1.1. As can be observed, the stress increases, according to the material's constitutive laws, until a certain point for which the first crack appears. The processes of crack initiation and propagation until separation is referred to as *fracture* and the completely fractured state as *rupture*. The behaviour is, in general, viscoelastic, even at very low temperatures and, depending on the level of strain, is differentiated into linear viscoelastic (LVE) and non-linear viscoelastic (NLVE). The linearity limit can be easily detected experimentally, since the response starts to be dependent on the level of strain applied. The continuum mechanics is used to describe the response, since the body is considered as a continuum. For a certain level of strain damage may occur, defined as the onset of micro defects in the uncracked body. The continuum damage mechanics deals with the response of the damaged body until crack initiation, since the damage is assumed to be homogeneous inside the specimen, such that the body can treated as a continuum having a reduced stiffness. Therefore, a reduction of the modulus is observed experimentally as the strain increases, similarly to the NLVE. This led the experimental identification of the occurrence of damage to be not so easy and specific laboratory equipments are needed for the purpose, such as acoustic emissions. The fracture mechanics focuses on the evaluation of crack propagation inside the sample and the experimental testing typically involves to load a pre-cracked specimen until rupture.

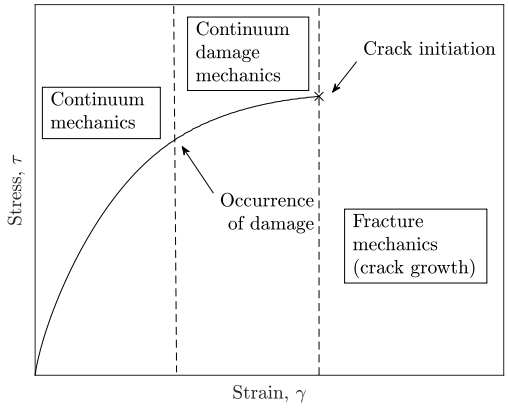

Figure 1.1 Schematic stress-strain curve and theoretical approaches

Certain definitions can be drawn up, based on the general description of Fig. 1.1. The material *strength* defines its capability to withstand stresses and is therefore equal to the maximum stress reached before fracture. On the other hand, the corresponding maximum strain stands out the material *ductility*, that represents its ability to deform before rupture. The deformation energy per unit volume, calculated as the area under the stress/strain curve until the failure point, represents the *toughness*. The terms *brittle* and *ductile* are used to address the condition of low or high energy absorbed before rupture, respectively, and are linked to the material's toughness. Fig. 1.2 shows different three responses, ranging from A, high-stiffness, brittle material, to C, relatively soft and ductile material. It can be observed that the toughness is, in general, linked to the strength, such that it increases as the strength decreases.

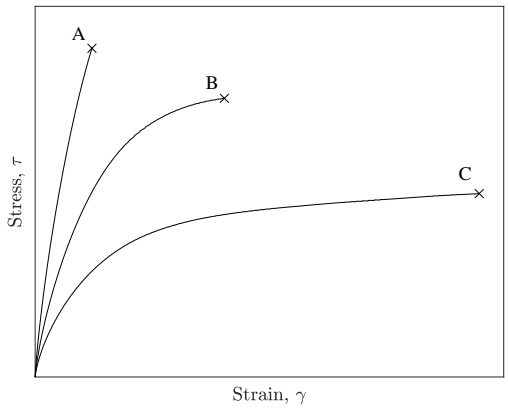

Figure 1.2 Stress-strain curves for different strength levels

1.1 Current specifications

Asphalt binders are traditionally graded using the Penetration Grade (PEN), an index based on empirical parameters [6]. Regarding low temperatures, the Fraass breaking point test [20] is used

to address the material's brittleness. The test requires to subject a film of bitumen to a cycle of bending and stretching load, at a uniform rate of $1\,s^{-1}$, while the temperature is decreased, with a cooling rate equal to $1\,°C\,min^{-1}$. The Fraass temperature is defined as the temperature for which the first crack appears. Even though the methodology has been widely used worldwide, it presents several limitations mostly deriving from the empirical nature of the parameters adopted. In particular, a poor correlation has been observed between the Fraass temperature of the binder and the low temperature performance of the corresponding mix [21].
The SuperPave grading system for asphalt binders was developed as an alternative to the empirical PEN, in the context of the Strategic Highway Research Program (SHRP), a five-year research project, approved in 1987 in the United States, aiming to develop and evaluate techniques and technologies to improve the nation's highways performance, durability, safety and efficiency. The grading system entails the determination of a Performance Grade (PG) [5], for each binder, defining a temperature range over which the material guarantee a prescribed performance. The nature of this approach is not anymore empirical, since the requirements entail with actual material's properties. The low temperature PG [22] is determined based on the results of 3 point bending creep tests performed using the Bending Beam Rheometer (BBR), shown in Fig. 1.3a. The test involves subjecting an asphalt binder beam to a constant load and measuring the corresponding vertical deflection as a function of time [23]. The specimen is prepared by pouring the pre-heated material inside the steel mould, as shown in Fig. 1.3b. The beam is conditioned for 1 h before the load is started, to reach its thermal equilibrium without inducing physical hardening effects. The requirements entail the determination of the stiffness $S(t)$, defined as the inverse of the creep compliance $D(t)$, and the creep rate $m-value$, at a predefined loading time fixed to 60 s. The $S(t)$ has to be lower than 300 MPa and the $m-value$ greater than 0.3, in order to ensure a sufficiently low stiffness along with a high relaxation capability of the material within the range of temperatures prescribed by the PG. The selected loading time comes from the assumption that the creep properties of the mixture after 2 h of loading time, presents a good correlation with the effects of thermal cracking in the field [24, 25]. The assumption was extended to the creep properties of the binders and to reduce the loading time to 60 s the time–temperature superposition principle (TTSP) was adopted. The 2 h properties are then inferred from 60 s tests, increasing the test temperature of 10 °C. The Direct Tension (DT) test is additionally used if the binder does not meet the stiffness requirement and the $S(60\,s)$ ranges between 300 MPa and 600 MPa. However, the $m-value$ requirement must be always satisfied. The Direct Tension Tester (DTT) [26] is used to perform uniaxial tension tests on a dog-bone shaped specimen of asphalt binder, using a fixed strain rate of $1\,mm\,min^{-1}$ while the temperature is kept constant. The limiting value prescribed for the strain at failure is 1 %. The temperature shift of 10 °C is applied also for DT tests. However, the testing equipment is expensive and the complex sample preparation leads to low repeatability of the results and therefore the test is kept optional in the PG specifications [27, 28, 29].

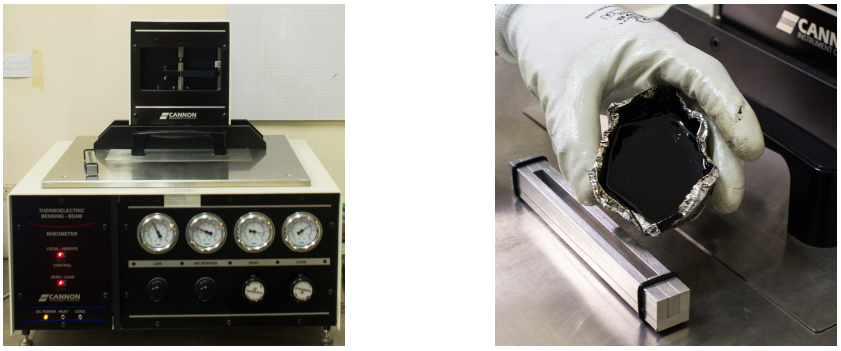

(a) Equipment (b) Asphalt binder beam

Figure 1.3 Bending beam rheometer

Even though this approach have been largely used worldwide several limitations have been highlighted by researchers, who observed that the PG grading not always is capable to differentiate asphalt binders in terms of cracking performance [30, 31]. The methodology was developed based on data concerning unmodified binders and correlates the LVE creep stiffness with the materials brittleness. This correspondence between stiffness and brittleness is not always effective for modified binders, which may behave as ductile even showing higher values of stiffness compared to the unmodified binders. Physical hardening effects are not included in the specifications, to reduce the experimental complexity, even though it has been shown to affect significantly the pavement performance [32, 33]. Several drawbacks were also highlighted about the use of the TTSP to use the 60 s loading test to represent 2 h properties by increasing the temperature of 10 °C [34, 35].
The use of the BBR has been recently re-considered following the introduction of a new measurement system for the Dynamic Shear Rheometer (DSR), proposed by the Western Research Institute (WRI) [8]. The DSR, shown in Fig. 1.4a, is the device used to characterize the LVE properties of asphalt binders for high and intermediate temperatures, upon which the high temperature PG is determined. It was excluded for low temperatures specifications since, during the SHRP, significant compliance errors were recognised for measurements below 5 °C. The new measurement system of smaller diameter of 4 mm, shown in Fig. 1.4b, coupled with the correction model proposed by Schröter [36], allows to use the DSR for measurements as low as −40 °C. The extended use of the DSR, as an alternative of the BBR, presents several advantages, mostly related to the small amount of material required for testing (each BBR beam requires about 5 g, whereas 4 mm DSR only about 0.15 g. This approach has been successfully used in several studies [9, 10, 11, 12] and a strong correspondence was observed with the BBR results [13, 14]. However, the method is still under testing for specifications. Even though experimental advantages, also the DSR tests focuses on small strain domain, that means that the material is tested far from its failure conditions.

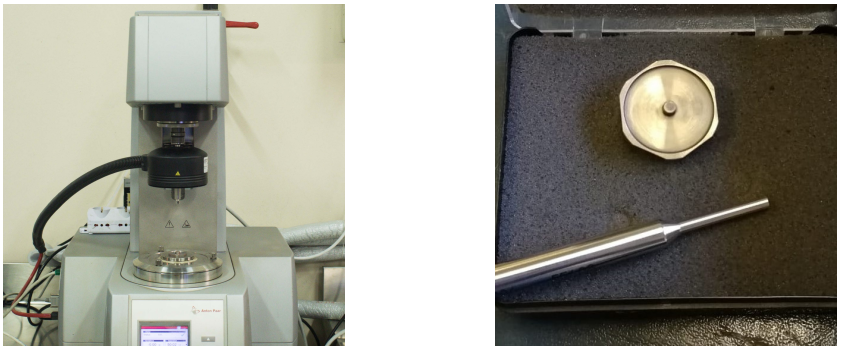

(a) Equipment (b) 4 mm parallel plates

Figure 1.4 Dynamic shear rheometer

1.2 Alternative test methods to characterize failure properties

The limitations highlighted for the current specifications led researchers to propose several alternative test methods, addressing low temperature *single-load fracture* of asphalt binders. The term single-load fracture is referred to define tests involving an increasing monotonic load leading the material to fail, thereby differentiating from fatigue. In general, the proposed tests are based upon two different theories: (1) continuum mechanics and (2) fracture mechanics.
The continuum mechanics theory assumes the body to be continuum, which is translated experimentally by testing an uncracked specimen hypothesising the material as homogeneous. The single-load fracture is originated wherever the local stress (load per unit of cross-sectional area) first exceeds the local strength. The assumption of continuum requires the imperfections of the real material hypothesised homogeneous (cracks and flaws) to be small enough to not affect the failure mechanism. In fact, the presence of defects would reduce the strength of the body by inducing a local stress concentration that would led the specimen to fail before reaching its maximum strength. Therefore, the experimentally assessed strength would be lower than its theoretical estimate. This difference is particularly significant for brittle materials, due to the high sensitivity to stress concentration. The crack morphology is a function of the stress distribution deriving from the type of loading selecting for testing and of the material brittleness. Considering the basic types of loading (pure tension, compression and torsion) and the simplest cylindrical geometry, the resulting stress distributions are shown in Fig. 1.5. When the specimen is subjected to tensile forces, the tensile stress component is axial and the compressive stress component transverse. The shear stresses are then angled at 45° with respect to the principal components. If the material behaves as ductile, the internal structure deforms permanently, causing lateral deformations (necking) prior to the fracture, which appears at the centre of the shaft. On the other hand, a brittle response leads the specimen to fail with little or no deformation, with the fracture likewise occurring at the centre of the specimen. When the shaft is subjected to an axial compression, the stress distribution is the reverse of the tensile case: the compressive component is axial and the tensile component is transverse. The shear stresses are again angled at 45° with respect to the cylinder axis. In such condition, a ductile behaviour leads the specimen to become shorter and thicker, without fracturing. A brittle response instead, implies the shaft to

fail perpendicularly to the maximum tensile stress component, which is transverse. Lastly, in the case of pure torsion, the stress system rotates of 45° in one direction, with respect to the cylinder axis, depending on the direction of twisting. The stress system of pure torsion is then equivalent to tensile and compressive stresses acting on the element inclined 45° with respect to the axis. The stress results to be maximum at the surface of the cylinder and zero at the centre. A ductile failure would be on the plane transverse with respect to the axis, in general at the centre of the shaft, such as the cylinder would be composed by an infinite number of infinitely thin disks, that slip a very small amount with respect to the neighbouring disk, not changing its diameter. A brittle material, instead, fractures againg in a plane perpendicular to the tensile stress component, which is angled 45° to the axis. The result is typical 45° crack, characterizing brittle failure in torsion.

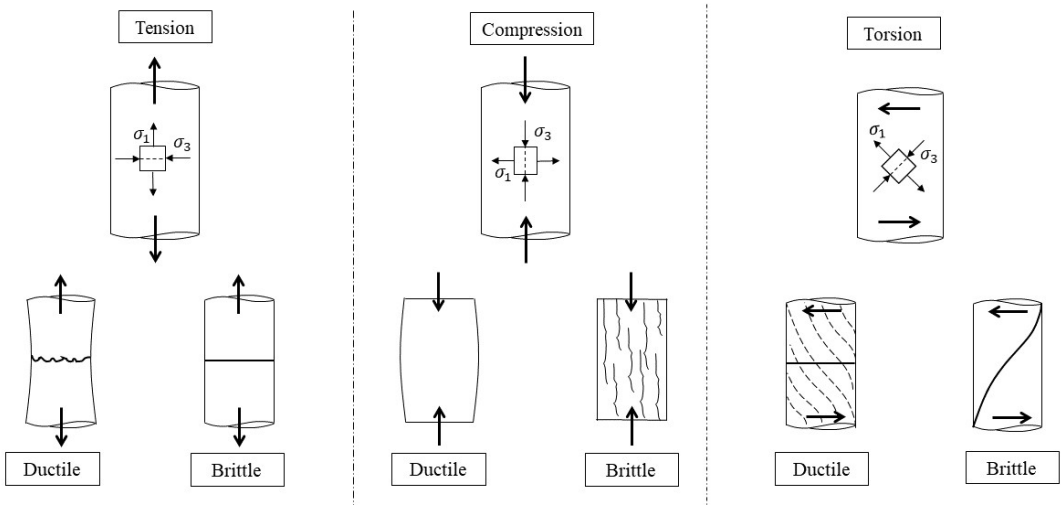

Figure 1.5 Orientation of normal components and single-load failure of a rod under pure tension, compression and torsion (adapted from [37])

In general, asphalt binders behave both as ductile and brittle materials, depending on several factors. Table 1.1, adapted from that drafted by D.J. Wulpi for metals [37], summarizes the main aspects affecting the asphalt binders response at failure. On of the most significant variables to consider is obviously the temperature, since as already repeatedly mentioned, the binder behaves as ductile for high temperatures and as brittle at low temperatures. The equivalent effects can be observed by varying the pressure instead of temperature. The loading time, as derived from the TTSP, produces the inverse effect of the change in temperature or pressure: lower rates of loading promote a ductile-like response and higher rates of loading a brittle-like response. The ductile-brittle transition is also dependent on specimen geometry and size due to stress concentration deriving from the presence of internal defects. A thicker section usually is more likely to behave as brittle, since there is a higher probability that stress concentrations are present. Considering instead the type of loading, the same specimen subjected to torsional loading tends to behave in a more ductile manner than the same specimen loaded in tension or compression.

Table 1.1 Factors affecting the ductile-brittle behaviour [37]

	Trend	
Factor	**Ductile**	**Brittle**
Temperature	Higher	Lower
Pressure	Higher	Lower
Rate of loading	Lower	Higher
Geometry and size	Smaller or thinner	Larger or thicker
Type of loading	Torsion	Tension or compression

Following the continuum mechanics approach, several test methods have been proposed concerning asphalt binders.
The BBR strength test [38] was developed in 2012. The test is performed using a modified BBR device, which allows to increase the load at constant rate, until the specimen fails. Therefore, the asphalt binder beam is led to fail using the BBR equipment, and outcomes are the load at failure and the corresponding recorded deflection, for the selected test temperature.
The Asphalt Binder Cracking Device (ABCD) was proposed in 2007 [15], to characterize the binders strength, in response to thermal stresses. The specimen is formed by pouring the material into a circular mould, with an internal metal ring. The whole system is placed in a conditioning chamber and the temperature is decreased using a fixed cooling rate. The specimen cracks when the thermal stresses, arising from the different thermal contractions between the metal ring and the binder as the temperature is decreased, exceed the material's strength. The device records the cracking temperature and the corresponding binder strength, calculated indirectly from the strain at failure.
The Local Fracture Test (LFT) [16] is a specific test addressing crack initiation and growth inside a thin film of asphalt binder, placed between two steel protuberances. The device is designed to simulate the response of the material inside the mixture, since the two protuberances should simulate the aggregates. The film is pulled in traction, at constant temperature and strain rate, selected properly to investigate the brittle response of the binder. The resulting fracture energy is assessed through the force-displacement curve recorded during the test.
Fracture mechanics-based test methods, were not involved in the PG specifications due to their theoretical and experimental complexity. However, they have been recently re-considered due to the limits of the current specifications since allow to characterize the material response to crack propagation. In general, the experimental procedure involves a notched specimen, of standard geometry, to be subjected to an increasing monotonic load until failure. The Linear Elastic Fracture Mechanics (LEFM) is valid under the assumption of linear elasticity. Subsequent works on fracture research incorporated other material behaviour, such non-linear time-independent and -dependent response, allowing to proper describe elasto-plastic, viscoelastic, viscoplastic responses and dynamic fracture. Regarding asphalt binders, the LEFM is typically applied considering the response as elastic at low temperatures and neglecting the effect of the time-dependency, for the sake of theoretical simplicity. The test results are in general expressed as fracture energy (labelled as $\mathscr{G}$ for LEFM) or using the stress intensity factor (K_I for mode I

fracture of opening), both indicating the material's *fracture toughness* (i.e. its ability to resist to crack propagation). The energy approach states that fracture occurs when the energy available for crack growth is sufficient to overcome the resistance of the material. Griffith [39] was the first to propose this approach, following the analysis of Inglis [40] on elliptical holes in flat plates. The energy release rate $\mathscr{G}$ is defined as "the rate of change in potential energy with crack area for linear elastic materials, and is expressed as

$$\mathscr{G} = \frac{\pi\sigma^2 a}{E} \tag{1.1}$$

where E is the Young's modulus, σ is the applied stress and a is half of the crack length. The energy $\mathscr{G}$ is the driving force for fracture and its critical value $\mathscr{G}_C$, recorded when the specimen fails, is the material resistance. The other methodology to characterize fracture toughness is the stress intensity approach. The stress intensity factor K_I is given by

$$K_I = \sigma\sqrt{\pi a} \tag{1.2}$$

and reaches the critical value K_{IC} when fracture occurs. In this case, the driving force for fracture is represented by K_I and K_{IC} is the measure of material resistance.
The energy and the stress intensity approach are equivalent for linear elastic fracture mechanics (LEFM), since comparing Eqs. 1.1 and 1.2 the following relation can be written:

$$\mathscr{G} = \frac{K_I^2}{E}. \tag{1.3}$$

The majority of fracture toughness tests have several common features, such the specimen geometry. The fundamental assumption of the theoretical discussion is the independency of the fracture toughness on size and geometry and since the laboratory testing has to deal with finite specimen size, some standard geometries has to be adopted.
The most known test methods regarding asphalt binders are: (1) the Single Edge Notched Beam (SENB) [18, 41, 42, 43] test and (2) the Double Edge Notch Tension (DENT) test [44, 17].
The SENB test is a 3-pt bending test on a notched beam of prescribed dimensions shown in Fig. 1.6, performed using the BBR modified to be able to increase the load. The procedure of testing and analysis is based on the ASTM E399 standard [45].

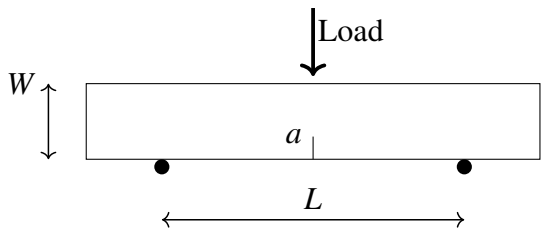

Figure 1.6 Single Edge Notched Beam test geometry

The DENT test involves testing a pre-cracked specimen by means of the DTT equipment. The specimen geometry is illustrated in Fig. 1.7.

All of these methodologies may represent an alternative to the current specifications, having shown promising results. In particular, the use of fracture mechanics seems to be a powerful tool to address thermal cracking performance of asphalt binders, since it allows to evaluate the material resistance to crack propagation. However, it has to be highlighted that all of these test methods proposed require specific equipments to be performed, leading in some cases to loose experimental simplicity.

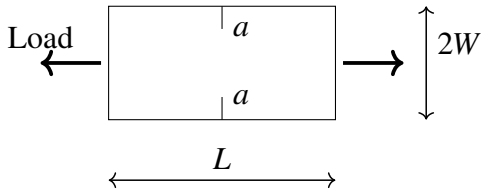

Figure 1.7 Double Edge Notch Tension test geometry

1.3 Glass transition

The glass transition is defined as a "reversible change from (or to) a viscous state to (or from) a hard and brittle one" [46] and concerns amorphous materials, such as asphalt binders. The change in the thermodynamic state of the material, which occurs when the glass transition is traversed, affects all the mechanical properties thermo-dependent and therefore represents an important parameter to consider in discussing the low temperature response of binders. The glass transition mechanism is linked to the molecular rearrangements that the material, in its viscous state, experience when the equilibrium is perturbed by an external solicitation. In this situation, if the time scale of the external solicitation is greater than the time needed to re-establish the equilibrium, the molecules appear "frozen", leading the material to show the properties of a solid [47]. This non-equilibrium state is *metastable* and the volume, the enthalpy and the entropy are greater than they would be in the equilibrium state. When the temperature is decreased, the structural equilibrium is perturbed, and an external time scale is introduced through the corresponding cooling rate. Therefore, if the temperature rate is greater than the time the material needs to establish the equilibrium, it experiences the transition. The temperature range over which this happens is inevitably time-dependent and is represented by the *glass transition temperature* T_g.

The laboratory determination of the T_g stems on arbitrary conventions since, as mentioned, it is strongly dependent on the experimental time scale. Therefore, the assessed T_g is associated to a time domain, selected based on experimental practical limits. Regarding asphalt binders, there are no standard methods to determine the T_g and therefore procedures similar to those used for polymers are generally adopted. Three main approaches are used: (1) the Differential Scanning Calorimetry standard (DSC) or Modulated (MDSC), (2) the Dynamic Mechanical Analysis (DMA) and (3) the Thermo-Mechanical Analysis (TMA). For the sake of simplicity, the corresponding temperatures are labelled as (1) $T_{g,DSC}$ or $T_{g,MDSC}$, (2) $T_{g,DMA}$ and (3) $T_{g,TMA}$. The DSC technique involves recording the differential heat flow of the tested material as a function of temperature, using a predetermined temperature history. Fig. 1.8a shows a typical

DSC curve and the corresponding $T_{g,DSC}$, detected as the stepwise drop in the heat capacity of the material. Two temperatures can be defined as $T_{g,DSC}$: the midpoint temperature and the temperature corresponding to the inflection point of the curve (labelled T_m and T_i respectively). The MDSC was developed as an extension of the DSC [48], to overcome some limitations of the DSC technique that lead, in some cases, to a complicate interpretation of the results. In fact, the temperature range of different types of material transition may overlap in the DSC curve, requiring experience to assist the interpretation of results. The MDSC procedure involves two simultaneous heating rates: (1) a linear heating rate and (2) a sinusoidal or modulated heating rate. The total heat flow signal, containing the same information of standard DSC, is separated through Fourier transformation analysis into reversing and non-reversing heat flow curves [49]. In general, this allows to increase sensitivity, resolution and the ability to separate multiple thermal events. Since asphalt binders are very complicated systems, consisting in a broad range of chemical groups, they show a DSC scan much more difficult to analyse due to the aforementioned superposition of thermal transitions [50]. For this reason, the MDSC appears to be a better technique for binders to detect the glass transition.

The $T_{g,DMA}$ is determined as the temperature corresponding to the peak of the loss modulus G", for a fixed frequency, as shown in Fig. 1.8b. The methodology allows a straightforward determination of the T_g, based on few and simple tests. However, the resulting temperature is strongly linked to the frequency and the cooling/heating rate selected for the measure. Some studies, such as that published by M.Elwardany et al. [51], have shown a high correlation between the $T_{g,MDSC}$ and the $T_{g,DMA}$ for asphalt binders, assessed using prescribed experimental procedures. However, the two temperatures refer to different aspects associated to the glass transition and they are not supposed to be correlated [47].

Methods based on TMA involves measuring the volume reduction of a stress-free sample subjected to certain cooling/heating rate. The volume reduction curve, as shown in Fig. 1.8c, results to be linear until a certain point for which deviates. This deviation arise when the configurational rearrangements, needed to maintain the internal structural equilibrium, cannot be accomplished within the experimental time. The material experiences then the glass transition and the corresponding time-dependent $T_{g,TMA}$ is assessed as the interception point between the extrapolated equilibrium line and the line fitting the new glassy state, as shown in Fig. 1.8c. Regarding asphalt binders, the experimental determination of the volume reduction curve is commonly performed through dilatometry, following the procedure proposed by Bahia and Anderson [52]. An alternative procedure was recently proposed by Santagata et al. [53], involving the use of the 4 mm DSR. The methodology is based on the assumption that the volume contraction is proportional to the high reduction. Therefore, the volume reduction curve can be inferred indirectly by measuring the reduction of height as the temperature decreases.

In general, as already mentioned, all of the temperatures assessed, regardless the technique used, differ from each other. This difference reflects the arbitrary nature of the T_g definition and its strong dependent upon the experimental conditions selected for testing.

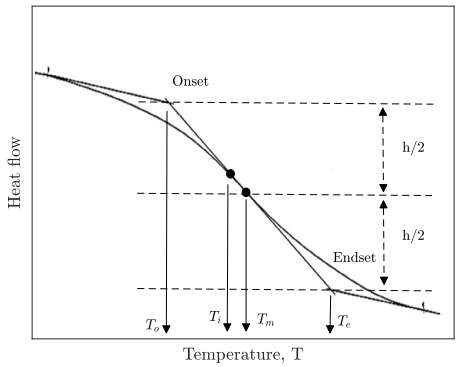

(a) Differential scanning calorimetry DSC

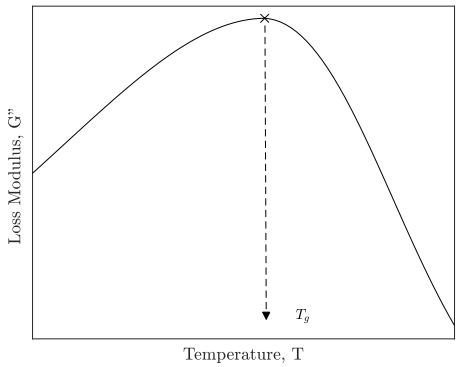

(b) Dynamic mechanical analysis DMA

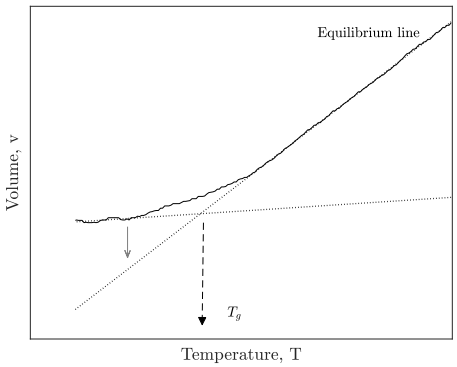

(c) Thermo-mechanical analysis TMA

Figure 1.8 Determination of the glass transition temperature T_g

1.4 Physical Hardening

Physical hardening of asphalt binders is a time and temperature-dependent ageing process that has a significant influence on the long-term performance of flexible pavements. The phenomenon is not included in the binders specifications and it was observed to be one of the causes of premature failure of pavements [54, 32]. The material, when stored isothermally at temperatures below the room temperature, undergoes to a thermo-reversible ageing, becoming stiffer and more brittle. Although the phenomenon was firstly reported for asphalt binders by Struik [55], who referred to as *physical ageing*, the first comprehensive study on it refers to the SHRP [56]. During the SHRP, the phenomenon was termed *physical hardening*, in order to be clearly differentiated from chemical ageing, commonly known simply as ageing in asphalt binders literature. The ageing mechanism can be explained using the "free volume theory" [55], which regards the total volume of the material as composed by a fraction of occupied volume and a fraction of free volume. The free volume fraction tends to decrease, when the temperature is lowered, due to configurational rearrangements. Simultaneously, the particle mobility decreases and, for a certain temperature, it becomes so small that the reduction in free volume cannot be accomplished in the experimental time. In such condition, the free volume starts to be greater

than it would be at the equilibrium. This non-equilibrium state is unstable and the material, if kept at constant temperature, tends to approach the equilibrium, affecting all those properties which are temperature dependent. The study of Struik addressed the experimental evaluation of this phenomenon by measuring the change in creep properties, when the material is subjected to different storage times and temperatures. The loading time-conditioning time superposition was applied, since the creep curves resulted to be shifted along the loading time scale, meaning that the ageing affects all the relaxation times by the same factor. The same approaches was adopted during the SHRP for asphalt binders, by performing several creep tests using the BBR, at different temperatures and progressively increasing the ageing time. An example of results is shown in Fig. 1.9a. As can be observed, the creep curves result to be shifted along the log loading time axis, validating the applicability of the loading time-ageing time superposition. An example of stiffness master curves obtained selecting a reference ageing time is shown in Fig. 1.9b. The overall study resulted in the BBR specification of testing after 1 and 24 h of conditioning. However, this requirement was not implemented, due to the absence of a simple and short laboratory procedure.

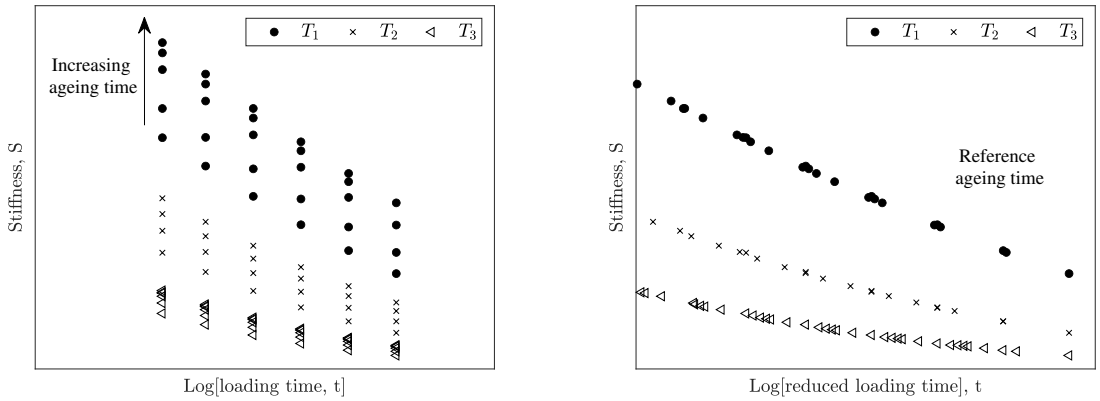

(a) Stiffness curves for different temperatures, as the ageing time increases

(b) Stiffness master curves for different temperatures, at a reference ageing time

Figure 1.9 BBR creep stiffness curves as a function of temperature ($T_1 < T_2 < T_3$) and ageing time

After the SHRP, many researchers have recognized the relevance of physical hardening in evaluating binders low temperature properties. Several studies have been carried out both on binders and mixtures and some of them are here mentioned [57, 33, 58, 59, 60, 13, 61, 62]. Concerning asphalt binders, the general approach entails to quantify the physical hardening effect based on BBR creep testing. The 4 mm DSR was also used by Laukkanen et al. [60] to substitute the BBR. Several parameters have been adopted for the purpose. One method involves referring to the shift factors, resulting from the application of the loading time-ageing time superposition principle to shift the creep curves, obtained at different ageing times, to build a single master curve, selecting a reference conditioning time (usually equal to 1 h). Another simple way to describe the effect physical hardening on asphalt binders is through the Hardening Index (HI), defined as

$$HI = \frac{S(60\,\mathrm{s})_{t_i}}{S(60\,\mathrm{s})_{t_0}} \tag{1.4}$$

where $S(60\,\mathrm{s})_{t_i}$ the 60 s BBR stiffness obtained at the conditioning time t_i and $S(60\,\mathrm{s})_{t_0}$ is the 60 s BBR stiffness determined at the reference conditioning time t_0.
Based on the HI index, the Hardening Rate (HR) was recently proposed by Tabatabaee et al.[62], defined

$$HR = \frac{S(60\,\mathrm{s})_{t_i} - S(60\,\mathrm{s})_{t_0}}{S(60\,\mathrm{s})_{t_0}}. \tag{1.5}$$

The HR was introduced to consider in the analysis the relative change in stiffness due to the isothermal storage. A model has been proposed to describe the HR as a continuous function of ageing time and temperature, which would allow to predict the long-term performance of the binder from simple and relatively short laboratory testing. The model was expressed through the following equations:

$$HR(T,t_i) = \frac{\phi(T)}{G}\left(1 - e^{-t_i\frac{G}{\eta}}\right) \tag{1.6}$$

$$\phi(T) = e^{\frac{-9(T-T_0)^2}{(2x)^2}}, \tag{1.7}$$

in which G and η are the viscoelastic parameters of the mechanical creep model, T_0 is the temperature for which the peak hardening rate is observed and $2x$ is the length of the temperature range in which hardening occurs. Following this methodology, a modified model was proposed by Tozzi et al. [63], to better describe the physical hardening effect both for short and long ageing times. Although the model seems to represent an interesting approach to the issue of laboratory assessment of physical hardening, allowing to predict the hardening effects from relatively short testing, further studies are certainly needed for the validation.

Chapter 2

Linear viscoelastic response

The mechanical response of any solid body subjected to an external input must simultaneously satisfy the conditions of (1) equilibrium, (2) kinematics and (3) material constitution. The first two conditions are applicable to all continuous body, regardless of the material's properties, whereas the third one refers to the material behaviour and is expressed through the *constitutive equations* (or *(rheological) equations of state*). In other words, the constitutive equations express analytically the material response to an external input (force and/or displacement), in a way that is independent of the body geometry (size and shape).
All real materials are in principle *viscoelastic*, meaning that for any mechanical deformation, the energy is not completely stored elastically, but part of it is dissipated by viscous forces. This dissipation leads the mechanical properties to be time-dependent and therefore the response is a function of the input history (indicated using the brackets $\{\}$ as $R = R\{I\}$) and the constitutive equations are expressed through characteristic material functions. The response can be in addition *linear*, when the constitutive equations satisfy the two conditions of (1) homogeneity (or proportionality) and (2) superposition (or Boltzmann superposition principle). The first condition expresses the stress-strain linearity, stating that an increase of the input by a constant factor α, is followed by the same increase in the response:

$$R\{\alpha I\} = \alpha R\{I\} = \alpha I. \tag{2.1}$$

The second condition refers to the time-dependence linearity and requires that the response deriving from multiple input, acting at different time instants, is additive such that

$$R\{I_1 + I_2\} = R\{I_1\} + R\{I_2\}. \tag{2.2}$$

Even though the assumption of linearity is valid under infinitesimally small deformations, in practice it has been observed to be a reliable approach if the deformation remains under a certain limit value (linear limit).
The material response can be considered as time-independent when the time-dependence can be neglected. The response depends then only on the current input (indicated using the brackets $()$ as $R = R(I)$) and the material's functions become constants. Such assumption remains an

approximation since, as mentioned, any real material behaves as viscoelastic.
The chapter is mostly focused on linear viscoelasticity, discussing the theoretical background of this thesis work. For the purpose, some assumptions have been made:

- the theoretical formulation is referred to isothermal and isobaric linear viscoelastic response and the thermo-viscoelasticity is discussed separately in section 2.7;
- the tensorial character of stress and strain is neglected, when not otherwise specified;
- all the equations are referred to the time-dependent shear stress $\tau(t)$ and the corresponding time-dependent shear strain $\gamma(t)$;
- the material is considered as homogeneous and isotropic.

For further reading, several books have been devoted to the subject and those used to draw up this chapter are here mentioned [64, 65, 66].

2.1 Linear elastic constitutive equations

The linear elastic constitutive equations are expressed, in the following general tensorial form:

$$\sigma_{ij} = C_{ijkl}\,\varepsilon_{kl} \tag{2.3}$$

where σ_{ij} and ε_{kl} are the stress and strain tensor respectively and the modulus C_{ijkl} is a tensor of the fourth order. The $3^4 = 81$ components of the modulus can be reduced, considering the tensor symmetry

$$\sigma_{ij} = \sigma_{ji} \qquad\qquad \varepsilon_{kl} = \varepsilon_{lk} \tag{2.4}$$

to 36 independent constants termed *elastic coefficients*.
The coefficients can be further reduced to 2 when the behaviour is isotropic, that means that the properties are identical in all directions. Hence, the stress-strain relation assumes the following form

$$\sigma_{ij} = \lambda\,\varepsilon_{kk}\,\delta_{ij} + 2G\,\varepsilon_{ij} \tag{2.5}$$

where δ_{ij} is the Kronecker's delta and G and λ are the *Lamé constants*. The two *Lamé constants* are defined as

$$G = \frac{E}{2(1+\nu)} \tag{2.6}$$

$$\lambda = \frac{E\,\nu}{(1+\nu)(1-2\,\nu)} = \frac{2G}{1-2\,\nu} \tag{2.7}$$

where G is the modulus of elasticity in shear, E is the elastic modulus (Young's modulus) and ν is the Poisson ratio.
In principle, the Eq. 2.5 can be expressed by means of any combination of two independent

constants and any elastic constant can be expressed as a function of any two others. Considering the modulus E and the ratio ν as constants, the Eq. 2.5 becomes

$$\sigma_{ij} = \frac{E\,\nu}{(1+\nu)(1-2\,\nu)}\,\varepsilon_{kk}\,\delta_{ij} + \frac{E}{(1+\nu)}\,\varepsilon_{ij}, \tag{2.8}$$

or inverting to solve for the strain tensor

$$\varepsilon_{ij} = \frac{1+\nu}{E}\,\sigma_{ij} - \frac{\nu}{E}\,\sigma_{kk}\,\delta_{ij} \tag{2.9}$$

where $1/E = D$ is the stretch (or tensile) compliance and $1/G = J$ is the shear compliance. The Eq. 2.8 represents the generalization, to a general state of stress, of the *Hook's law*, which is written for tensile loading as

$$\sigma = E\,\varepsilon. \tag{2.10}$$

2.2 Linear viscoelastic constitutive equations: integral representation

The integral representation of the LVE constitutive equations, derives from the principle of superposition (Eq. 2.2) and therefore is referred to as *Boltzmann superposition integral*. Consider a constant input I_1 (stress or strain) applied at time $t = \xi_1$, such that

$$I(t) = I_1\,H(t-\xi_1) \tag{2.11}$$

where t is the time of interest and $H(t-\xi_1)$ is the *Heaviside unit step function*. According to Eq. 2.1, the corresponding response is

$$R = R\{I\} = R\{I_1 H(t-\xi_1)\} = I_1\,R\{H(t-\xi_1)\}. \tag{2.12}$$

When the input is a continuous function of time $I(t)$, can be approximated as the sum of $(N+1)$ constant inputs as

$$I(t) = \sum_{i=1}^{N} I_i\,H(t-\xi_i), \tag{2.13}$$

and, similarly to Eq. 2.12 the response is

$$R(t) = \sum_{i=1}^{N} I_i\,R\{H(t-\xi_i)\}. \tag{2.14}$$

The continuos input function (number of intervals tends to infinity) can be solved through the integral representation as

$$R(t) = \int_0^t R\{H(t-\xi)\}\,d\,[I(\xi)]\,. \tag{2.15}$$

The integration variable ξ is always less than or equal to t so that the function $H(t-\xi)$ is always unity in the range of integration. Replacing $d\,[I(\xi)]$ by $[\partial I(\xi)/\partial(\xi)]\,d(\xi)$, the integral can be written as

$$R(t) = \int_0^t R_H(t-\xi)\,\frac{\partial I(\xi)}{\partial(\xi)}\,d(\xi) \tag{2.16}$$

where $R_H(t-\xi)$ represents the material's unit response function, i.e. the response to an excitation of unit amplitude.
The symbols R and I are used to address the generic response and input, respectively, since the formulation does not differ whether we regard stress as the response to a strain excitation or strain as a response to a stress excitation.

2.3 Linear viscoelastic response functions

The integral representation of the constitutive equations reported in section 2.2, does not specify a particular input form and the symbols R and I are used to identify the general response and input, respectively. However, the viscoelasticity implies time-dependency, leading the response to differ based on the excitation selected, since any possible excitation is a function of time. The response is, as aforementioned, described through material characteristic functions, which in the case of linearity, completely describe the behaviour, if known over the entire time domain. In other words, at least in principle, any linear material response function can be converted into any other. For this reason, the laboratory determination of the material LVE response stems on experimental and theoretical simplicity and the most used excitations, referred to as *standard excitations*, are:

1. the step excitation;
2. the harmonic excitation;
3. the slope excitation.

Strictly speaking, the first two excitations are not realizable experimentally, since it not possible neither to apply an instantaneous excitation nor to obtain instantaneously a steady-state sinusoidal excitation. However, it is possible to obtain, in both cases, an experimental approximated excitation that allows to use these simple mathematical forms. In general, independently on the excitation form, the input can be in the form of strain or stress and the corresponding material response functions are defined as *relaxation* and *retardation or creep*. The following discussion does not give mathematical derivations, for the sake of simplicity and for further details, the reader is referred to the books mentioned in the introduction of section 2.
Let the excitation be the strain γ_0, applied at time $t = 0$ and held constant as shown in Fig. 2.1a. The time-dependent stress $\tau(t)$

$$\tau(t) = G(t)\gamma_0 \tag{2.17}$$

where $G(t)$ is the shear relaxation modulus.
Similarly, in the case of an applied stress τ_0, represented in Fig. 2.1b, the time-dependent strain

$\gamma(t)$ is:

$$\gamma(t) = J(t)\tau_0 \tag{2.18}$$

where $J(t)$ is the shear creep compliance.

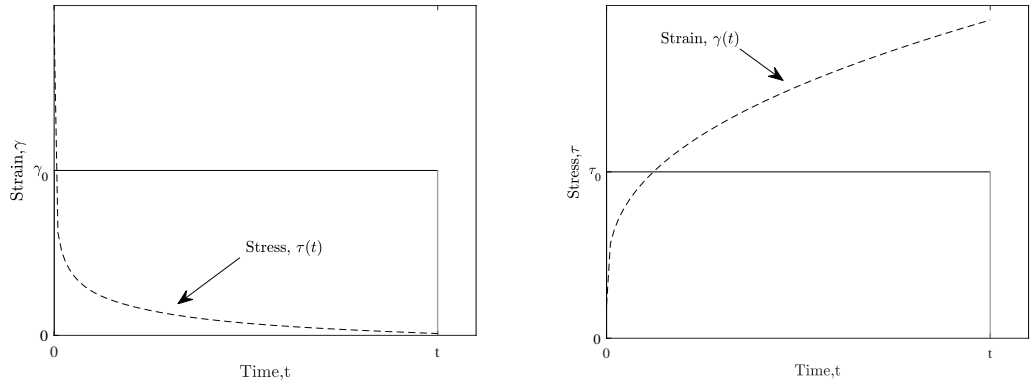

(a) Relaxation (b) Creep

Figure 2.1 Step excitation

The harmonic excitation, also referred to as sinusoidal steady-state or dynamic excitation, is represented in Fig. 2.2.
Let the input be an harmonic strain, analytically represented in the two equivalent forms of

$$\gamma(t) = \gamma_0 sin(\omega t) \qquad \gamma(t) = \gamma_0 cos(\omega t), \tag{2.19}$$

where ω is the constant angular frequency, or considering the generalized complex form as

$$\gamma(t) = \gamma_0 (cos(\omega t) + i sin(\omega t)) = \gamma_0 e^{i\omega t}. \tag{2.20}$$

The steady-state stress response $\tau(\omega)$ is

$$\tau(\omega) = G^*(\omega)\,\gamma(\omega) \tag{2.21}$$

where $G^*(\omega)$ is the complex shear relaxation modulus.
Similarly, considering the generalized stress input

$$\tau(t) = \tau_0 e^{i\omega t}, \tag{2.22}$$

the steady-state strain response $\gamma(\omega)$ is

$$\gamma(\omega) = J^*(\omega)\,\tau(\omega) \tag{2.23}$$

where $J^*(\omega)$ is the complex shear compliance.
Observing Eqs. 2.21 and 2.23, it can be highlighted that the response has the same angular

frequency ω than the harmonic excitation applied.

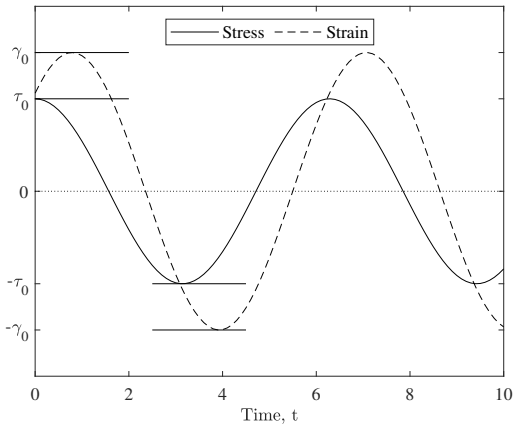

Figure 2.2 Harmonic excitation

The two moduli $G^*(\omega)$ and $J^*(\omega)$ are complex quantities and can be decomposed, as shown in Fig. 2.3, into cartesian and polar components as

$$G^*(\omega) = G'(\omega) + iG''(\omega) = G^*(\omega)\, e^{i\delta(\omega)} \tag{2.24}$$

$$J^*(\omega) = J'(\omega) - iJ''(\omega) = J^*(\omega)\, e^{-i\delta(\omega)} \tag{2.25}$$

where G' and J' are the real components, G'' and J'' are the imaginary components and $\delta(\omega)$ is the *loss angle*.
The terms G' and J' are defined as *storage components* since they are proportional to the average energy stored during a cycle of deformation per unit volume. Conversely, the terms G'' and J'' are defined as *loss components*, since are linked to the energy dissipated during a cycle of deformation per unit volume.
Considering the cartesian space the norm of the complex moduli are

$$|G^*|(\omega) = \sqrt{[G'(\omega)]^2 + [G''(\omega)]^2} \qquad |J^*|(\omega) = \sqrt{[J'(\omega)]^2 + [J''(\omega)]^2} \tag{2.26}$$

and the loss tangent is

$$\tan\delta(\omega) = \frac{G''(\omega)}{G'(\omega)} = \frac{J''(\omega)}{J'(\omega)}. \tag{2.27}$$

On the other hand, considering the polar space the following relations can be derived for the relaxation components

$$G' = |G^*|(\omega)\, cos\delta(\omega) \qquad G'' = |G^*|(\omega)\, sin\delta(\omega) \tag{2.28}$$

and for the creep components

$$J' = |J^*|(\omega)\, cos\delta(\omega) \qquad J'' = |J^*|(\omega)\, sin\delta(\omega). \tag{2.29}$$

The loss angle $\delta(\omega)$ is the phase angle between the sinusoidal steady-state stress and strain. It is always positive since its tangent is the ratio between two moduli (Eq. 2.27) and can range from 0° (purely elastic material) to 90° (purely viscous material). As described in Fig. 2.2, the stress always leads the strain, which is lagged by the phase angle.

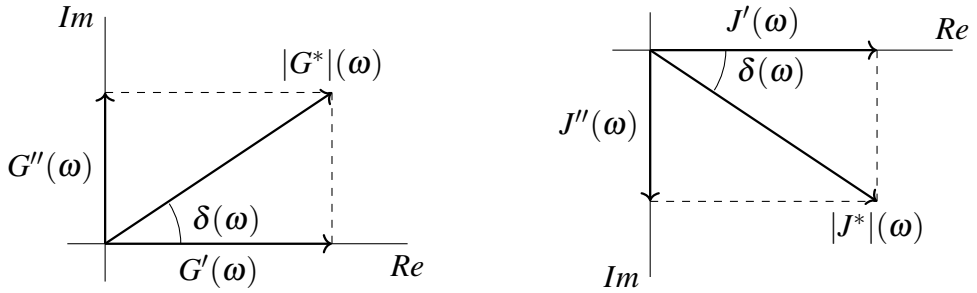

(a) Complex relaxation modulus

(b) Complex creep compliance

Figure 2.3 Real and complex components of the modulus

The slope excitation, represented in Fig. 2.4, involves the imposition of the input (stress or strain) increasing monotonically with a constant rate. In general, it is not used for the laboratory characterization of the linear time-dependent response, since the linear limit can be exceeded quite soon after the excitation is imposed. However, it is included as standard excitation and it is here briefly described. Let the excitation be the strain, expressed as

$$\gamma(t) = \dot{\gamma}_0 t \tag{2.30}$$

where $\dot{\gamma}_0$ is the constant rate of loading. The corresponding response is

$$\eta(t) = \frac{\tau(t)}{\dot{\gamma}_0} = \int_0^t G(u)du \tag{2.31}$$

where $\eta(t)$ is the shear viscosity. Similarly, for the stress excitation

$$\tau(t) = \dot{\tau}_0 t \tag{2.32}$$

where $\dot{\tau}_0$ is the constant rate of loading, the response is

$$\chi(t) = \frac{\gamma(t)}{\dot{\tau}_0} = \int_0^t J(u)du \tag{2.33}$$

where $\chi(t)$ is the inverse of the shear viscosity $\eta(t)$.

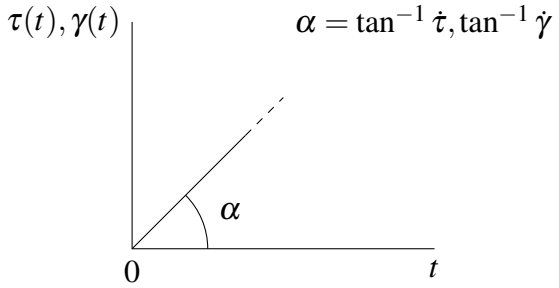

Figure 2.4 Slope excitation

2.4 Theoretical interrelations between linear viscoelastic functions

All linear time-dependent response functions contain, as mentioned, the same information on the material behaviour and therefore, any of these functions can be, at least in principle, converted into any other. The need for interconversion arises mainly for experimental reasons since the test selected has to be short, simple (both from experimental and theoretical point of view) and has to allow to characterize the material in the widest range of time.
Interconversion between the harmonic response functions is simple, since the two moduli G^* and J^* are reciprocal, such that

$$G^*(\omega)J^*(\omega) = 1. \tag{2.34}$$

The following relations can be easily derived considering Eq. 2.34:

$$|J^*|(\omega) = \frac{1}{|G^*|(\omega)} \qquad \tan\delta = \frac{G''(\omega)}{G'(\omega)} = \frac{J''(\omega)}{J'(\omega)}. \tag{2.35}$$

Conversely, the interconversion between the relaxation modulus $G(t)$ and the creep compliance $J(t)$ is much more complex since the two transient moduli are not reciprocal as G^* and J^*. In general, it can be shown that

$$G(t)J(t) \leqq 1, \tag{2.36}$$

with the equality satisfied when $t \to 0$ or ∞ (time-independence).
The theoretical interrelations between the two transient material functions, can be expressed using different form and the Laplace transform is here adopted. Recalling Eq. 2.16, the convolution integral is expressed as

$$\gamma(t) = \int_0^t J(t-\xi)\frac{\partial\tau(\xi)}{\partial(\xi)}d(\xi) \tag{2.37}$$

for a stress excitation and as

$$\tau(t) = \int_0^t G(t-\xi)\frac{\partial\gamma(\xi)}{\partial(\xi)}d(\xi) \tag{2.38}$$

when the input is the strain. Applying the Laplace transforms to Eqs. 2.37 and 2.38 the following relations can be written considering the variable s:

$$\bar{\gamma}(s) = s\bar{J}(s)\bar{\tau}(s) \tag{2.39}$$

$$\bar{\tau}(s) = s\bar{G}(s)\bar{\gamma}(s). \tag{2.40}$$

By solving Eqs. 2.39 and 2.40 for the transient moduli, the following relation can be obtained

$$\frac{\bar{\tau}(s)}{\bar{\gamma}(s)} = s\bar{G}(s) = \frac{1}{s\bar{J}(s)}, \tag{2.41}$$

and consequently

$$\bar{G}(s)\bar{J}(s) = \frac{1}{s^2}. \tag{2.42}$$

Applying the inverse Laplace transform to Eq. 2.42 yields to the relation in the time-domain

$$\int_0^t G(t-\xi)J(\xi)\,d\xi = \int_0^t J(t-\xi)G(\xi)\,d\xi = t. \tag{2.43}$$

The theoretical interrelation between the time domain and the frequency domain, can involve fairly complex mathematical calculation and the resulting relations are just here reported. The generic symbol R is here used for the equations, to address the response since these interconversions are carried out within the group of responses (relaxation or retardation). The harmonic response function is related to the corresponding time-dependent response function by the following relations:

$$R^*(\omega) = i\,\omega \int_0^\infty R(t)exp(-i\omega t)\,dt \tag{2.44}$$

and

$$R'(\omega) = \omega \int_0^\infty R(t)sin(\omega t)dt \qquad R"(\omega) = \omega \int_0^\infty R(t)cos(\omega t)dt. \tag{2.45}$$

The inverse transforms are:

$$R(t) = \frac{1}{2\pi} \int_0^\infty \frac{R^*(\omega)}{i\omega} exp(i\omega t)d\omega \tag{2.46}$$

and

$$R(t) = \frac{2}{\pi} \int_0^\infty \frac{R'(\omega)}{\omega} sin(\omega t)d\omega \qquad R(t) = \frac{2}{\pi} \int_0^\infty \frac{R"(\omega)}{\omega} cos(\omega t)d\omega. \tag{2.47}$$

The theoretical relations of Eqs. 2.43, 2.44 and 2.46, are not commonly used due to their mathematical complexity. Rather, multiple of easy and approximate methods have been developed for the purpose. A review of these methods, applied to asphalt binders can be found here [67].

2.5 Linear elastic-viscoelastic correspondence principle

The elastic-viscoelastic correspondence (E-VC) principle allows the solution to a viscoelastic problem to be inferred from a reference elastic solution. The E-VC principle is traditionally expressed by means of the Laplace transform of the viscoelastic convolution integral of Eq. 2.16, which is expressed for shear as

$$\tau(t) = \int_0^t G(t-\xi)\frac{\partial \gamma}{\partial \xi} d\xi. \tag{2.48}$$

The Laplace transform $\mathscr{L}$ is an integral transform, particularly used in solving linear ordinary differential equations and is defined as

$$\mathscr{L}\{f(t)\} = \bar{f}(s) = \int_0^\infty f(t)\, e^{-st} dt. \tag{2.49}$$

Given that the Laplace transform of the convolution integral is

$$\int_0^t f(t-\xi) g(\xi) d\xi = \bar{f}(s)\, \bar{g}(s), \tag{2.50}$$

the Eq. 2.48 is written as

$$\bar{\tau}(s) = \bar{G}(s)\, \bar{\gamma}(s) = \bar{G}(s)\, s\, \bar{\gamma}(s) = \tilde{G}(s)\, \bar{\gamma}(s) \tag{2.51}$$

where $\tilde{G}(s) = \bar{G}(s)\, s$ is the *Carson transform* of G.
The time-independent shear response is expressed, based on Eq. 2.3, as

$$\tau = G\gamma, \tag{2.52}$$

and performing in the Laplace domain as

$$\bar{\tau}(s) = G\, \bar{\gamma}(s). \tag{2.53}$$

Comparing Eqs. 2.53 and 2.51, it can be observed that the LVE solution can be obtained through a reference elastic problem, in the Laplace domain, by replacing the material's properties with the corresponding Carson transformed.
A more convenient mathematical formulation of the correspondence principle was proposed by Schapery [68] and involves the definition of *pseudo stresses* and *pseudo strains*, labelled as τ^R and γ^R respectively. The analytical definitions for the pseudo quantities are

$$\gamma^R(t) = G_R^{-1} \int_0^t G(t-\xi)\, \frac{\partial \gamma}{\partial \xi} d\xi \tag{2.54}$$

$$\tau^R(t) = G_R \int_0^t J(t-\xi)\, \frac{\partial \tau}{\partial \xi} d\xi. \tag{2.55}$$

where the coefficient G_R is a constant reference modulus.
Considering Eqs. 2.54 and 2.55, the LVE constitutive equations become

$$\tau(t) = G_R \, \gamma(t)^R \tag{2.56}$$

$$\gamma(t) = G_R^{-1} \, \tau(t)^R. \tag{2.57}$$

Similarly to the Laplace transform, the introduction of the pseudo quantities allows to solve a viscoelastic problem based on the solution of a reference elastic problem. In fact, as can be observed by looking at Eqs. 2.56 and 2.57, also using pseudo quantities the constitutive LVE relations become expressed in the form of the Hooke's law, reported in Eq. 2.53.

2.6 Mechanical models representation

The one-dimensional theory of mechanical models, coming from the electric circuit theory, describes physical systems using a combination of idealized elements, differentiated in general as *active* and *passive*. Active elements are sources of energy, whether passive elements can store or dissipate energy. The theory of linear viscoelastic mechanical models uses as active elements the excitations (stress or strain) and as passive elements the *spring* and the *dashpot*. These elementary elements are represented in Fig 2.5. The inertial effects can be shown to be negligible, in the case of linear viscoelasticity, for a large class of excitations. The theoretical discussion reported in this paragraph would need to be extended in the case of not negligible inertia effects, such as short loading times (ex. impact testing) or high frequencies (ex. wave propagation).
The spring represents the linear purely elastic behaviour (i.e. deformation energy completely stored), and can be described analytically through the Hook's law:

$$\tau = G \, \gamma \tag{2.58}$$

where G is the modulus of elasticity.
The dashpot describes the linear purely viscous behaviour (i.e. deformation energy completely dissipated), and described by the Newton's law:

$$\tau(t) = \eta \, \dot{\gamma}(t) \tag{2.59}$$

where η is the coefficient of shear viscosity.

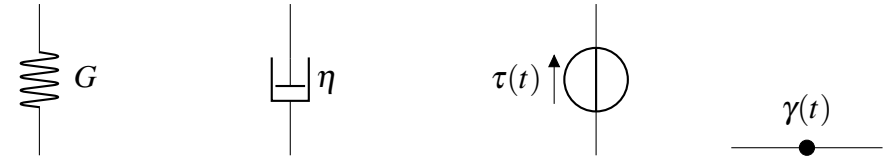

(a) Spring (b) Dashpot (c) Stress (d) Strain

Figure 2.5 Conventionalized symbols for LVE mechanical model theory

Two basic blocks deriving from the two basic combinations of one spring and one dashpot, that are in series and in parallel. These blocks are typically referred to as "units" since are not able to describe the viscoelastic response, which requires more complex models. In general, two elements connected in series show the same stress, whereas two elements combined in parallel experience the same strain and therefore, the corresponding variables (stress or strain) are addictive.
The Maxwell unit, represented in Fig. 2.6a, consists in a spring and a dashpot connected in series. The total strain γ is given by the sum of the strain referred to the spring and that referred to the dashpot as

$$\gamma = \gamma_{spring} + \gamma_{dashpot}. \tag{2.60}$$

The stress-strain differential relation is derived by substituting Eqs. 2.58 and 2.59 into Eq. 2.60:

$$\frac{d\gamma}{dt} = \frac{d\tau}{dt}\frac{1}{G} + \frac{1}{\eta}\tau. \tag{2.61}$$

The Kelvin-Voigt unit, represented in Fig. 2.6b, is defined as a spring and a dashpot connected in parallel. Following the same approach used for the Maxwell unit, the total stress τ is

$$\tau = \tau_{spring} + \tau_{dashpot}. \tag{2.62}$$

The stress-strain differential relation is then derived by substituting Eqs. 2.58 and 2.59 into Eq. 2.62:

$$\frac{d\gamma}{dt} + \frac{G}{\eta}\gamma = \frac{\tau}{\eta}. \tag{2.63}$$

The Maxwell unit describes stress relaxation whereas the Voigt unit is typically referred to strain retardation. Let the excitation be a constant strain γ_0, applied at $t = 0$, the solution of Eq. 2.61 is

$$\tau(t) = G\gamma_0 e^{-Gt/\eta} \tag{2.64}$$

where G and η are material's constants. The characteristic time $\rho = \frac{\eta}{G}$ is termed *relaxation time* and characterises the material's relaxation properties. On the other hand, for a constant stress τ_0 applied at $t = 0$, the solution of Eq. 2.63 is

$$\gamma(t) = \frac{\tau_0}{G}(1 - e^{-Jt/\eta}). \tag{2.65}$$

where J and η are material's constants. Similarly to the relaxation, the characteristic time $\tau_R = \frac{\eta}{J}$ is termed *retardation time*.

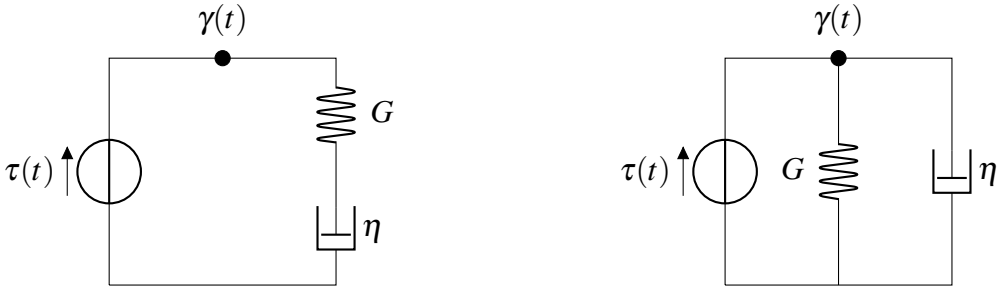

(a) Maxwell unit (b) Voigt unit

Figure 2.6 The Maxwell and Voigt units

As aforementioned, the representation of viscoelastic behaviour demands, in general, more complex models. The most frequently used are the Maxwell and Kelvin-Voigt generalized models. The model representation is slightly different whether the material exhibits long term steady-state flow or not. The term *rheodictic* and *arrheodictic*, adopted by N.W. Tschoegl ([66]-pg 93), are used to address a material which does and does not exhibit long term steady-state flow, respectively. For the purpose of this thesis, the discussion is referred to rheodictic materials. The Maxwell generalized model, represented in Fig. 2.7, consists in several Maxwell units connected in parallel. Considering once again the constant strain γ_0 applied at $t = 0$, the stress, which is addictive, is expressed as

$$\tau(t) = \gamma_0 \sum_{i=1}^{N} g_i e^{-t/\rho_i} \tag{2.66}$$

where $\{g_i, \rho_i; i = 1, ..., N\}$ are the relaxation strength and time respectively.
Similarly, the Kelvin-Voigt generalized model, represented in Fig. 2.8, consists in several Voigt units connected in series.
Let the excitation be a constant stress τ_0 applied at $t = 0$, the strain retardation is expressed as

$$\gamma(t) = \tau_0 \left(J_0 + \frac{t}{\eta_0} + \sum_{i=1}^{N} j_i (1 - e^{-t/\tau_{R,i}}) \right) \tag{2.67}$$

where $\{j_i, \tau_{R,i}; i = 1, ..., N\}$ are the retardation strength and time respectively, J_0 is the glassy compliance, η_0 is the zero shear viscosity.
Eq. 2.66 implies that each relaxation time ρ is associated to a relaxation strength g_i, as well as from Eq. 2.66 can be observed that each retardation time τ_R is linked to a retardation strength j_i. The two relaxation and retardation spectra are so defined, labelled respectively as $H(\rho)$ and $L(\tau_R)$. In general, the two spectra are continuous, although they can be described, with satisfactory approximation, considering a finite number of elements for $\{\rho_i, g_i\}$ and $\{\tau_{R,i}, J_i\}$. Once the set

of parameters $\{\rho_i, g_i\}$ is known $G(t), G'(\omega), G''(\omega)$ can be obtained from the relations

$$G(t) = \sum_{i=1}^{N} g_i e^{-t/\rho_i} \tag{2.68}$$

$$G'(\omega) = \sum_{i=1}^{N} g_i \frac{\omega^2 \rho_i^2}{1+\omega^2 \rho_i^2} \tag{2.69}$$

$$G''(\omega) = \sum_{i=1}^{N} \frac{g_i \rho_i \omega}{1+\omega^2 \rho_i^2}. \tag{2.70}$$

Similarly, once the set $\{\tau_{R,i}, J_i\}$ has been obtained, $J(t), J'(\omega), J''(\omega)$ can be derived as

$$J(t) = J_0 + \sum_{i=1}^{N} j_i (1 - e^{-t/\tau_{R,i}}) + \frac{t}{\eta_0} \tag{2.71}$$

$$J'(\omega) = J_0 + \sum_{i=1}^{N} j_i \frac{1}{1+\omega^2 \tau_{R,i}^2} \tag{2.72}$$

$$J''(\omega) = \sum_{i=1}^{N} j_i \frac{\omega \tau_{R,i}}{1+\omega^2 \tau_{R,i}^2} + \eta_0 \omega. \tag{2.73}$$

The discrete set of exponential decays describing $G(t)$ and $J(t)$ in Eqs. 2.68 and 2.71 are referred to as *Prony series*.

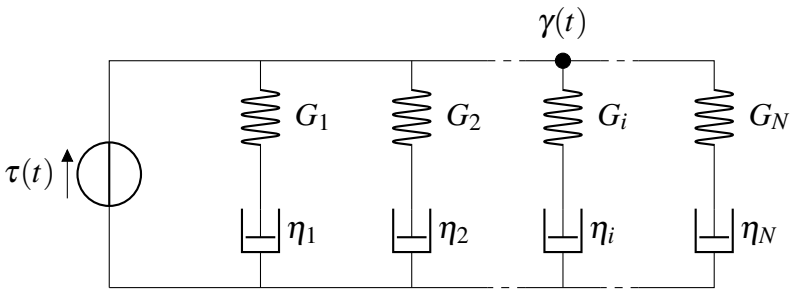

Figure 2.7 The Maxwell generalized model

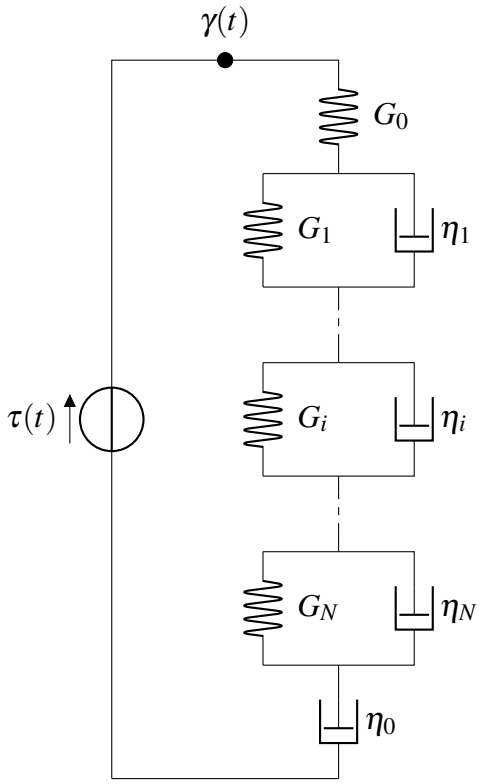

Figure 2.8 The Voigt generalized model

2.6.1 Boltzmann integral numerical solution using Prony series

The determination of the discrete relaxation spectrum through Prony coefficients allows to solve numerically the convolution integral of Eq. 2.16 using the *state variables* method. The key idea is to transform the convolution integral into a two-step recurrence formula, involving internal variables, such that each step is described by the previous one [69]. The method is valid under the hypothesis of linearity. Defining a time interval of interest $[t_0,t]$, with $t > 0$ and $t > t_0$, the discretization is

$$[t_0,t] = \bigcup [t^n,t^{n+1}] \tag{2.74}$$

where $n \in \mathbb{I}$ and $t^{n+1} = t^n + \Delta t^n$.
Let the excitation be a strain, applied at $t_0 = 0$, the convolution integral of Eq. 2.16 can be written as

$$\tau(t) = \int_0^t \sum_{i=1}^{N} g_i e^{-\frac{t-\xi}{\rho_i}} \dot{\gamma} d\xi, \tag{2.75}$$

by expressing the relaxation modulus using the Prony coefficients as shown in Eq. 2.68. Considering the time step $t = t^n$ the integral of Eq. 2.75 becomes

$$\tau^n(t) = \int_0^{t^n} \sum_{i=1}^{N} g_i e^{-\frac{t^n-\xi}{\rho_i}} \dot{\gamma} d\xi. \tag{2.76}$$

or

$$\tau^n(t) = \sum_{i=1}^{N} \psi^n \tag{2.77}$$

by introducing the state variable ψ^n for time t^n. The i-th state variable at time t^n is defined as

$$\psi_i^n = g_i \int_0^{t^n} e^{-\frac{t^n-\xi}{\rho_i}} \dot{\gamma} d\xi \tag{2.78}$$

and considering the time step $t = t^{n+1}$, as

$$\psi_i^{n+1} = g_i \int_0^{t^{n+1}} e^{-\frac{t^{n+1}-\xi}{\rho_i}} \dot{\gamma} d\xi. \tag{2.79}$$

For time intervals $\Delta t = t^{n+1} - t^n$, sufficiently small that the strain rate $\dot{\gamma}$ can be expressed as $\frac{\Delta\gamma}{\Delta t}$, the integral formulation of Eq. 2.79 is simplified as

$$\begin{aligned} \psi_i^{n+1} &= \psi_i^n e^{-\frac{\Delta t}{\rho_i}} + g_i \left(\frac{\gamma^{n+1} - \gamma^n}{\Delta t} \right) \int_{t^n}^{t^{n+1}} e^{-\frac{t^{n+1}-\xi}{\rho_i}} d\xi = \\ &= \psi_i^n e^{-\frac{\Delta t}{\rho_i}} + g_i \left(\frac{\gamma^{n+1} - \gamma^n}{\Delta t} \right) \left[1 - e^{-\frac{\Delta t}{\rho_i}} \right] \rho_i. \end{aligned} \tag{2.80}$$

As can be noticed, using the state variables the convolution integral can be easily solved solving Eq. 2.80, by knowing the discrete relaxation spectrum $\{g_i \rho_i\}$. The same formulation can be obtained when considering the stress excitation, instead of the strain excitation.

2.6.2 Model fitting

The two generalized models of Maxwell and Voigt are used to determine the relaxation and retardation spectrum indirectly through the Prony coefficients, as described. The spectra are not accessible by direct experiments and each spectrum is considered as a sum of several line spectrum, as shown in Eqs. 2.68 and 2.71, determined by fitting the correspondent model on the experimental data. The resulting spectrum is so not the "true" spectrum, which remains unknown, and is not unique since it is dependent on the fitting procedure selected. The success of the solution is evaluated by comparing the original experimental data with those reconstructed using the assessed spectrum. The easiest techniques, and perhaps the most used, are the Collocation method of R. Schapery [70] and the Multidata method of T.L. Cost and E.B. Becker [71]. However, the two methods can generate negative strength coefficients, theoretically inconsistent, which led to a wavy reconstructed curve. To overcome these limitations, several methods have been proposed such that of M. Baumgaertel and H.H. Winter [72, 73] or that proposed for polymeric liquids by C. Elster, J. Honerkamp and J. Weese [74, 75, 76] or the recursive algorithm of N.W. Tschoegl and I. Emri [77, 78, 79, 80].
In this paragraph, the Collocation method of R. Schapery [70] and the Parsimonious Model (PM) of M. Baumgaertel and H.H. Winter [72, 73] are described, for the purpose of this thesis work. The discussion is referred to the relaxation set of constants $\{\rho_i, g_i; (i = 1, ..., N)\}$, but in a similar

way can be formulated considering the retardation coefficients $\{\tau_{R,i}, j_i; (i = 1, ..., N)\}$.

Collocation method

Suppose a discrete set of moduli G_j measured at times t_j, such as $\{G_j, t_j; j = 1, ..., K\}$, and the corresponding $G(t_j)$ assessed through Eq. 2.68, the following relation may be written:

$$G_j = \sum_{i=1}^{N} g_i e^{-t_j/\rho_i} = G(t_j). \tag{2.81}$$

The determination of the appropriate set of Prony coefficients $\{\rho_i, g_i; (i = 1, ..., N)\}$ is performed by *collocating* the observed G_j with the theoretical $G(t_j)$. The set of K non-linear equations is difficult to solve and the method proposed by Schapery suggests to relate the relaxation times to the experimental time such that

$$\rho_i = a t_j, \tag{2.82}$$

where a indicates the proportionality constant. The coefficients ρ_i are fixed and the unknowns remain the N coefficients g_i. Since the number of coefficients N is equal to the number of measured points K, the system is expressed as

$$G_j = B_{ji}\, g_i. \tag{2.83}$$

The matrix inversion gives the unknowns g_i

$$g_i = \left[B_{ji}\right]^{-1} G_j. \tag{2.84}$$

The method is easily extended to the harmonic response by collocating the measured storage modulus G'_j with the assessed one $G'(\omega_j)$ by means of Eq. 2.69. The relaxation times are, in such case, related to the measured frequency ω_j as

$$\rho_i = \frac{1}{a\,\omega_j}. \tag{2.85}$$

Experimental observations on LVE materials are generally performed considering equally logarithmic spaced time intervals, such that

$$t_j = 10^{m+pj} \tag{2.86}$$

or, similarly

$$\omega_j = 10^{m+pj}. \tag{2.87}$$

where m is the beginning of the time scale and p the spacing. The time scale has to be properly spaced to obtain a successful solution and usually p is chosen to be unity. It is important to remember that the collocation is not unique and different set of coefficients can be obtained depending on the values of m and p selected. However, the matrix inversion of Eq. 2.84 is mathematically an ill-posed problem and it may results in a series of negative coefficients g_i, which are theoretically inconsistent. The Collocation method has been widely used for asphalt binders, in particular for the calculation of the pseudo quantities of Eqs. 2.54 and 2.55, needed

for the application of the E-VC principle in the Viscoelastic Continuum Damage (VECD) model [81, 82]. Concerning asphalt mixtures, the AASHTO specification TP 107-14 [83], suggests to select the ρ_m coefficients spaced one decade apart, ranging from $2x10^x$ to $2x10^y$ where x and y are the same power values of the measured angular frequencies, leading typically to obtain 16 Prony coefficients. Regarding asphalt binders, two ρ coefficients are suggested for each decade, implying even more Prony coefficients (typically 32).

Parsimonious model PM

M. Baumgaertel and H.H. Winter [72, 73] proposed a methodology for model fitting, which allows to avoid negative strength coefficients g_i, considering the fewest number of line spectra. The representation is defined the *Parsimonious Model* (PM), since the procedure is based on the idea that "the discrete relaxation times should be freely adjustable so that they can converge to values which are characteristic for the material". In other words, supposing that there exists a discrete set of Maxwell-modes which represents the continuous relaxation spectrum with sufficient accuracy, there will be a number of elements for which the fitting is optimum and this *optimum discrete spectrum* is the PM-spectrum of the material. Considering Eqs. 2.69 and 2.70, the coefficients $\{\rho_i, g_i; (i = 1, ..., N)\}$ are then determined such that

$$SD = \sum_{j=1}^{m} \left(\left[\frac{G'(\omega_j)}{G'_j} - 1 \right]^2 + \left[\frac{G''(\omega_j)}{G''_j} - 1 \right]^2 \right) = min \tag{2.88}$$

where G'_j and G''_j are the measured moduli and $G'(\omega_j)$ and $G''(\omega_j)$ are the calculated ones.The number of relaxation modes N is freely adjustable as the spacing of the relaxation times. Starting from the minimum two modes $N = 2$, the SD value of Eq. 2.88 starts to decrease sharply increasing N, until a certain point after which it remains nearly constant. This minimum value reflects the experimental noise of the data and cannot be reduced, even further increasing N. This number N, corresponding to minimum SD value, is considered as the optimum number of modes.

2.7 Temperature dependence

The mechanical properties of a viscoelastic material are strongly affected by temperature and/or pressure. This dependence can be mathematically described, for a class of materials, such that it is possible to refer the chosen response function to a reference temperature T_{ref} and/or pressure P_{ref}, through temperature and/or pressure shift functions [84]. Such materials are referred to as thermo-rheologically and/or piezo-rheologically simple materials, respectively for temperature and pressure dependence [85]. The following discussion is referred to the thermo-rheological simplicity, considering the pressure as constant.

The thermo-rheological simplicity requires that all the material response times (relaxation or retardation times) depend equally on temperature, such that this dependence can be described by a temperature shift function [86]. The material LVE functions, obtained at different temperatures as a function of time, can be superimposed to build a master curve for a reference temperature,

using proper shift factors. The *thermo-rheologically simple postulate* [87, 88], also referred to as *time-temperature superposition principle* or *method of the reduced variables*, states that, when the material is thermo-rheologically simple, the response function $R(T,t)$, can be referred to a reference temperature T_0 by shifting the curve on the logarithmic time scale, thereby extending the experimental time scale. The mathematical description of the principle is

$$R(T,t) = R(T_0, t_{red}), \tag{2.89}$$

where T is the measured temperature, t is the experimental time, T_0 is the reference temperature and t_{red} the reduced time, expressed as

$$log(t_{red}) = log(t) - \alpha(T), \tag{2.90}$$

where α(T) is the shift function.
The following relations can be expressed for the shift function

$$\alpha(T_0) = 0 \qquad\qquad \frac{d\alpha(T)}{dT} > 0, \tag{2.91}$$

expressed as

$$a_T(T_0) = 1 \qquad\qquad \frac{da_T(T)}{dT} > 0 \tag{2.92}$$

when considering the following variable change

$$\alpha(T) = log(a_T(T)). \tag{2.93}$$

Recalling Eq. 2.90, the reduced time t_{red} is defined as

$$t_{red} = \frac{t}{a_T(T)}. \tag{2.94}$$

The nature of the shift factors, needed to superpose the curves, are a matter of empirical investigation and the justification for using superposition rests on empirical observations [87]. Several functions have been proposed and adopted for the analytical description of the shift factors, such as the widely used William-Landel-Ferry (WLF) function [89]. A wide review on these functions, applied on asphalt binders measurements, can be found here [90]. However, these continuous functions can be implemented only considering a limited range of temperature which does not include thermal discontinuities, such as the glass transition. For this reason, a second order polynomial function, fitted on the shift coefficients, is also in some cases adopted to represent the shift function.
One of the method available to assess the shift coefficients is that based on the Kramers-Kronig relation, proposed by Chailleux E, et al. [91]. The approximated Kramers-Kronig relation allows

to relate the modulus $|G^*|(\omega)$ to the phase angle $\delta(\omega)$ such that

$$\delta(\omega) \approx \frac{\pi}{2} \frac{dlog(|G^*|(\omega))}{dlog(\omega)}. \tag{2.95}$$

Considering two close frequencies ω_i and ω_j and the same temperature T, the average of the two angles measured for each frequency $\delta_{avr}^{(\omega_i),\omega_j}$ is

$$\delta_{avr}^{(\omega_i),\omega_j} \frac{2}{\pi} = \frac{log(|G^*(T,\omega_j)|) - log(|G^*(T,\omega_i)|)}{log(\omega_j) - log(\omega_i)}. \tag{2.96}$$

Similarly for two temperatures T_i and T_j, by fixing the angular frequency

$$\delta_{avr}^{(T_i),(T_j)} \frac{2}{\pi} = \frac{log(|G^*(T_j,\omega)|) - log(|G^*(T_i,\omega)|)}{log(a_{T_j}) - log(a_{T_i})}. \tag{2.97}$$

Therefore

$$log(a_{T_i,T_ref}) = \sum_{j=i}^{ref} log(a_{T_j,T_{j+1}}) \tag{2.98}$$

and

$$log(a_{T_i,T_ref}) = \sum_{j=i}^{ref} \frac{log(|G^*(T_j,\omega)|) - log(|G^*(T_{j+1},\omega)|)}{\delta_{avr}^{T_j,T_{j+1}}(\omega)}. \tag{2.99}$$

Part II

Development of the methodology

Preamble

This part II discusses the development of the Monotonic Torsional Loading (MTL) test, both considering the experimental procedure and the corresponding modelling approach. The test protocol described is the results of several attempts, which are not reported for the sake of simplicity. The experimental investigation involved four unaged binders, preliminarily characterized for the linear viscoelastic response and the glass transition temperature. The MTL test procedure was adopted to determined failure response of each binder, by means of several test temperatures and strain rates. The results were modelled considering the time-temperature superposition principle and for each material a critical temperature was determined. Physical hardening effects were not considered in the analysis since the test conditioning part was properly designed to ensure thermal equilibrium avoiding the arise of hardening phenomena. The MTL test results are then evaluated in terms of test repeatability and chemical ageing of materials.

Chapter 3

Experimental

3.1 Materials

The experimental study involved four unaged asphalt binders, listed in Table 3.1. Three of them, coded as B1, B2 and B3, were unmodified having a different penetration grade (PEN) and the fourth one, labelled as B4, was an SBS-modified binder.

Table 3.1 Materials

Binder Code	Nature of the binder	PEN
B1	Unmodified	40/60
B2	Unmodified	50/70
B3	Unmodified	70/100
B4	SBS-modified	30/45

The materials were firstly subjected to a preliminary laboratory investigation by performing frequency sweep tests at different temperatures by means of the DSR (Fig. 1.4a), following the AASHTO T315 [92]. The test temperatures were ranged from 34 °C to −30 °C, and the angular frequencies between 1 rad s^{-1} and 100 rad s^{-1}. For the purpose, the DSR was equipped with parallel plates measurement system of 8 mm for intermediate temperatures and of 4 mm (Fig. 1.4b) for low temperatures. The low temperature measurements were corrected for the machine compliance error, as explained in the following section 3.4.
Experimental results were plotted in the form of Black diagram, shown in Fig. 3.1. The Black space is commonly used for the preliminary evaluation of raw data coming from frequency sweep tests. In general, the material is considered as thermo-rheologically simple when its Black curve is continuous, thus validating the applicability of the TTSP [93]. The curves corresponding to binders B2, B3 and B4 resulted to be continuous and smooth on the complete range of frequencies and therefore, the TTSP was considered valid over the complete range of investigated frequencies. For binder B2, the imperfect superposition of the raw data, observed at phase angle values of about 30°, was attributed to the change in the measurement system and not to a complex

response of the material. Conversely, in the case of binder B1 the Black diagram becomes a little bit scattered at phase angle values above 50° and the TTSP was considered valid at low temperatures only.

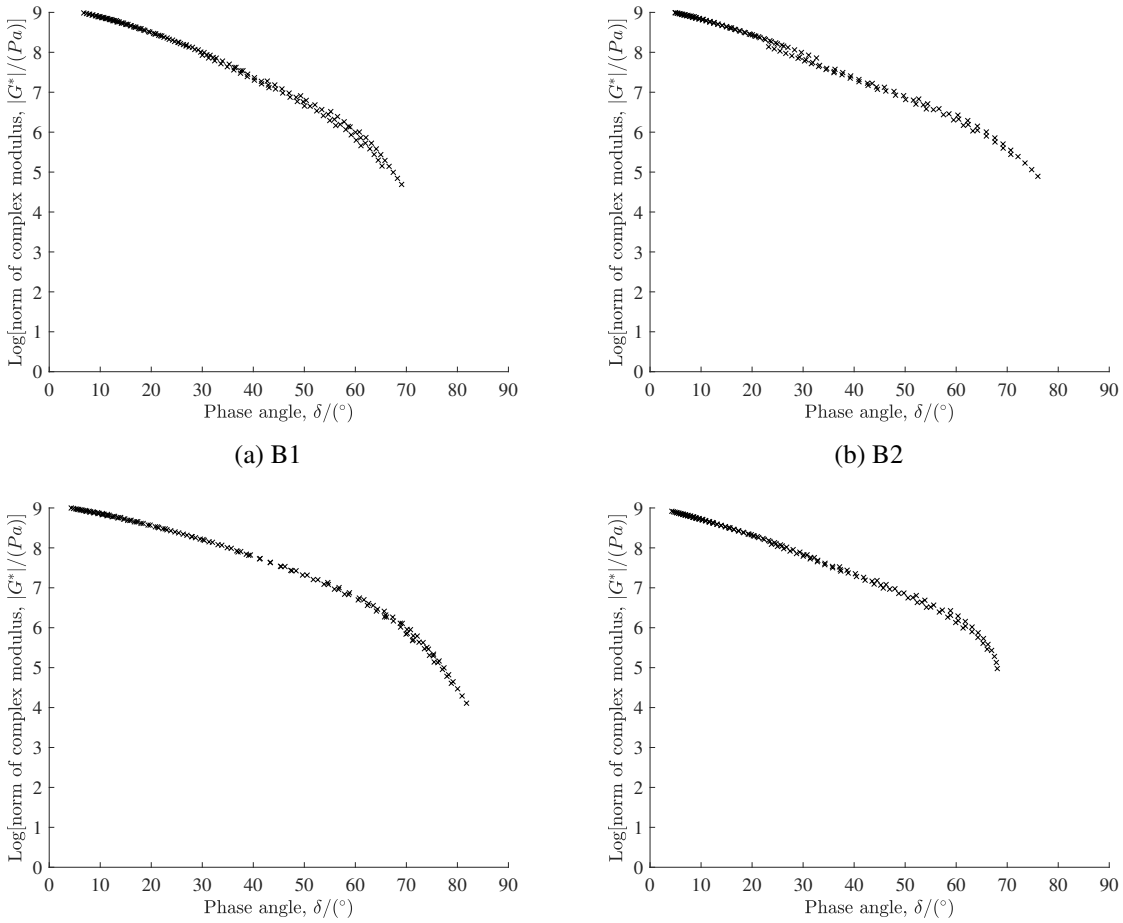

(a) B1

(b) B2

(c) B3

(d) B4

Figure 3.1 Black diagram

The applicability of the TTSP allows to model the experimental data into master curves, selecting a reference temperature T_{ref}, as explained in section 2.7. In order to remain within the range of temperature of interest, the T_{ref} was fixed equal to -15 °C. The horizontal shift factors were determined by means of the Kramers-Kronig relationship of Eq. 2.99, since the experimental range of temperature, including the glass transition, did not allow to use a continuous function of temperature. Outcomes are reported in Table 3.2. As can be observed, the shift factor is equal to 0 for the selected T_{ref} and increases monotonically as the temperature departs from the T_{ref}. Binder B2 shows slightly higher shift factors, with respect to the other materials, indicating a higher sensitivity to the change in temperature.

Table 3.2 Shift factors

Temperature ($°C$)	B1	B2	B3	B4
-30	2.03	2.17	2.05	2.19
-25	1.41	1.54	1.47	1.54
-20	0.81	0.88	0.83	0.88
-15	0	0	0	0
-10	-0.95	-1.03	-0.98	-1.02
-5	-1.83	-1.98	-1.88	-1.98
0	-2.66	-2.88	-2.72	-2.88
4	-3.63	-3.97	-3.73	-3.79
10	-4.50	-4.88	-4.54	-4.69
16	-5.31	-5.75	-5.28	-5.54
22	-6.06	-6.57	-5.95	-6.32
28	-6.77	-7.34	-6.57	-7.05
34	-7.37	-8.00	-7.13	-7.69

The experimental data were shifted horizontally, using the assessed shift factors (Table 3.2) and the resulting master curves of the norm of the complex modulus $|G^*|$ and the phase angle δ are shown in Fig. 3.2. The master curves allow to evaluate the material LVE response [94]. As can be observed, all the modulus curves approached the maximum value of about 1 GPa for high values of angular frequency. For all the materials considered, the phase angle fell between 3° and 4° in correspondence of the maximum value of the modulus. Observing the phase angle curves, binder B1 appears to reach the lowest value at low frequencies among the unmodified binders, comparable with that obtained for the SBS modified binder. For the range of frequency investigated, binder B3 showed the widest range of variation for the modulus corresponding to the highest slope of the viscous asymptote. Considering the cross over frequency ω_0, i.e. the frequency for which the phase angle is equal to 45°, binders B2 and B4 showed the lowest values, followed by the intermediate value of binder B1 and the highest value of binder B3. The cross over frequency can be seen as an indicator of the material consistency, at the selected temperature, and resulted to be consistent with the penetration grades of Table 3.1.

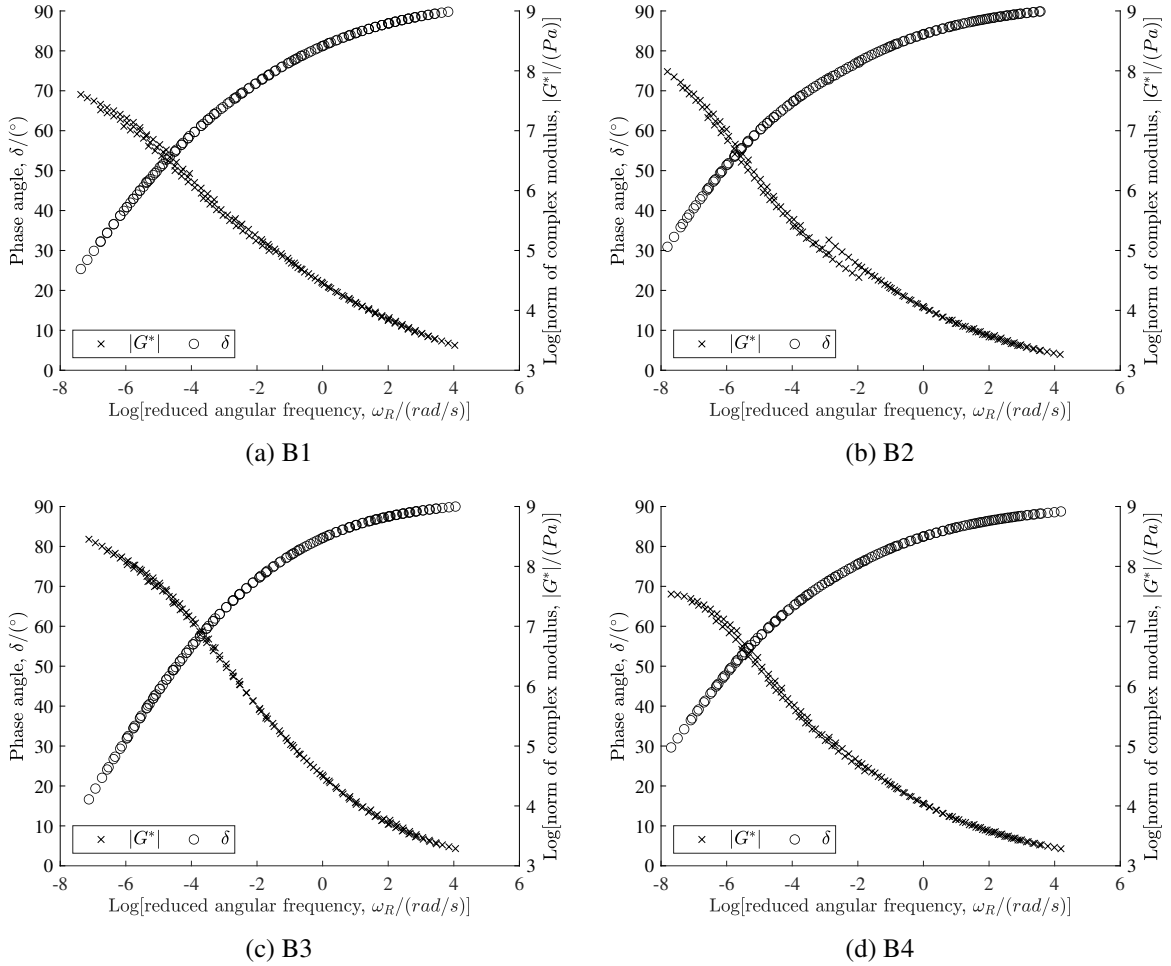

(a) B1

(b) B2

(c) B3

(d) B4

Figure 3.2 Master curves of the experimental storage modulus G' and loss modulus G", for a reference temperature T_{ref} of $-15\,°C$

3.2 Glass transition temperature

The glass transition temperature (T_g) was evaluated, for all the selected materials, through the DMA and the DSC technique, explained in section 1.3, assessing the corresponding $T_{g,DMA}$ and $T_{g,DSC}$ were assessed.

The $T_{g,DMA}$ was inferred from the frequency sweep test results of section 3.1, as the temperature corresponding to the peak value of the loss modulus G", by fixing the frequency to 1 Hz, as shown in Fig. 3.3.

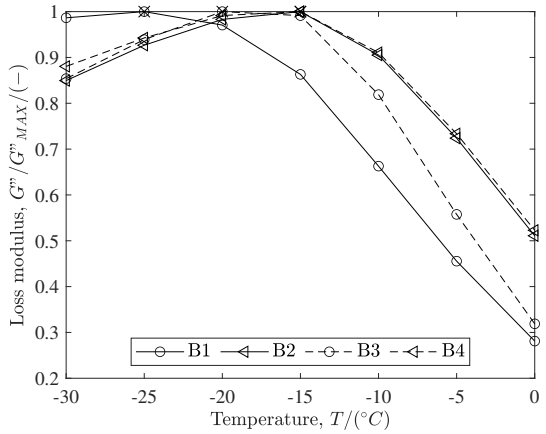

Figure 3.3 DMA glass transition temperature $T_{g,DMA}$

The calorimetric $T_{g,MDSC}$ was determined by means of a Modulated Differential Scanning Calorimeter MDSC Q100 TA instrument, following a procedure similar to that adopted by Chailleux et al. [95]. Therefore, a sample of about 10 mg of asphalt binder was heated up to 180 °C at 10 °C min^{-1} rate, to remove the thermal history. Then, the material was cooled down to 40 °C, with the same temperature rate. The temperature rate was lowered to 1 °C min^{-1} from 40 °C to −40 °C, and lastly the material reached −80 °C at 5 °C min^{-1}. The temperature rate was selected in order to balance the experimental time and the time the material needs to accomplish its internal rearrangements. At the end of the cooling phase, a modulated ramp of 5 °C min^{-1} was applied, with an oscillation period of 60 s and an amplitude of ± 0.80 °C. The $T_{g,MDSC}$ was determined as the inflection point of the stepwise drop in the heat capacity of the material, considering the MDSC reversible heat flow curve, as illustrated in Fig. 1.8a. The crystalline fraction can additionally be determined through calorimetry as the area of the endotherm peak, which for the modulated calorimetry is evaluated using the non-reversible heat flow curve. Since the wax enthalpy typically ranges between 228 J g^{-1} and 169 J g^{-1}, the average value of 200 J g^{-1} was used to determine the wax content.
The results in terms of $T_{g,DMA}$, $T_{g,MDSC}$ and wax content are reported in Table 3.3 for all the materials investigated.
Observing the values of $T_{g,DMA}$ and $T_{g,MDSC}$, a good correlation was found, as also shown in Fig 3.4, with a correlation coefficient of about 0.8. However, it has to be remembered from section 1.3, that the T_g value is strongly dependent on the experimental conditions adopted and therefore the two values were not supposed to be correlated.
Table 3.3 reports also the wax content inferred from the MDSC curve, showing that binder B1 has the highest percentage of wax of 1.32 % whereas binder B4 the lowest percentage of 0.37 %.

Table 3.3 Glass transition temperature assessed by means of DMA and MDSC techniques and wax content

Material	$T_{g,DMA}$ (°C)	$T_{g,MDSC}$ (°C)	Wax content (%)
B1	-25	-22.7	1.32
B2	-15	-17.7	0.78
B3	-20	-17.6	0.61
B4	-15	-16	0.37

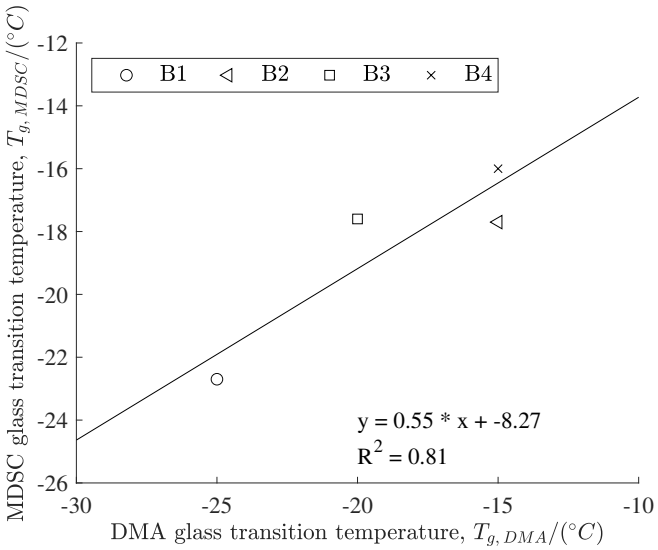

Figure 3.4 Comparison between $T_{g,DMA}$ and $T_{g,MDSC}$

3.3 MTL test: specimen preparation and test procedure

The Monotonic Torsional Loading (MTL) test was developed to characterize the low temperature failure properties of asphalt binders by means of the DSR (Fig. 1.4a), equipped for with 4 mm parallel plates geometry (Fig. 1.4b). The main idea was to develop a simple procedure to address binders failure properties at low temperatures, through short testing and by using the DSR, a versatile and easy-to use device, already adopted for the high temperature characterization of binders. To reduce the torsional stiffness, the specimen height was increased, with respect to the standard, and after several attempts the value of 5 mm was selected. The choice was based on experimental needs, since higher specimens were too complex to prepare. However, the 5 mm cylindrical specimen, led the DSR conditioning hood to be not completely lowered. A polystyrene disk was used to overcome this problem assuring the specimen to be conditioned properly, as shown in Fig. 3.5.

Figure 3.5 DSR conditioning hood for MTL test

The specimen was prepared directly on the upper plate, using an aluminium mould. The final procedure for specimen preparation, proposed here, comes from several trials, focused on finding an easy and repeatable way to prepare the specimen. The following procedure can be adopted:

1. the gap between DSR plates is zeroed, and the upper plate is released;
2. a mould, made by rolling an aluminium sheet, is fitted on the upper plate (Fig. 3.6a);
3. a small amount (around 0.1 g) of material is inserted into the mould;
4. the mould, containing the material, is heated, until good adhesion between the material and the plate is achieved;
5. the mould, filled with the binder, is placed in a refrigerator for the time necessary to remove the aluminium sheet without damaging the specimen (Fig. 3.6b);
6. the de-moulded specimen is cut by means of a hot spatula, to obtain the target height of 5 mm;
7. the upper plate is placed back into the DSR and lowered, until the cylindrical specimen comes in contact with the preheated lower plate.

(a) Aluminium mould

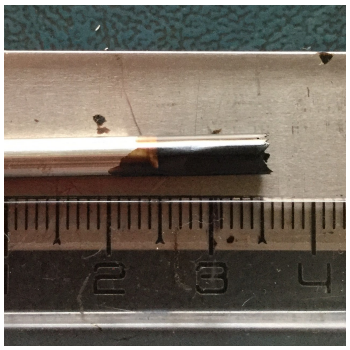

(b) Demoulded specimen

Figure 3.6 Specimen preparation

The test protocol developed consists of three subsequent phase, each of which was extensively evaluated:

1. The conditioning phase represents the most sensitive part of the test, due to the high susceptibility of the binders to the variation of temperature. Hence, adequate control of conditioning is extremely important for the accuracy and repeatability of the results. The conditioning phase was divided into three steps, summarized in Table 3.4. The first two steps allow the sample to reach the test temperature, with a proper rate. The rate was evaluated balancing the experimental testing time and the time the material needs for molecular rearrangements. During the third step, the specimen is conditioned at the test temperature. The isothermal conditioning time was fixed as 10 min since, after several attempts (see [96]), it was observed that, due to the little amount of material, a short interval of time can be used for isothermal conditioning, thereby reducing the testing time. During the overall cooling phase, the gap between the two plates is automatically reduced to maintain the normal force close to zero.

2. The fingerprint test consists in an isothermal frequency sweep performed at the test temperature. The angular frequencies were selected to range between $1\,\mathrm{rad\,s^{-1}}$ and $100\,\mathrm{rad\,s^{-1}}$, and the strain level to remain in the LVE domain. The fingerprint allows to characterize each sample in terms of LVE properties, in order to consider the specimen-to-specimen variability.

3. The torsional loading test leads the specimen to fail for a monotonic torsional load, which increases with a fixed strain rate.

Table 3.4 Conditioning phase of MTL test

Step	Initial temperature (°C)	Final temperature (°C)	Temperature rate $\left(^{\circ}\mathrm{C\,min^{-1}}\right)$
1	20	4	2
2	4	Test temperature	1
3	Isothermal conditioning at test temperature for 10 min		

3.4 Determination of the machine compliance

The DSR measurements at low temperatures need to be corrected for the machine compliance error, which becomes significantly since the sample deformation is comparable with the deformation of the measurement tool. In fact, the deflection angle recorded by the DSR φ_m, is given by the sum of the sample deflection angle φ_s and the measuring tool deflection angle φ_t as:

$$\varphi_m = \varphi_s + \varphi_t = \frac{M}{K_s} + \frac{M}{K_t}, \tag{3.1}$$

where M is the applied torque and K_s and K_t are respectively the torsional stiffness of the sample and the measuring tool. For high temperature measurements, K_s is significantly lower than K_t and therefore the term φ_t of Eq. 3.1 can be neglected. Conversely, at low temperatures the material K_s becomes comparable with the K_t of the measurement system and the term φ_t of

Eq. 3.1 is no longer negligible. A correction method for oscillatory measurements was reported by K. Schröter et al. [36], such that the norm of the complex modulus of the sample $|G^*|_s$ is

$$|G^*|_s(\omega) = \frac{|G^*|_m(\omega)}{1 - \frac{J_t}{k_g}|G^*|_m(\omega)} \tag{3.2}$$

where $|G^*|_m$ is the norm of the complex modulus measured, $J_t = 1/K_t$ is the compliance of the measurement tool and k_g is a geometry conversion factor. The factor k_g, for parallel plates geometry is

$$k_g = \frac{2h}{\pi R^4} \tag{3.3}$$

where h is the specimen height and R the radius.
Therefore, the machine compliance J_t has to be measured to correct the measurements, following Eq. 3.2. The procedure adopted to measure the value of J_t involved "gluing" together the upper and lower plates, using the 4 mm geometry. This allows the sample deformation to tend to zero and thereby to measure the deformation of the measurement system. Two different tests were then performed: (1) a torque sweep test, with the angular frequency fixed to $1\,\mathrm{rad\,s^{-1}}$ and (2) a monotonic torque test, with a torque rate of $20\,\mathrm{mN\,m\,min^{-1}}$. The measured deflection angle φ was plotted against the applied torque M for both tests and the compliance J_t was determined as the slope of the resulting straight lines, as shown in Fig. 3.7.

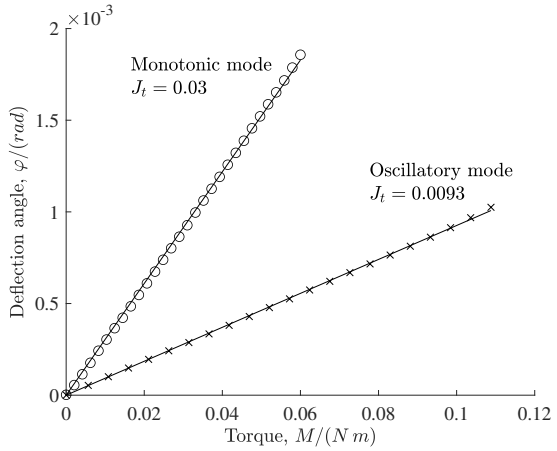

Figure 3.7 Determination of the machine compliance

As can be observed in Fig. 3.7, the two tests led to different results in terms of J_t. In particular, the value obtained using the monotonic mode was higher than that of the oscillatory mode. This was caused by the automatic real-time correction performed by the DSR software, which occurs for the oscillatory mode only. The assessed value of J_t was used to adjust the device settings to let the DSR software to automatically correct the oscillatory measurements. The monotonic measurements were instead corrected manually, post-processing the DSR raw data, as

$$\varphi_s = \varphi_m - J_t M. \tag{3.4}$$

3.5 Experimental plan

The experimental investigation was planned to characterize the brittle response of each binder, in its unaged state, by means of the proposed MTL test protocol. Several MTL tests were carried out, considering different combinations of temperature and strain rate, selected based on some preliminary investigations. The experimental plan is reported in Table 3.5. At least three replicates were performed for each test condition.

Table 3.5 Experimental plan

Binder	Temperature (°C)	Strain rate $\left(s^{-1}\right)$
B1	-15	0.0005, 0.001, 0.002
	-17.5	0.001
	-19	0.002
	-20	0.0005, 0.001
	-25	0.0005, 0.001
B2	-9.5	0.002
	-10	0.0005, 0.001
	-11	0.001
	-13	0.001
	-15	0.0005, 0.001, 0.002
	-17.5	0.001
	-20	0.0005, 0.001
B3	-12.5	0.002
	-15	0.0005, 0.001, 0.002
	-20	0.0005, 0.001
	-25	0.0005, 0.001
B4	-15	0.001, 0.002
	-20	0.0005, 0.001
	-25	0.0005, 0.001

3.6 Test results

Fig. 3.8 shows some examples of stress-strain curves deriving from the MTL test. All tests were corrected manually for the machine compliance error, as explained in section 3.4. As can be observed, the failure point can be easily detected from the curves, allowing to determine for each test the failure shear stress and strain. Observing Fig. 3.8, three different regions of behaviour can be detected in the stress-strain space: (1) the ductile region, (2) the brittle region and (3) the ductile-brittle transition region (or quasi-brittle).

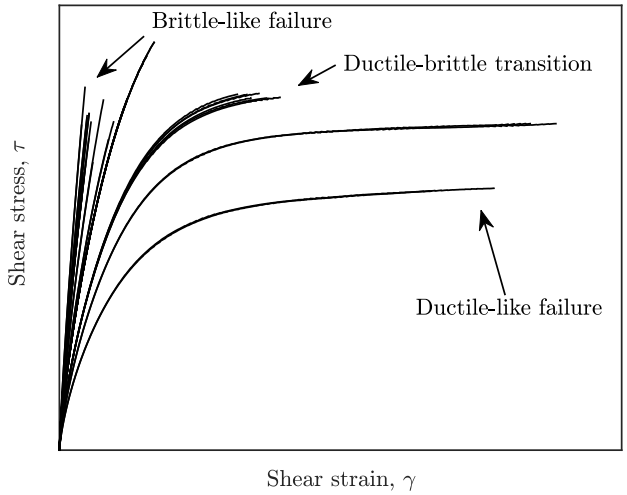

Figure 3.8 MTL shear stress and strain output

In general, asphalt binders show a ductile-like response for higher temperatures and/or lower strain rates, with relatively low failure shear stresses and high failure shear strains. Conversely, for lower temperatures and/or higher strain rates, the material exhibits a brittle-like behaviour, characterized by relatively high failure shear stresses and low failure shear strains. The transition region between the brittle- and the ductile-like response defines the third region. The fracture morphology observed after failure is shown in Fig. 3.9. As can be noticed, the characteristic 45° fracture of the torsional single-load failure for brittle materials (see Fig. 1.5) was obtained.

Figure 3.9 Fracture morphology

For each combination of strain rate and temperature investigated (summarized in Table 3.5) the failure shear stress and strain were assessed. The results are shown in Fig. 3.10 to 3.13. The general trend of the two variables appears to be consistent with expectations, since the response becomes more brittle (high value of stress and low value of strain) as the temperature decreases and/or the strain rate increases.

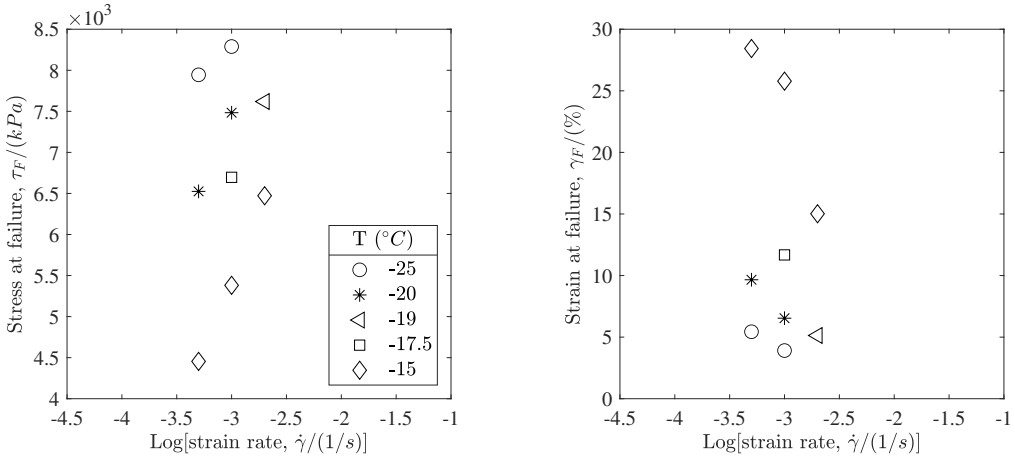

Figure 3.10 Experimental failure shear stress and strain for binder B1

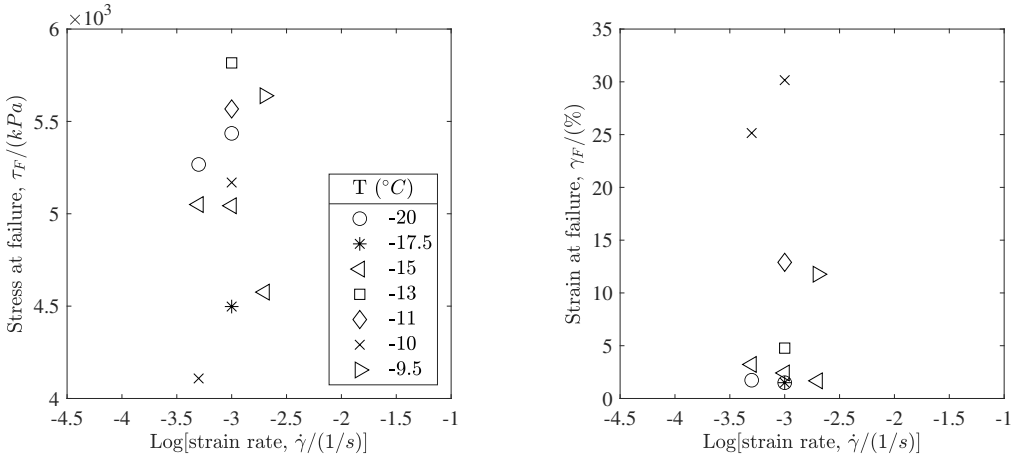

Figure 3.11 Experimental failure shear stress and strain for binder B2

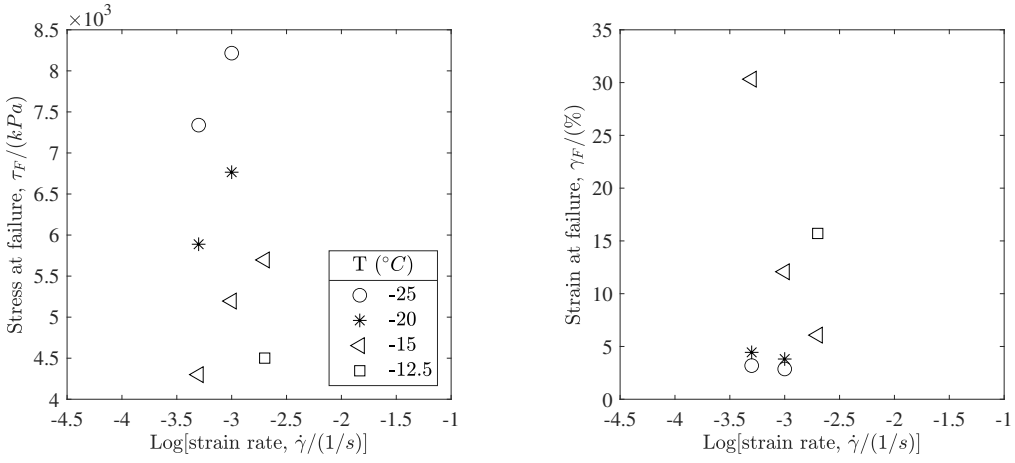

Figure 3.12 Experimental failure shear stress and strain for binder B3

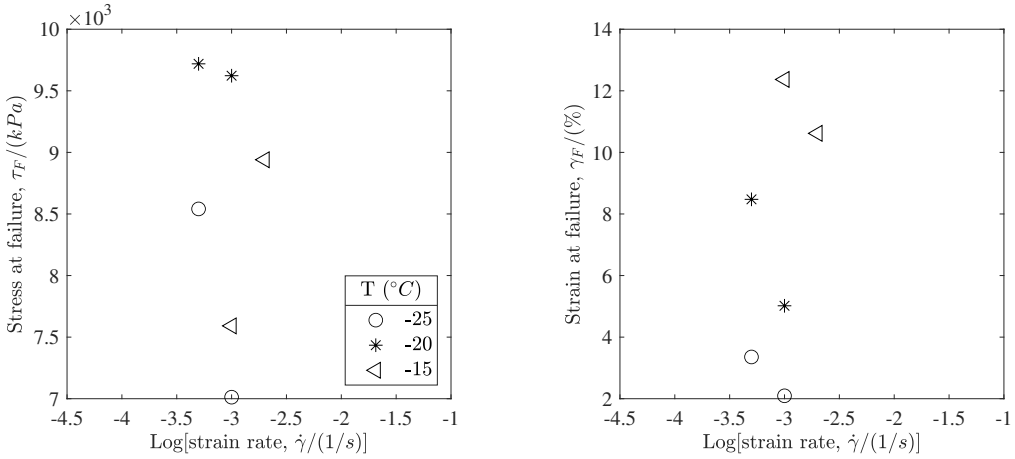

Figure 3.13 Experimental failure shear stress and strain for binder B4

Chapter 4

Modelling approach

4.1 Brittleness index

The brittleness index I_B was proposed as a synthetic parameter to represent the material response. The index is defined by applying the elastic-viscoelastic correspondence (E-VC) principle, explained in section 2.5, through the use of pseudo quantities. Pseudo strains were assessed using Eq. 2.54, by fixing the reference modulus G_R as unity. The convolution integral of Eq. 2.54 was solved by means of the state variable method, described in section 2.6.1. The discrete relaxation spectrum, needed to solve Eq. 2.80, was indirectly determined using the frequency sweep test data performed for the preliminary linear viscoelastic characterization of investigated materials (section 3.1) since, as mentioned in section 2.6.2, the spectrum is not accessible through direct experiments. To avoid the arise of negative relaxation strengths from the model fitting, an algorithm based on the Parsimonious Model (PM), proposed by Baumgaerted and Winter [72, 73], described in section 2.6.2, was used. The relaxation times ρ_i were selected to be equally spaced in the logarithmic time scale, such that the minimum and the maximum relaxation time, labelled as ρ_m and ρ_1 respectively, were equal to

$$\rho_m = \frac{1}{\omega_{R,min}} \qquad\qquad \rho_1 = \frac{1}{\omega_{R,max}}. \tag{4.1}$$

considering the reduced experimental time interval of frequency $[\omega_{R,min}, \omega_{R,max}]$. The number of equally spaced intervals N, was increased repeatedly, until the minimum of the average square deviation SD (Eq. 2.88) between predicted and measured $G'(\omega)$ and $G"(\omega)$ was reached, as shown in Fig. 4.1. As can be observed from Fig. 4.1, increasing the number of modes, starting from the minimum number of 2, the SD decreases sharply until a certain point for which a minimum value is reached. This minimum SD value represents the noise of the experimental data and cannot be decreased even increasing more the number of modes.

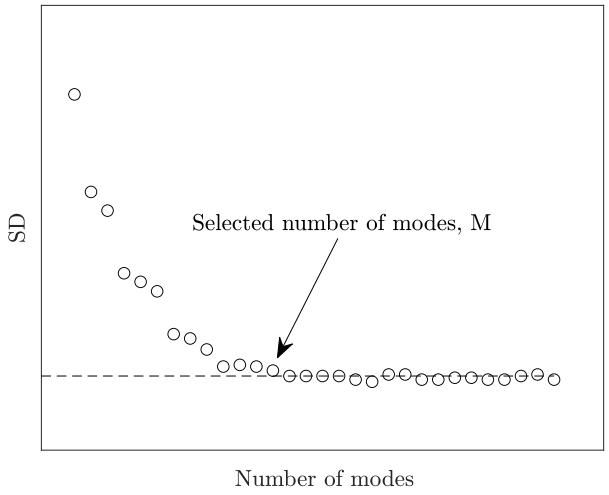

Figure 4.1 Average square deviation (SD) between predicted and measured $G'(\omega)$ and $G"(\omega)$ as a function of the number of modes N

The simple algorithm used and the spectra assessed, for each binder, are reported in appendix A. The success of the fitting procedure was evaluate by comparing the reconstructed curves with the experimental ones, as shown for binder B1 in the example of Fig. 4.2. All the curves obtained are reported then in appendix A. The algorithm allowed the determination of the relaxation spectrum for all the considered binders, with a number of elements ranging from 11 to 15 and avoiding negative relaxation strengths. Furthermore, the experimental data were directly used for the fitting, without involving the use of a model to describe the data in a continuous way, such as is frequently necessary when the Collocation Method is adopted.

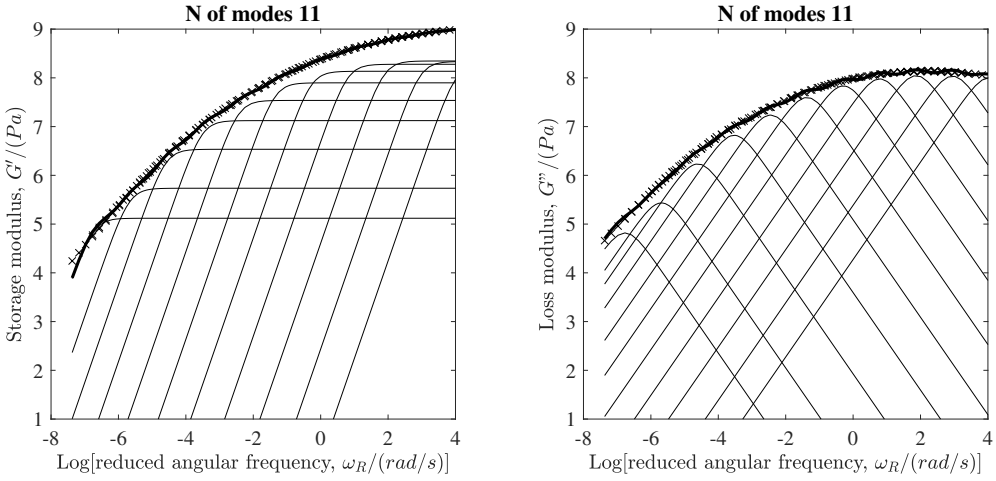

Figure 4.2 Relaxation spectrum of binder B1 for a reference temperature T_{ref} of $-15\,°C$

By knowing the relaxation spectrum for all the materials tested, the pseudo strain can be easily assessed, and the stress-pseudo strain curves were built. When the material behaves as linear viscoelastic, the stress-strain curve becomes a straight line in the stress-pseudo strain

space, and in this case the bisector since G_R is equal to 1. Analysing the results, it was observed that under certain circumstances the experimental curve in the stress-pseudo strain space deviates from the straight line, as shown in Fig. 4.3. This results was addressed to the fact that, for a certain level of strain, the response becomes non linear, due to the occurrence of non linear viscoelasticity and/or damage. In terms of deformation energy, it means that in such conditions there is an additional amount of energy dissipated, along with that dissipated by the linear viscoelasticity. Two energies are defined in the stress-pseudo strain space: (1) the pseudo strain energy density w^R and (2) the linear viscoelastic pseudo strain energy density w^R_{LVE}.
The pseudo strain energy density w^R is determined as the area under the stress-pseudo strain curve as

$$w^R = \int_0^t \tau(t) d\gamma^R. \tag{4.2}$$

and represents the deformation energy per unit volume of the material.
The linear viscoelastic pseudo strain energy density w^R_{LVE} defines the potential energy per unit volume the material could store if would behave as linear viscoelastic. The w^R_{LVE} is assessed as

$$w^R_{LVE} = \frac{\tau_F \, \gamma^R_F}{2} \tag{4.3}$$

where τ_F and γ^R_F are the failure stress and pseudo strain respectively. The two energies are displayed in Fig. 4.3.

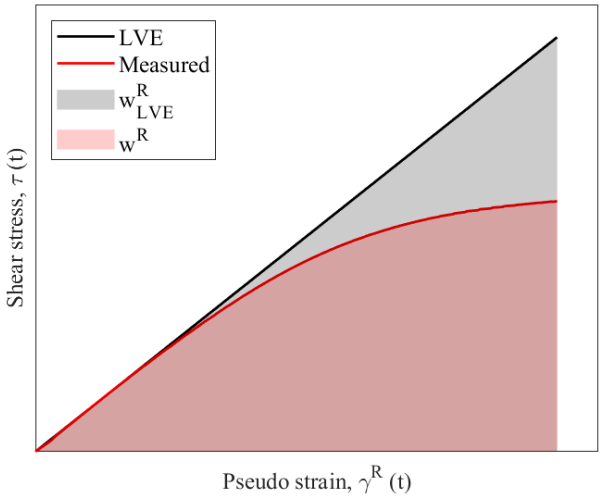

Figure 4.3 Actual and linear viscoelastic pseudo strain energy density

Following the energy approach, the ratio between the two energies quantifies the material's brittleness and was termed brittleness index I_B

$$I_B = \frac{w^R}{w^R_{LVE}}. \tag{4.4}$$

The I_B index of Eq. 4.4 is equal to its maximum value of 1 when the response is purely brittle and decreases as the energy dissipation before failure, and therefore the ductility, increases.
The I_B was assessed for each test in the stress-pseudo strain space, solving Eq. 4.4. A correction factor $\bar{f}_{ad\,j}$ was applied to the results for the specimen-to-specimen variability, defined as

$$\bar{f}_{ad\,j} = \frac{1}{K}\sum_{j=1}^{K}\frac{|G^*|_{mod}(\omega_j)}{|G^*|_{meas}(\omega_j)} \tag{4.5}$$

where $|G^*|_{mod}$ is the modelled modulus and $|G^*|_{meas}$ is the measured modulus, for the frequency ω_j, and K is the number of experimental frequencies.
The I_B results obtained are shown in Fig. 4.4, for the four materials, as a function of temperature and strain rate. Consistently with the expectations, the index increased as the temperature was decreased and/or the strain rate increased, until its maximum value of 1.

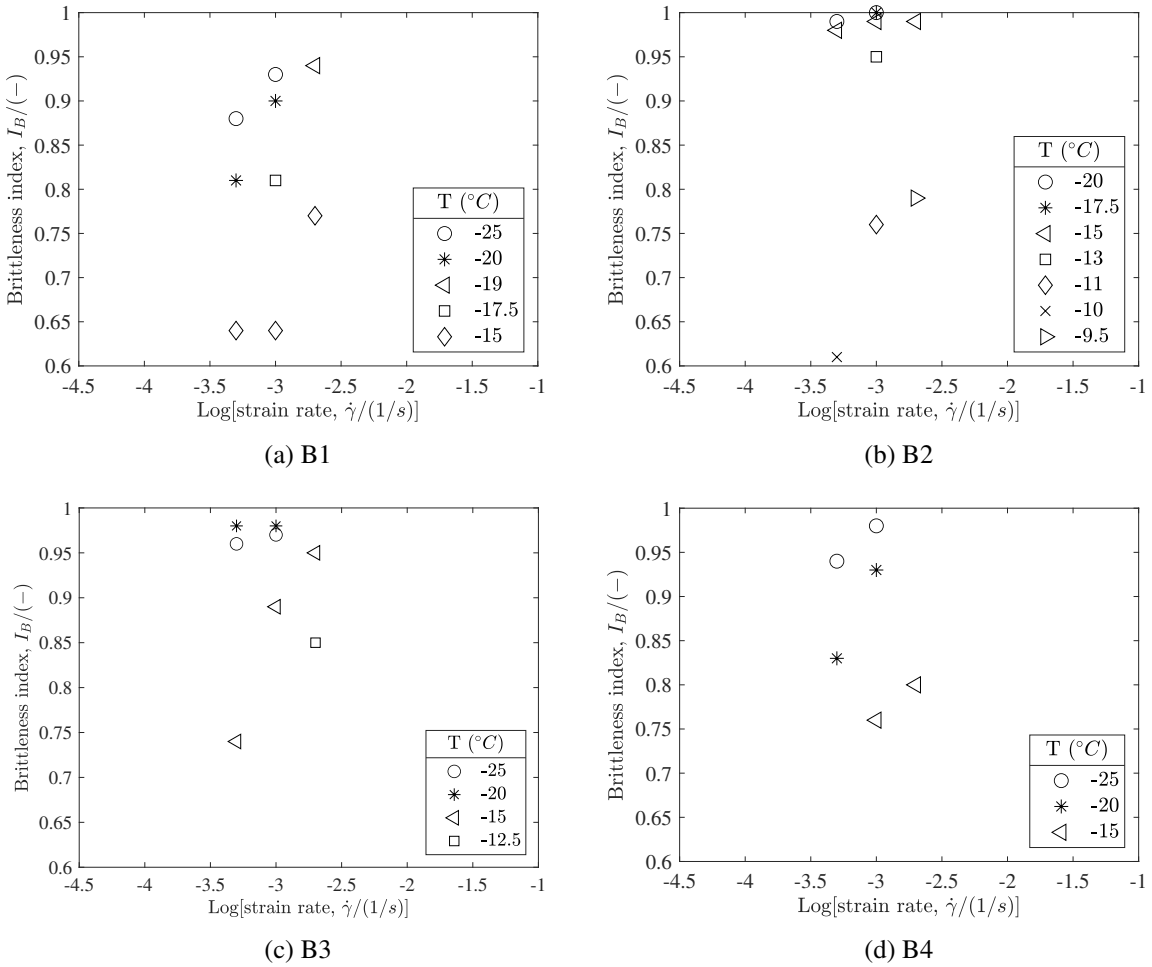

(a) B1 (b) B2

(c) B3 (d) B4

Figure 4.4 Brittleness index

4.2 Failure master curves: loading time-temperature superposition

The MTL results, in terms of stress and strain at failure, shown in Fig. 3.10 to 3.13, suggested the applicability of the TTSP. Therefore, the shift factors assessed to build the linear viscoelastic master curves, reported in Table 3.2, were used to horizontally shift the points, for the reference temperature $-15\,°C$. The resulting failure master curves are shown in Fig. 4.5. A continuos curve was obtained for all the materials tested, validating the applicability of the TTSP on the failure shear stress and strain. The failure strain curves of Fig. 4.5 show a similar trend for all the materials tested, decreasing monotonically as the strain rate increases as expected. Conversely, for the investigated conditions, the failure stress curves do not show the same for all the materials investigated:

- binders B1 and B3 presented a continuous growth of the isothermal stress at failure, as the strain rate increases;
- binder B2 exhibits a first upward trend, followed by a fluctuation around 5×10^3 kPa;
- the SBS-modified binder B4 presented an increasing failure stress until a peak value, after which the failure stress starts to decrease.

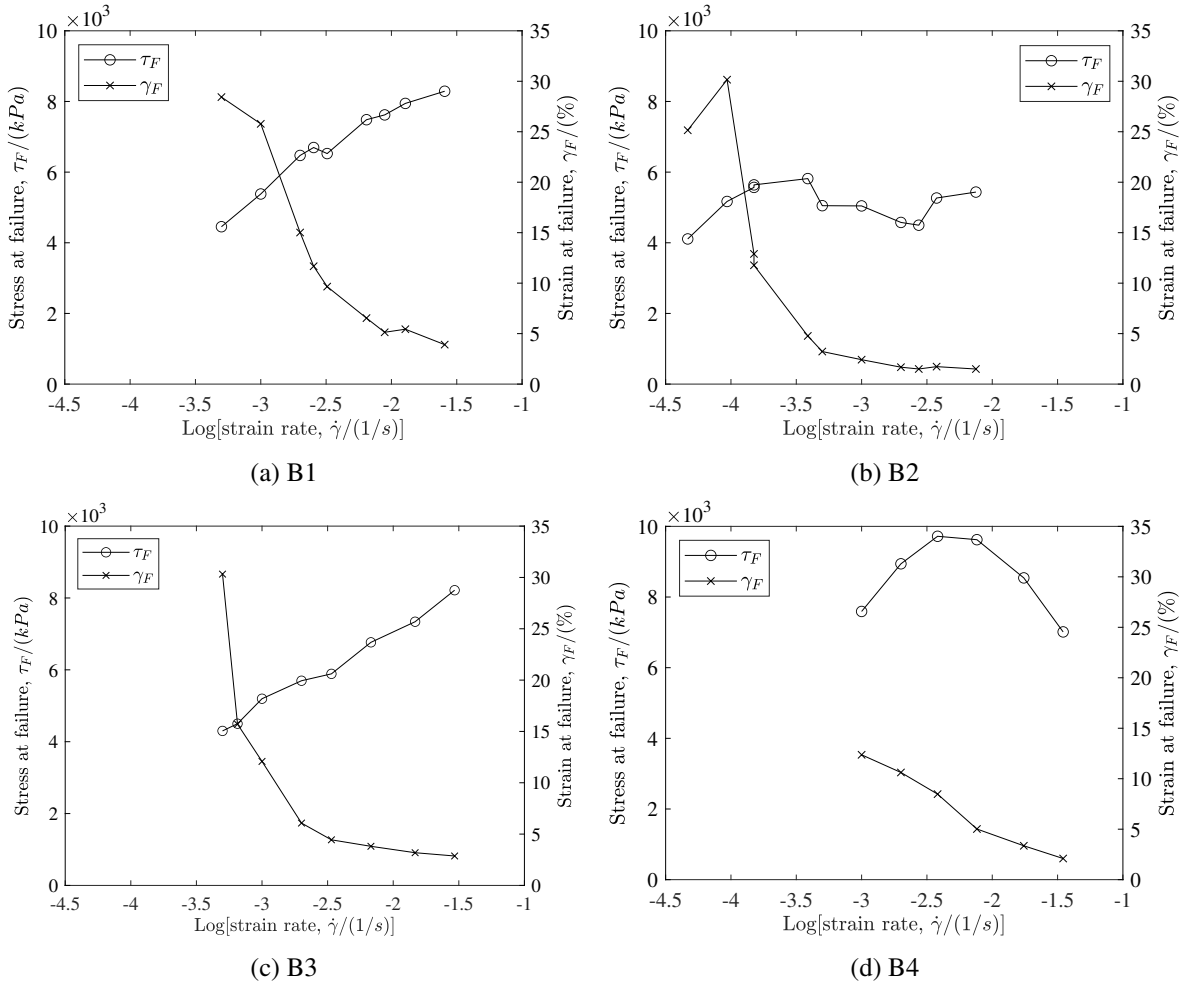

(a) B1 (b) B2

(c) B3 (d) B4

Figure 4.5 Failure shear stress and strain, at a reference temperature T_{ref} of $-15\,°C$

The following explanation can be considered.

The MTL test is based on continuum mechanics theory, thereby assuming the specimen as a continuum. In such context, the isothermal failure stress increases monotonically as the strain rate increases, due to the time-dependency, until the maximum strength is reached. After that, the stress remains constant and equal to its maximum value if the strain rate is further increased. A specimen without internal defects, strictly speaking, is not realizable experimentally and therefore, the specimen can fail before reaching its maximum strength value for crack propagation. This is particularly significant for brittle materials, which are highly sensitive even to very small inhomogeneities and leads the experimental determination of the failure strength extremely complex to achieve. Following these considerations, in the case of binder B1 and B3, the failure stress was not affected by internal crack propagations, and the trend resulted to be monotonic. Differently, for binder B2 and B4, the stress, after a certain point, starts to decrease. This is particularly prominent for binder B4, probably due to the SBS modification, which causes the internal inhomogeneities to be more significant. Comparing the materials in terms of strength, binder B2 showed the lowest failure stress and binder B4 the highest, consistently with the effects of the SBS modification.

Observing the failure master curves of Fig. 4.5, several considerations can be made about the

failure responses of the different binders. For the purpose, consider a fixed strain rate value of $0.001\,\mathrm{s}^{-1}$. Binder B1 has the highest failure strain, between 25 % and 30 %, followed by binders B3 and B4, showing a failure strain between 10 % and 15 %. Binder B2 appears to be the most brittle, with the lowest failure strain of about 2 %. Regarding the failure stress, the three unmodified binders, B1 B2 and B3, show roughly the same failure stress (around 5×10^3 kPa), even though the value seems to be the maximum strength for binder B2 with respect to the other two materials. Conversely, the modified binder B4 reaches the highest strength of almost 8×10^3 kPa, for the conditions considered, as expected due to the polymer modification.
The brittleness index I_B was shifted in a similar way to construct master curves, since the parameter derives from the failure stress and strain. The curves are given in Fig. 4.6. As can be observed, also for the index the curves were continuous, thus validating the applicability of the TTSP.

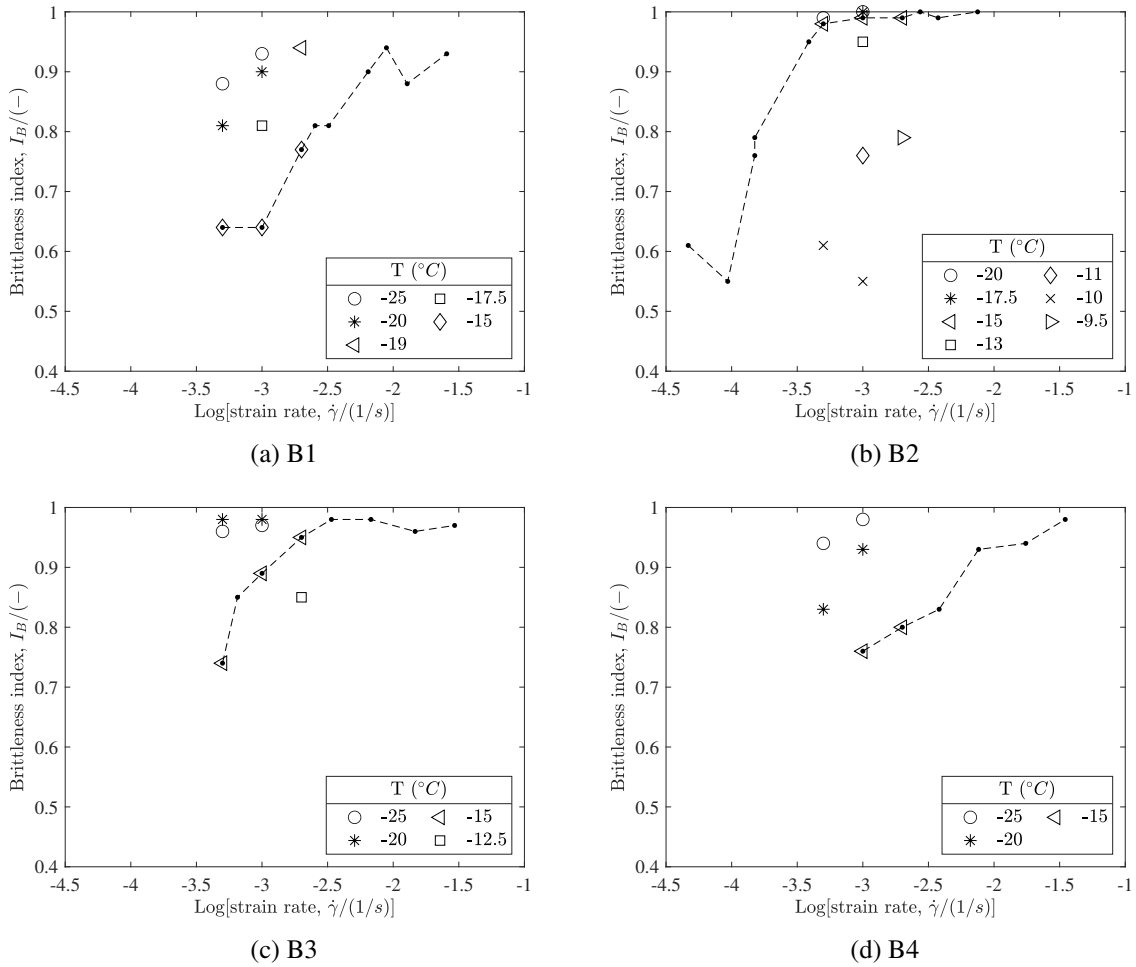

Figure 4.6 Brittleness master curves at a reference temperature T_{ref} of $-15\,°\mathrm{C}$

It can be observed from Fig. 4.6 that the isothermal I_B increases with the increase in strain rate, until the maximum theoretical value of 1 (i.e. purely brittle response) is approached. The three regions of behaviour, detected from the stress-strain curves, as was shown in Fig. 3.8, where identified using the brittleness master curves, by observing the experimental results. For

I_B greater than 0.95 the response was observed to be prevalently brittle, identifying the brittle region. On the other hand, a response largely ductile was detected when the I_B value decreases lower than 0.75. Therefore, the region identified by I_B between 0.75 and 0.95 was defined as the ductile-brittle transition region (or quasi-brittle).

4.3 MTL critical temperature

The scope of the analysis was to determine an easy parameter to rank the binders in terms of thermal cracking performance. For the purpose, the brittleness master curves were used. Theoretically, the critical condition of the MTL results would be the combination of time and temperature leading to approach the maximum I_B of 1. However, it was observed that the experimental results start to be scattered in the brittle region due to the increase of the sensitivity to internal inhomogeneities and therefore the quasi-brittle region was considered for the determination of the critical condition. Since a linear trend of the I_B semi-logarithmic curve was observed in the quasi-brittle region, the strain rate corresponding to an I_B equal to 1 was extrapolated by linearly interpolating the shifted experimental points falling in this interval. The methodology is graphically illustrated in Fig. 4.7. The resulting critical condition is a point defined as $(\dot{\gamma}, T)_{cr}$, where the temperature is equal to the T_{ref} selected for the master curve and the strain rate is determined, as explained, through linear interpolation. Furthermore, the slopes of the interpolated lines show that binders B1 and B4 approach gradually the brittle condition, with respect to binder B2 and B3. The validity of the TTSP allows to plot this critical point $(\dot{\gamma}, T)_{cr}$ assessed, as a function of temperature and strain rate. Therefore, by means of the shift factors of Table 3.2 the critical point can be expressed as

$$(\gamma_{cr}, T_{cr}) = (a_T\, \gamma_{cr}, T)\,. \tag{4.6}$$

The resulting plot, shown in Fig. 4.8, allows to characterize the susceptibility to thermal cracking for each material by fixing a value for the strain rate (or for the temperature) and determining the corresponding critical parameter (in terms of temperature or strain rate). Observing Fig. 4.8 and considering a fixed strain rate, binders B1 and B4 show a similar low temperature resistance, having the lowest critical temperatures. Binder B2 appears to be the most prone to thermal cracking, whereas the soft binder B3 presents an intermediate critical condition. Unexpectedly, the unmodified binder B1 resulted to have similar performances at low temperatures than the SBS-modified binder B4.

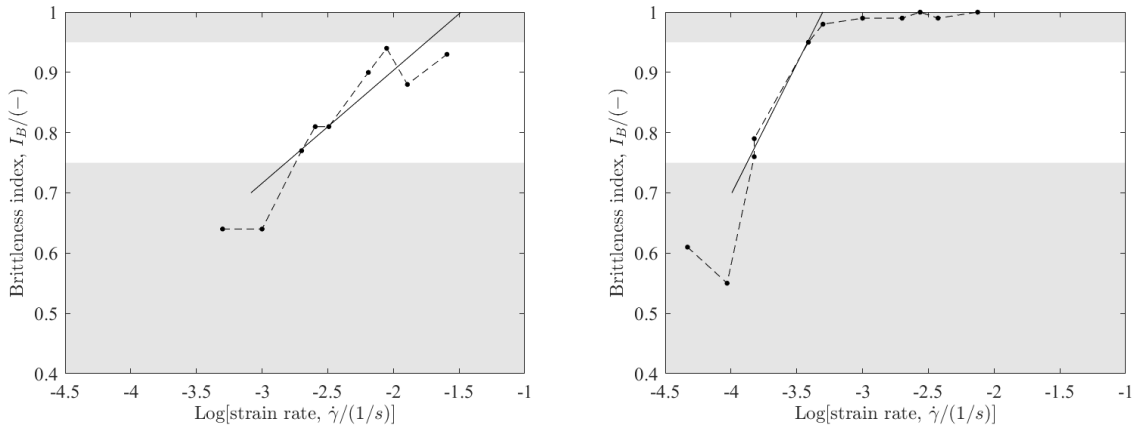

(a) B1 (b) B2

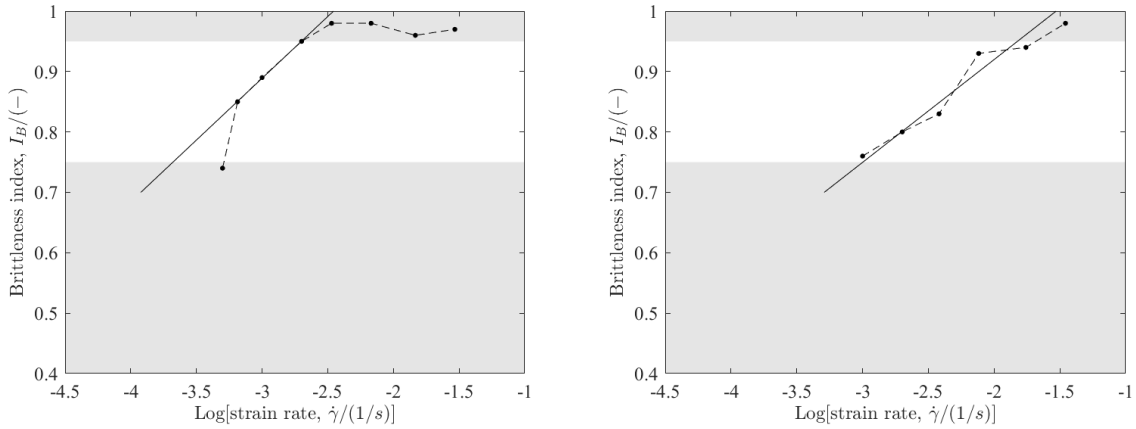

(c) B3 (d) B4

Figure 4.7 Determination of the critical point

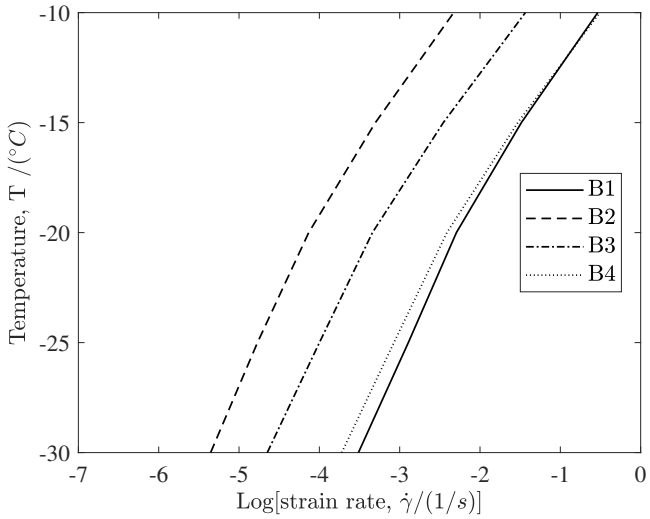

Figure 4.8 Critical point as a function of temperature and strain rate

For the purpose of comparison, a critical temperature was determined for each material by fixing the strain rate equal to $0.001\,s^{-1}$, and it was labelled as $T_{cr,MTL}$. Outcomes are reported in Table 4.1. Binder B1 showed the lowest $T_{cr,MTL}$ of $-26.4\,°C$, slightly lower than the SBS-modified binder B4. Binder B2 was instead the most fragile, with the highest $T_{cr,MTL}$ of $-14.4\,°C$.

Table 4.1 MTL critical temperature for a strain rate of $0.001\,s^{-1}$

Binder	$T_{cr,MTL}\,(°C)$
B1	-26.4
B2	-14.4
B3	-19.1
B4	-24.7

The temperatures obtained were compared to the glass transition temperature values, assessed in the previous section 1.3. The comparison is shown in Fig. 4.9. As already remarked, the T_g assessed through the two different techniques described in section 1.3, showed a good correlation for all the materials tested, with no difference in their corresponding ranking order. The $T_{cr,MTL}$ resulted to be in agreement with the determined T_g, for binders B1 B2 and B3. Conversely, in the case of modified binder B4 a significant difference was observed, with a T_g value approximately 10 °C lower than the T_g. Such an outcome suggests that T_g values assessed through the procedures described in section 1.3 may be unable to capture the contribution of SBS polymers to the improvement of low temperature performance. Thus, by means of the MTL methodology and related modelling the enhanced toughness deriving from polymer modification is duly highlighted, leading to realistic lower values of the critical failure temperature.

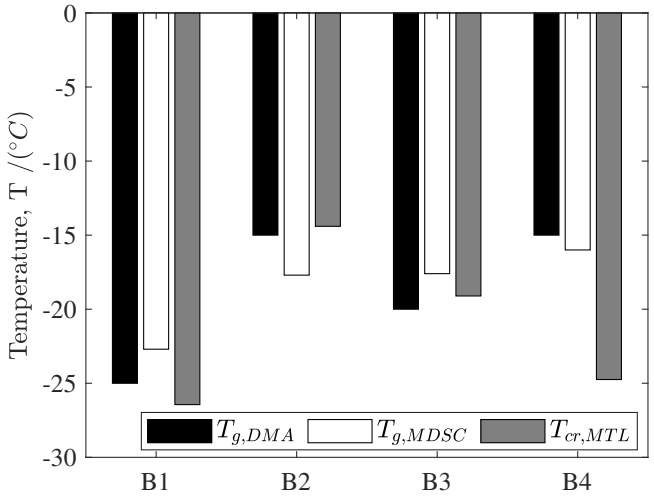

Figure 4.9 Comparison between the MTL critical temperature for a strain rate equal to $0.001\,s^{-1}$ $T_{cr,MTL}$ and the glass transition temperature T_g

Chapter 5

Statistical analysis of results

The use of statistics represents an important tool when designing failure test methods, in particular for brittle materials due to low test precision. The test precision is defined in the ASTM E456-13a specification as "the closeness of agreement between independent test results obtained under stipulated conditions" [97]. The *repeatability* refers to "conditions where independent test results are obtained with the same method on identical test items in the same laboratory by the same operator using the same equipment within short intervals of time". Conversely, the *reproducibility* conditions are "conditions where test results are obtained with the same method on identical test items in different laboratories with different operators using different equipment". The scope of this analysis was to perform several MTL tests under repeatability conditions to evaluate data distributions and to estimate the test repeatability.

5.1 Experimental design

Several MTL replicates were performed under repeatability conditions. The tests were carried out in the laboratory of road materials of "Politecnico di Torino" by a single operator, using a 4 mm DSR AntonPaar MCR302. The experimental plan is summarized in Table 5.1. Four samples were designed for the experimental investigation, in order to evaluate the effect of different aspects on the results. Three material were selected, the two unmodified B2 and B3 and the SBS-modified binder B4 (Table 3.1). The test conditions were selected in order to obtain a brittle response for the first three samples (X_1 X_2 and X_3) and a quasi-brittle response for the fourth sample (X_4). Based on the results of the previous investigation reported in section 4.3, the combinations of temperature and strain rate were selected to obtain a brittleness index $I_B \approx 1$ for the first three samples and $0.75 < I_B < 0.95$ for the fourth sample. The sample size n (i.e. the number of replicates) was selected as 49 for the first sample x_1 and reduced to 30 for the other samples, after a preliminary analysis of the data standard deviation of the first sample.

Table 5.1 Experimental plan

Sample	Binder	Temperature (°C)	Strain rate $\left(s^{-1}\right)$	$I_B(-)$	Sample size
X_1	B2	-20	0.001	1	49
X_2	B3	-20	0.001	0.98	30
X_3	B4	-20	0.002	1	30
X_4	B4	-20	0.001	0.93	30

5.2 Data descriptors and distributions

Referring to section 3.3, the MTL test allows to determine the material LVE properties during the fingerprint of phase 2 and the failure properties, leading the specimen to fail for monotonic torsional load in phase 3. The variables considered for the analysis were:

1. the norm of complex modulus $|G^*|$ for the angular frequency of $10\,\mathrm{rad\,s^{-1}}$;
2. the phase angle δ for the angular frequency of $10\,\mathrm{rad\,s^{-1}}$;
3. the failure shear stress τ_F;
4. the failure shear strain γ_F.

Generally speaking, suppose X a sample for the random variable x, composed by N observations. The sample mean $\bar{X}$ gives a measure of data centrality and is calculated as

$$\bar{X} = \frac{1}{N}\sum_{i=0}^{N} x_i, \tag{5.1}$$

where x_i is the i-th observation for the variable x. The mean could not always be the most appropriate descriptor of the "centre" of a data set and for some purposes, the median may be better, especially in small data sets. The median of X gives the midpoint of sorted data, so half of the data is greater than the median and half is smaller. The median is equal to the mean when the data are distributed symmetrically. The standard deviation s measures the spread in the data and has the same units as the mean value. It is expressed as

$$s = \sqrt{\frac{\sum_{i=0}^{n}\left(x_i - \bar{X}\right)^2}{n-1}}. \tag{5.2}$$

Since the mean and the standard deviation are expressed in the same units, the coefficient of variation (COV) is introduced as the ratio of the standard deviation and the mean, to represent the dispersion of the distribution dimensionless, as

$$COV = \frac{s}{\bar{X}}. \tag{5.3}$$

A smaller value of the COV indicates a smaller amount of randomness in the variable, and a larger amount indicates a larger amount of uncertainty. The interquartile range (IQR) is a measure of the spread for non-symmetric distributions since it gives the distance between the 25^{th} percentile and the 75^{th} percentile. In other words, it is the width of the region that contains the 50 % of the data. Lastly, the skewness coefficient θ_X gives the measure of the asymmetry of the data distribution around the mean and is assessed as

$$\theta_X = \frac{\frac{1}{N}\sum_{i=0}^{n}(x_i - \bar{X})^3}{s^3}. \tag{5.4}$$

When the skewness is negative, the data spreads out more below the mean and if it is positive more above the mean. The skewness of any perfectly symmetric distribution is zero. Outliers may be present in the sample, deriving from measurement errors and several methods can be used to detect and remove them. The interquartile method was used, which defines outliers the observation that fall outside the following range

$$Q_1 - 1.5\,IQR < x_{m,i} < Q_3 + 1.5\,IQR, \tag{5.5}$$

where Q_1 is the the lower 25^{th} percentile, Q_2 is the upper 75^{th} percentile and $x_{m,i}$ the i-th observation for the variable x of the sample m. The data descriptors were assessed for each variable, without considering the outliers, and the results are reported in Table 5.2 for $|G^*|$ and δ and in Table 5.3 for τ_F and γ_F. The summary statistics for each sample was plotted as box plots, as shown in Fig. 5.1 for sample X_1. Each box represents the interquartile range and the red marks inside each box are the median. The bottom edge indicates the lower 25^{th} percentile and the top edge the upper 75^{th} percentile. The whiskers extend to the most extreme data points not considered outliers. The box plots for all the samples are reported in appendix B.

Table 5.2 General statistics LVE properties

Sample	Variable	Mean	Median	s	COV (%)	IQR	θ_X
X_1	$\|G^*\|$(Pa)	5.25e+08	5.27e+08	1.03e+07	1.97	1.32e+07	0.30
	$\delta(^\circ)$	10.8	10.8	0.24	2.23	0.34	-0.23
X_2	$\|G^*\|$(Pa)	6.33e+08	6.32e+08	1.42e+07	2.24	1.69e+07	0.38
	$\delta(^\circ)$	9.7	9.6	0.24	2.52	0.34	0.39
X_3	$\|G^*\|$(Pa)	5.39e+08	5.40e+08	6.34e+06	1.18	8.39e+06	0.09
	$\delta(^\circ)$	8.6	8.6	0.07	0.86	0.11	0.17
X_4	$\|G^*\|$(Pa)	5.49e+08	5.47e+08	1.33e+07	2.42	1.82e+07	0.46
	$\delta(^\circ)$	8.6	8.6	0.12	1.37	0.13	-055

Table 5.3 General statistics failure properties

Sample	Variable	Mean	Median	s	COV (%)	IQR	θ_X
X_1	τ_F(kPa)	5.60e+03	5.61e+03	791.1	14.1	819.8	-0.18
	γ_F(%)	3.3	3.3	0.77	23.2	0.99	0.14
X_2	τ_F(kPa)	5.93e+03	6.01e+03	750.2	12.7	1.18e+03	0.03
	γ_F(%)	2.7	2.7	0.59	22.1	0.96	0.56
X_3	τ_F(kPa)	7.69e+03	7.83e+03	701.6	9.1	897.45	0.09
	γ_F(%)	2.9	2.9	0.38	13.1	51	0.28
X_4	τ_F(kPa)	6.72e+03	6.67e+03	925.37	13.77	1.37e+03	0.01
	γ_F(%)	2.9	2.9	0.60	20.9	0.84	0.64

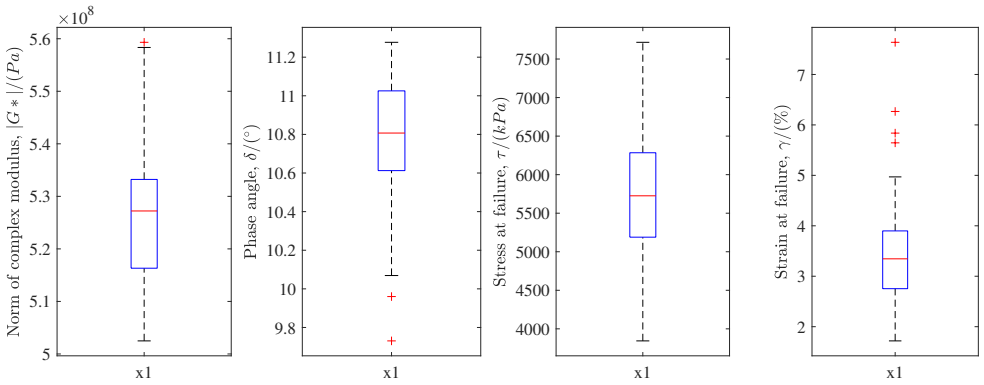

Figure 5.1 Box plots for sample X_1

By looking the mean values of Table 5.2 and remembering that the temperature was kept equal to $-20\,°C$ for all the samples investigated, it can be observed that binder B2 (sample X_1) showed the lowest $|G^*|$ value and the highest δ value for the considered frequency. Binder B3 (sample X_2) resulted to have the highest $|G^*|$ and the SBS modified binder (samples X_3 and X_4) the lowest value of δ. The mean values of the variables τ_F and γ_F of Table 5.3 were dependent not only on the temperature but also on the strain rate used to apply the monotonic load. However, the combination of temperature and strain rate was selected to obtain an iso-brittleness condition for samples X_1, X_2 and X_3. Sample X_3 showed the highest average τ_F, as expected for the SBS-modified binder. The γ_F appeared to be around 3 % for all the samples. Comparing the mean values with the median values, it can be observed that for all the variables the data distributions were mostly symmetrical. The same information was given by the skewness coefficient, from which it can also be observed that for the majority of the cases the data spread out above the mean (skewness coefficient positive). The coefficient of variation was around: 2 % for both the LVE properties; 10 % for the failure stress and about 20 % for the failure strain. Even though it appears that the COV is high for failure properties, it has to be remembered that failure test methods are inherently noisy procedures which are always linked to higher variability, particularly for brittle materials.

To evaluate the relationship between the variables, the correlation coefficient was assessed. The correlation coefficient of two random variables is a measure of their linear dependence and is defined as

$$\rho(A,B) = \frac{1}{N-1}\sum_{1}^{N}\left(\frac{A_i - \bar{X}_A}{s_A}\right)\left(\frac{B_i - \bar{X}_B}{s_B}\right) \tag{5.6}$$

or equivalently in terms of covariance COV as

$$\rho(A,B) = \frac{COV(A,B)}{s_A\, s_B}. \tag{5.7}$$

Therefore, the correlation matrix of two random variables is expressed as

$$\begin{pmatrix} \rho(A,A) & \rho(A,B) \\ \rho(B,A) & \rho(B,B) \end{pmatrix} \tag{5.8}$$

and, since A and B are always directly correlated to themselves, the diagonal entries are equal to 1, such that

$$\begin{pmatrix} 1 & \rho(A,B) \\ \rho(B,A) & 1 \end{pmatrix}. \tag{5.9}$$

Considering the random variables $|G^*|$, δ, τ_F and γ_F, the correlation matrices $\rho(|G^*|,\delta,\tau_F,\gamma_F)$ for all the samples (respectively $\rho(X_1)$, $\rho(X_2)$, $\rho(X_3)$ and $\rho(X_4)$ for sample X_1, X_2, X_3 and X_4) are:

$$\rho(X_1) = \begin{pmatrix} 1 & -0.47 & 0.07 & -0.17 \\ -0.47 & 1 & 0.40 & 0.57 \\ 0.07 & 0.40 & 1 & 0.93 \\ -0.17 & 0.57 & 0.93 & 1 \end{pmatrix} \quad \rho(X_2) = \begin{pmatrix} 1 & -0.50 & -0.10 & -0.32 \\ -0.50 & 1 & 0.40 & 0.58 \\ -0.10 & 0.40 & 1 & 0.96 \\ -0.32 & 0.58 & 0.96 & 1 \end{pmatrix}$$

$$\rho(X_3) = \begin{pmatrix} 1 & 0.01 & 0.17 & -0.31 \\ 0.01 & 1 & 0.06 & 0.14 \\ 0.17 & 0.06 & 1 & 0.98 \\ -0.31 & 0.57 & 0.98 & 1 \end{pmatrix} \quad \rho(X_4) = \begin{pmatrix} 1 & 0.14 & -0.26 & -0.45 \\ 0.14 & 1 & -0.01 & 0.08 \\ -0.26 & -0.01 & 1 & 0.99 \\ -0.45 & 0.08 & 0.99 & 1 \end{pmatrix}.$$

As can be observed the two variables τ_F and γ_F resulted to be strongly correlated for all the sample investigated, with a correlation coefficient ranging from 0.93 to 0.99. To visualize the correlation, the γ_F was plotted against τ_F and the results are shown in Fig. 5.2. The outliers are shown in the graphs as red crosses.

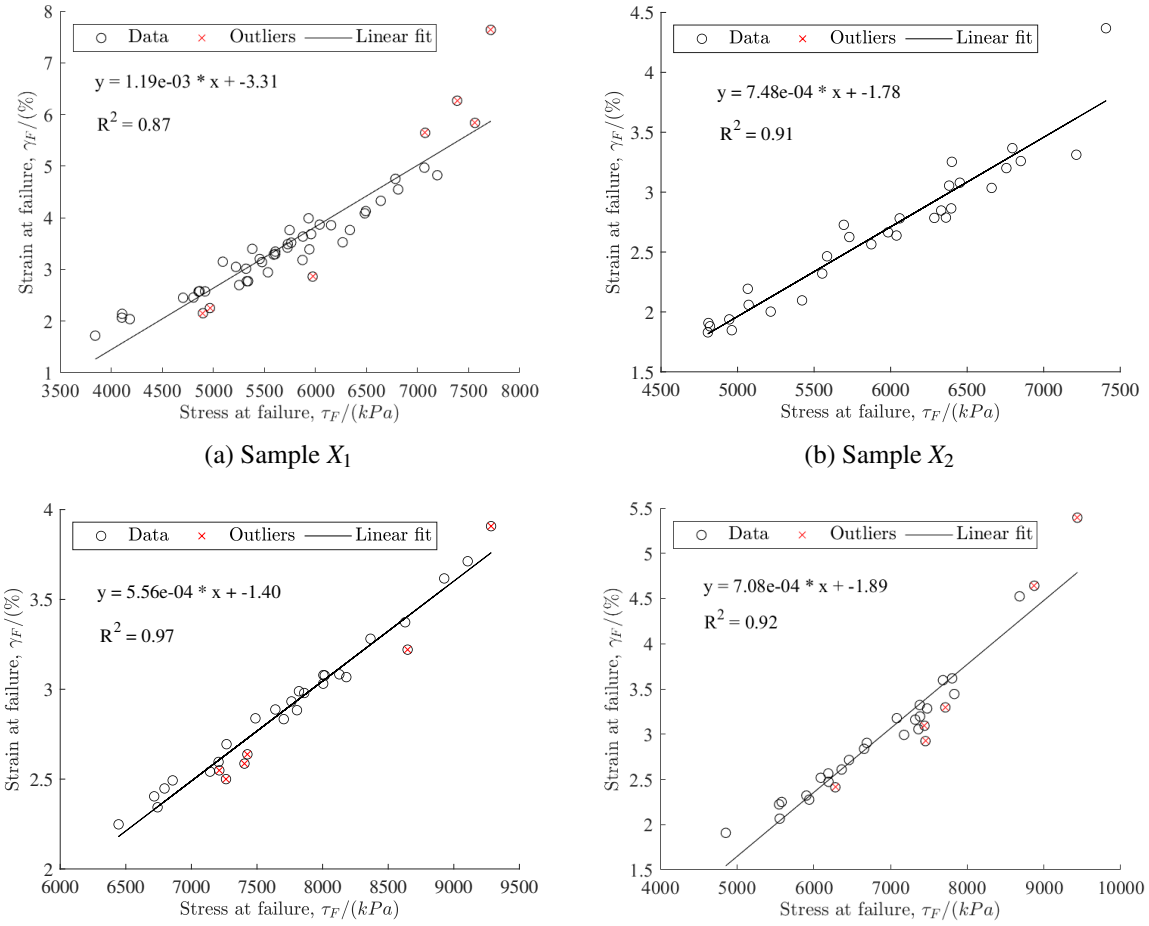

(a) Sample X_1

(b) Sample X_2

(c) Sample X_3

(d) Sample X_4

Figure 5.2 Plot of failure stresses as a function of failure strains

Three distributions were considered in describing the data: the normal distribution, the log-normal distribution and the Weibull distribution. Due to the high correlation coefficient between τ_F and γ_F, only one of the two variables was considered for the analysis. It was observed that the data can be described adopting the normal distribution. The empirical Cumulative Distribution Function (CDF) was built and compared with that referred to the normal distribution. The CDF was selected with respect to the histogram since the variables considered were continuous. The results were in the form of that shown in Fig. 5.3 for sample X_1, and the curves for all the samples are reported in appendix B. The probability plot technique [99] was also used to evaluate the normal distribution. The plots involve to represent the data points against the theoretical distribution, such that the points should form approximately a straight line. The deviation from this line indicates departures from the selected distribution. The plots of sample X_1 are shown as an example in Fig. 5.4. Similar results were obtained for the other samples and the graphs are shown in appendix B.

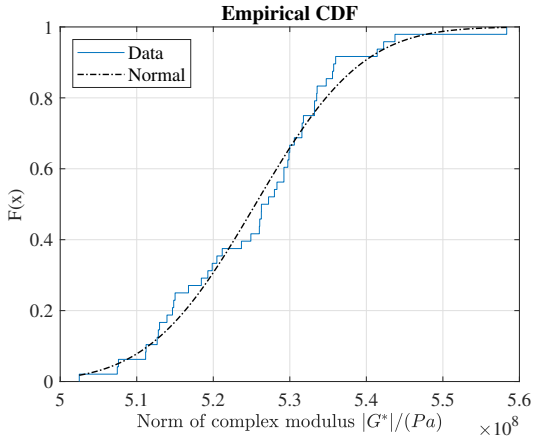

(a) Norm of complex modulus

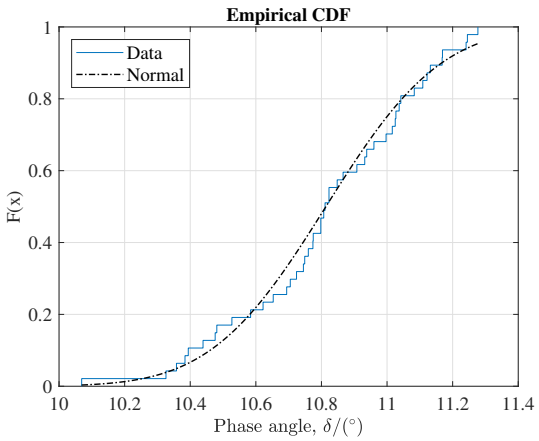

(b) Phase angle

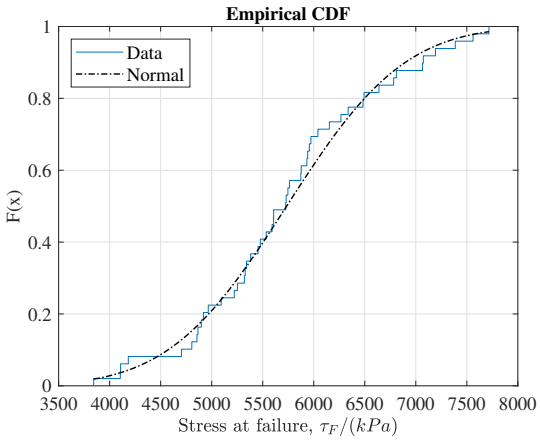

(c) Failure stress

Figure 5.3 CDF for sample X_1

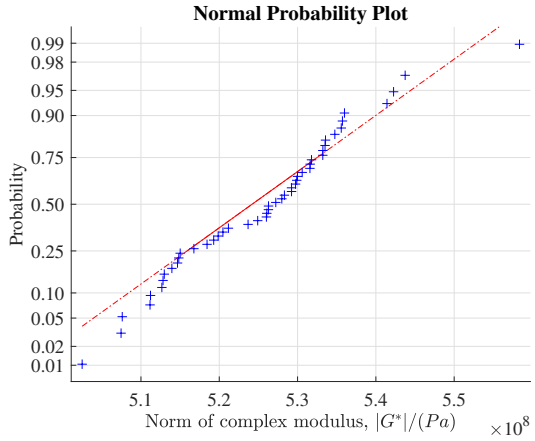

(a) Phase angle

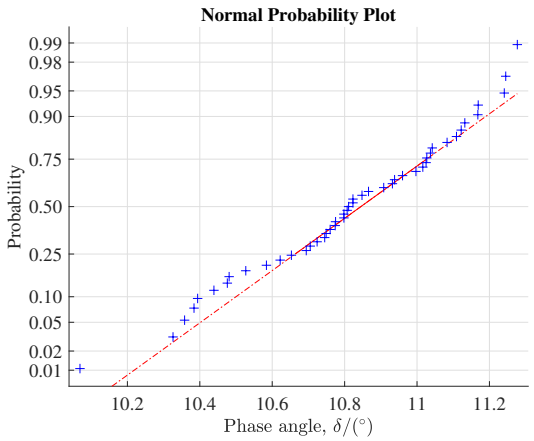

(b) Norm of complex modulus

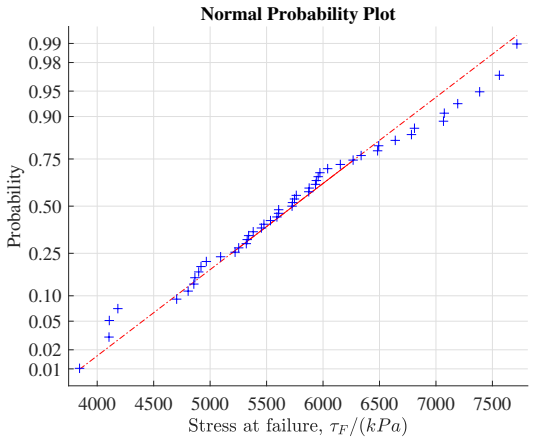

(c) Failure stress

Figure 5.4 Probability plots for sample X_1

As can be noticed both from the CDF and the probability plots, the data seemed to be normal distributed for all the variables. The Lilliefors test was used to test the hypothesis that the data sets fit a normal distribution. The Lilliefors test verify that the following coefficient is lower than a fixed critical value

$$D^* = \max |\hat{F}(x) - G(x)|, \tag{5.10}$$

where $\hat{F}(x)$ is the empirical cdf of the sample data and $G(x)$ is the cdf of the hypothesized distribution with estimated parameters equal to the sample parameters. The test indicated that the normal distribution is suitable for describing the data, with a significant level of 5 %.

5.3 Test repeatability

The test repeatability was determined, following the specifications ASTM C670 [100]. Two parameters represent test precision in terms of repeatability: (1) the repeatability standard deviation (1s or 1s%) and (2) the repeatability limit ($d2s$ or $d2s$%). The $d2s$ indicates the

maximum difference between two acceptable results, such that

$$(\bar{X}_1 - \bar{X}_2) - d2s < \mu_1 - \mu_2 < (\bar{X}_1 - \bar{X}_2) + d2s, \tag{5.11}$$

where $\bar{X}_1$ and $\bar{X}_2$ are the sample means and μ_1 and μ_2 are the corresponding population means, and is expressed as

$$d2s = z_{(\alpha/2)}\, s_{(\bar{X}_1 - \bar{X}_2)}, \tag{5.12}$$

where $z_{(\alpha/2)}$ is the value of the normal distribution for the confidence interval α and $s_{(\bar{X}_1 - \bar{X}_2)}$ is the standard error of the difference means. The standard error of the mean indicates the standard deviation of the means distribution as

$$s_{\bar{X}} = \frac{\hat{\sigma}}{\sqrt{n}} \tag{5.13}$$

where $\hat{\sigma}$ is an estimate of the population standard deviation.
Considering n_1 independent measurements on sample 1 and n_2 independent measurement on sample 2, the standard deviation of the difference means is assessed, following Eq. 5.13, as

$$s_{(\bar{X}_1 - \bar{X}_2)} = \sqrt{\hat{\sigma}^2 \left(\frac{1}{n_1} + \frac{1}{n_2} \right)}. \tag{5.14}$$

Substituting Eq. 5.14 into Eq. 5.13 and selecting α equal to 0.05 and $n_1 = n_2 = 1$ the following expression can be obtained

$$d2s = 2.8\,(COV). \tag{5.15}$$

The standard deviation of the population was selected discussing the results obtained for the four samples for the failure variables, since the LVE COV does not change significantly among the samples. Considering the COV value reported in Table 5.3, two different parameters can be evaluated: (1) the material and (2) the failure mode. The comparison is shown in Fig. 5.5. It can be observed that no significant differences in terms of COV arise whether by looking to different materials or different brittleness conditions. The sample X_3 showed the lowest COV value and this may be linked to experimental issues: the tests of sample X_3 were the lasts to be performed and the experimental procedure was handled more and more carefully moving forward. For this reason, the sample X_3 standard deviation was used for the analysis as the best estimate of the population standard deviation.

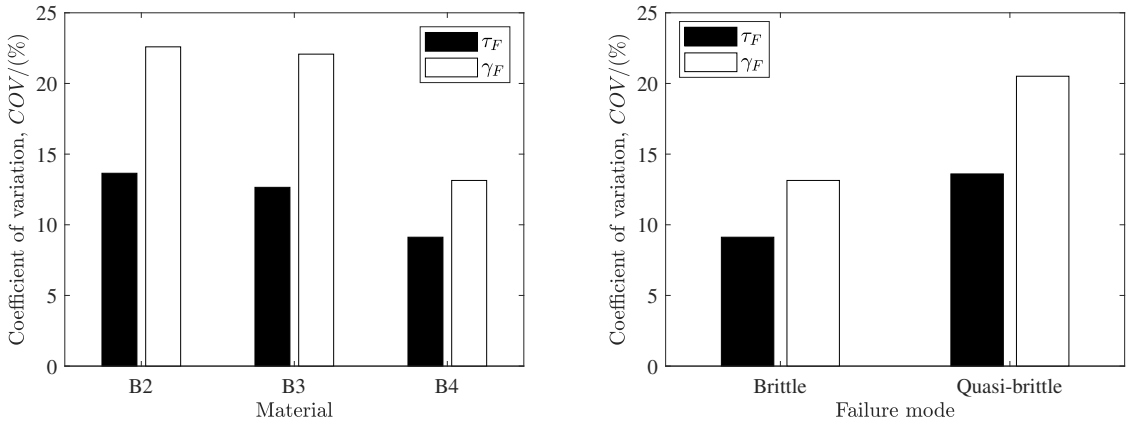

(a) COV as a function of the material

(b) COV as a function of failure mode for binder B4

Figure 5.5 Evaluation of the effect of different parameters on the COV value

The results obtained for the test repeatability are reported in Table 5.4. Outcomes are consistent with other failure tests on brittle materials, such as the DTT [26]. However, this study represents a starting point from which the procedure can be improved. In particular, it was observed that the results were strongly affected by the specimen preparation phase requiring the procedure to be handled carefully. The material needs to be degassed, to avoid the presence of air bubbles that could lead the specimen to fail prematurely for crack propagation. Furthermore, the mould, rebuilt for each test, has to be as similar as possible each test, in order to not affect the specimen geometry.

Table 5.4 Test repeatability

Variable	1s (%)	d2s (%)
$\lvert G^* \rvert$	1.18	3.3
δ	0.86	2.4
τ_F	9.1	25.3
γ_F	13.1	36.4

Chapter 6

The effect of chemical ageing

The asphalt binders *chemical ageing* is the non-reversible change of its internal chemical structure, during both pavement manufacture and service life. The material become stiffer and more brittle, being more prone to crack and therefore to lead to the premature failure of the pavement.Two ageing conditions can be distinguished: the short- and the long-term ageing. The short-term ageing refers to the process of storage, mixing, transport and laying, during which the material is exposed to air and high temperatures, causing significant thermal and oxidative reactions. The long-term ageing addresses the ageing phenomenon arising during the pavement service life, due to the exposure to environmental factors, mostly involving oxidation.
The chapter addresses the application of the MTL approach to aged binders, both considering short- and long-term ageing. Two main objectives can be drawn up for the experimental investigation:

1. characterize a set of asphalt binders through the MTL approach;
2. evaluate how the chemical ageing affects the MTL critical temperature.

6.1 Experimental plan

The same binders listed in Table 3.1 were adopted for the experimental investigation. Since the binder B2 was no longer available to be aged, an other binder with the same penetration grade 50/70 was used instead. Therefore, for binder B2 the comparison with the unaged binder is missing. The binders labelled B1, B2, B3 and B4 were subjected to the Rolling Thin Film Oven Test (RTFOT), shown in Fig. 6.1a, to simulate short-term ageing. The test was set following the AASHTO T240-13 specification [101]. The RTFOT involves subjecting a thin film of asphalt binder to the simultaneous effect of temperature and air for 85 min. A part of the RTFOT aged materials were afterward tested using the Pressurized Ageing Vessel (PAV), shown in Fig. 6.1b, according to the AASHTO R28-12 specification [102]. The PAV simulates the long-term ageing of binders by subjecting the materials to high pressures and high temperature for 20 h. The combined effect of temperature and pressure allows to estimate the properties of the binders after 5 to 10 years of in-service ageing in the field.

(a) Rolling thin film oven

(b) Pressurized ageing vessel

(c) Equipment for laboratory chemical ageing of asphalt binders

A preliminary characterization was carried out, for each material in both ageing conditions, addressing: (1) linear viscoelastic properties and (3) performance grade (PG). Therefore, frequency sweep tests were performed, using the DSR equipped with 8 mm parallel plates measurement system for temperatures ranging from 34 °C to 4 °C and with 4 mm parallel plates for temperatures between 4 °C and −30 °C. The angular frequencies were varied between 1 rad s^{-1} and 100 rad s^{-1}, for each step of temperature. The low temperature measurements were corrected for the compliance error, as explained in section 3.4. The determination of the PG, according to the AASHTO M320-17 specification [5], requires additional testing. For the purpose, frequency sweep tests were performed at higher temperatures ranging from 76 °C to 34 °C by means of the DSR equipped with the 25 mm parallel plates measurement system. The frequencies were also here varied between 1 rad s^{-1} and 100 rad s^{-1}. Furthermore, BBR creep tests were performed at different temperatures, following the AASHTO T313-12 specification [23], for the determination of the low temperature PG.

Following the preliminary characterization, the MTL tests were carried out to determine the MTL critical point, as shown in Fig. 4.7 for each binder, for both the RTFOT and the PAV ageing conditions. The experimental investigation was planned to identify at least three points falling in the range of interest, in order to obtain a consistent linear interpolation. For the purpose, the combinations of strain rate and temperature were varied, until the minimum number of useful points were obtained. Three strain rates were used, considering experimental limits and the preliminary investigation reported in ch. 3: (1) 0.0005 s^{-1}, (2) 0.001 s^{-1} and (3) 0.002 s^{-1}.The temperatures were selected for each material, based on the previous investigation, between −13 °C and −25 °C. The experimental plan is summarized in Table 6.1.

Table 6.1 Experimental testing to investigate low temperature performance of aged binders

Objective	Ageing	Test	Equipment
LVE	RTFOT PAV	Frequency sweep	DSR
High temperature PG	RTFOT PAV	Frequency sweep	DSR
Low temperature PG	RTFOT PAV	- 3-pt bending creep test	- BBR
$T_{cr,MTL}$	RTFOT PAV	MTL	DSR

6.2 Linear viscoelastic characterization

The frequency sweep data coming from low and intermediate temperature tests were analysed to evaluate the effect of both short- and long-term ageing on the linear viscoelastic properties of the considered binders. The so-called Black space was used for the preliminary evaluation of raw data and the resulting diagrams are shown in Fig. 6.2. For low temperatures, all the materials investigated, independently on the level of ageing, show a continuous Black curve, validating the applicability of the TTSP. Comparing the different ageing conditions to the unaged materials in Fig. 6.2, it can be observed that chemical ageing led the phase angle values to be lower, for a fixed value of the modulus. This means that, for the same conditions, the material become less and less capable to dissipate energy, as the grade of ageing increases. The comparison is missing for binder B2, as explained in section 6.1. Observing the diagrams of Fig. 6.2, it can be noticed that the effect of the most severe PAV ageing on LVE properties become clearly visible for phase angle values greater than about 20°. These condition corresponds to temperatures higher than -5 °C, considering the investigated frequencies. The raw data were then shifted horizontally, using the TTSP, to build linear viscoelastic master curves, selecting the (T_{ref}) equal to -15 °C. The horizontal shift factors were determined by means of the Kramers-Kronig relationship (Eq. 2.99) and are reported in Table 6.2 for the RTFOT aged materials and in Table 6.3 for the PAV aged materials. Fig. 6.3 reports the master curves referred to binder B1 and similar curves were obtained for all the materials. It can be observed that as the level of ageing increases, for the same frequency, the modulus increases while the phase angle decreases, since the material becomes stiffer and less capable to dissipate energy. The effect of ageing on the LVE properties becomes significant for the lowest frequencies, corresponding to the highest temperatures. At high frequencies, corresponding to low temperatures, the ageing did not affect the curves.

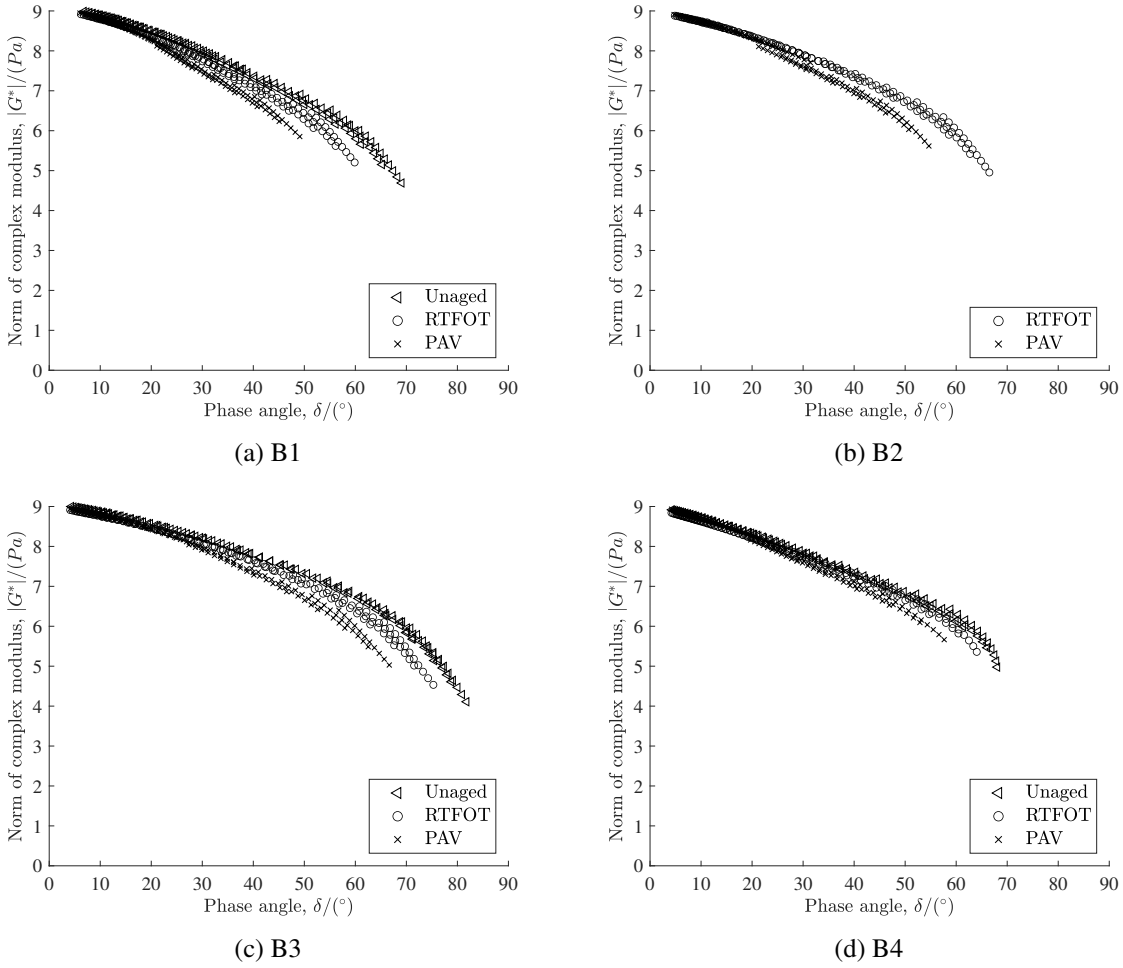

(a) B1 (b) B2

(c) B3 (d) B4

Figure 6.2 Black diagram

Table 6.2 Shift factors for RFTOT aged binders B1, B2, B3 and B4 at a reference temperature of −15 °C

Temperature (°C)	B1	B2	B3	B4
-30	1.94	2.06	2.12	2.20
-25	1.35	1.41	1.51	1.51
-20	0.75	0.78	0.88	0.91
-15	0	0	0	0
-10	-0.93	-0.99	-0.99	-1.03
-5	-1.83	-1.90	-1.90	-1.97
0	-2.70	-2.80	-2.71	-2.87
4	-3.45	-3.41	-3.34	-3.40
10	-4.32	-4.24	-4.17	-4.28
16	-5.12	-5.03	-4.94	-5.13
22	-5.89	-5.77	-5.65	-5.92
28	-6.62	-6.47	-6.29	-6.65
34	-7.23	-7.10	-6.88	-7.30

Table 6.3 Shift factors for PAV aged binders B1, B2, B3 and B4 at a reference temperature of −15 °C

Temperature (°C)	B1	B2	B3	B4
-30	2.00	2.06	2.11	2.18
-25	1.37	1.43	1.50	1.54
-20	0.76	0.78	0.87	0.87
-15	0	0	0	0
-10	-0.96	-1.00	-0.97	-1.01
-5	-1.85	-1.91	-1.90	-1.95
0	-2.74	-2.80	-2.74	-2.84
4	-3.47	-3.43	-3.53	-3.86
10	-4.35	-4.31	-4.39	-4.77
16	-5.19	-5.14	-4.18	-5.63
22	-5.99	-5.93	-5.91	-6.45
28	-6.74	-6.68	-6.60	-7.21
34	-7.44	-7.37	-7.22	-7.89

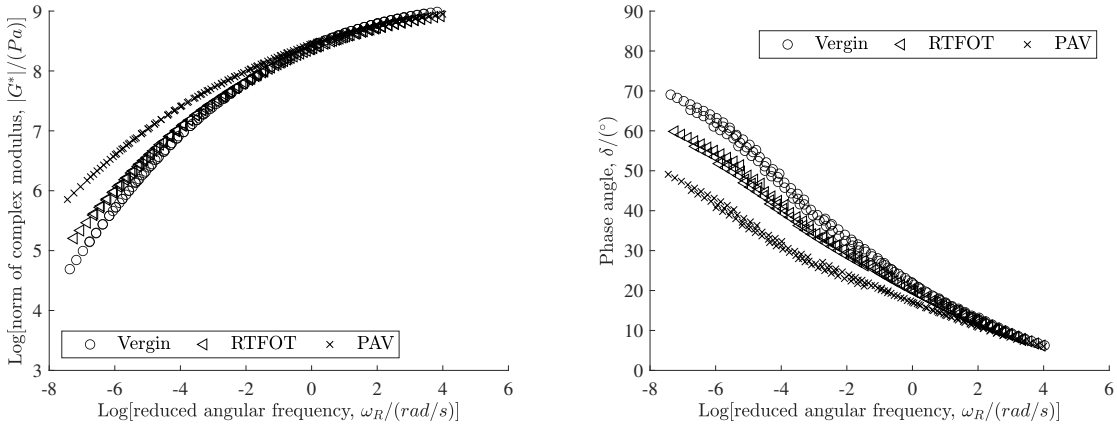

(a) Norm of complex modulus

(b) Phase angle

Figure 6.3 Master curves for binder B1 at a reference temperature of −15 °C

6.3 Performance grade

The PG was assessed for the selected materials, following the corresponding specifications [5, 22]. In particular, the low temperature PG was assessed by subtracting 10 °C to the lowest temperature for which the following conditions were met:

- $S(t)$ for 60 s lower than 300 MPa for the PAV ageing condition;
- $m-value$ for 60 s higher than 0.3 for the PAV ageing condition.

The results obtained are reported in Table 6.4. The low temperature PG resulted to be identical and equal to -22 °C for all the materials tested and therefore, the temperature for which the PG criterion failed was assessed and reported in Table 6.4. The $T_{cr,S}$ is the temperature referred to the stiffness criterion ($S(t) < 300$ MPa) and $T_{cr,m}$ the temperature related to the $m-value$ requirement ($m-value > 0.3$). These critical temperatures were determined by linear interpolating the BBR data points, as shown in Fig. 6.4 and the highest temperature is highlighted in Table 6.4. It can be observed from Table 6.4, that binder B4 appeared to be the most fragile, according to the PG grading, failing the $m-value$ criterion for the highest temperature of -12.4 °C. The $m-value$ criterion is the most critical also for binder B1, whereas binders B2 and B3 temperatures failed for the $S(t)$ criterion. Binder B3 showed an m-value greater than the limiting value 0.3, for both the temperatures investigated, consistently with its higher PEN. However, the difference between these critical temperatures is in the range of ± 3 °C, indicating that the PG grading did not highlight a significant difference in terms of thermal cracking performance among the investigated materials.

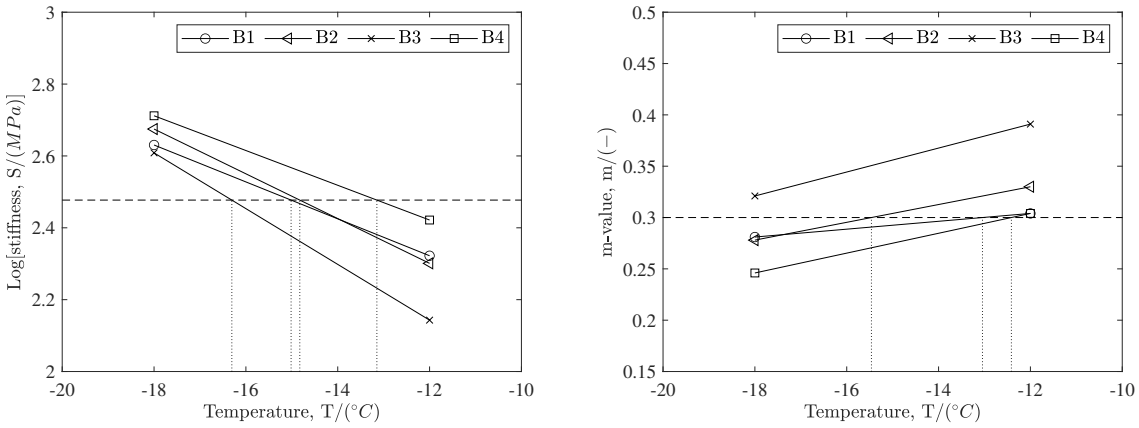

(a) Stiffness criterion

(b) m-value criterion

Figure 6.4 Determination of the PG critical temperature

Table 6.4 Performance grade PG

Binder Code	PG	$T_{cr,S}$ (°C)	$T_{cr,m}$ (°C)
B1	70-22	-15.0	$\mathbf{-13.0}$
B2	70-22	$\mathbf{-14.8}$	-15.5
B3	64-22	$\mathbf{-16.3}$	-
B4	76-22	-13.1	$\mathbf{-12.4}$

6.4 Determination of the MTL critical condition

The MTL stress-strain curves, obtained for each test, were corrected for the machine compliance, as explained in section 3.4. The index I_B was determined using Eq.4.4. The relaxation spectra,

needed to solve Eq.4.4, were determined using the same algorithm explained in section 4.1. The success of the fitting procedure was evaluate by comparing the reconstructed curves with the experimental ones, as shown for binder B1 in the example of Fig. 6.5. All the curves obtained are reported then in appendix A. The algorithm allowed the determination of the relaxation spectra for all the considered binders, with a few number of elements and avoiding negative relaxation strengths. The number of modes remains almost the same for all the binders, considering both the ageing conditions.

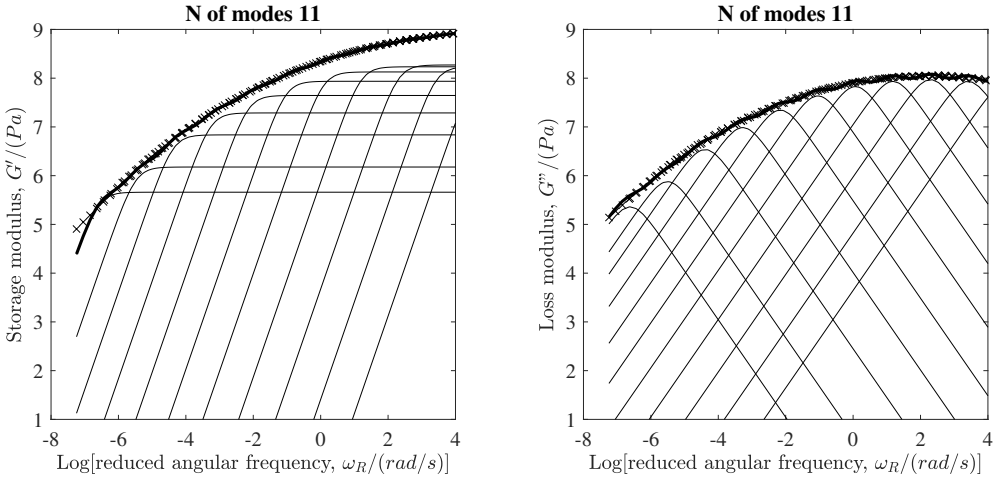

Figure 6.5 Relaxation spectrum of RTFOT binder B1 for a reference temperature T_{ref} of -15 °C

By knowing the relaxation spectrum for each material, the index I_B can be easily determined in the stress-pseudo strain domain. In order to determine the MTL critical point, as described in ch. 4, the I_B points were shifted horizontally, if necessary, to build brittleness master curves. The reference temperature T_{ref} was selected equal to -15 °C. Then, the values of I_B between 0.75 and 0.95 were interpolated linearly and the strain rate corresponding to an $I_B = 1$ was extrapolated, as shown in the example of Fig. 6.6 for binder B1.

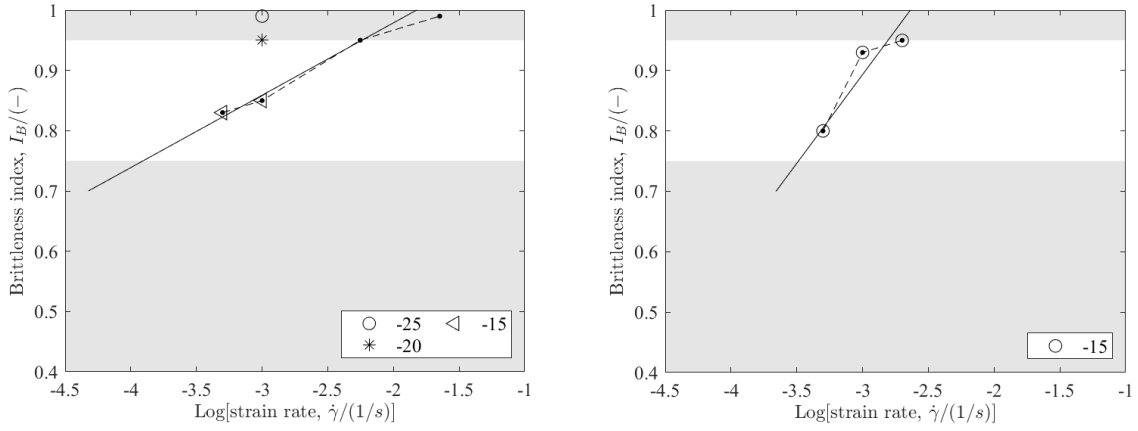

(a) RTFOT (b) PAV

Figure 6.6 Determination of the MTL critical point for binder B1 in both ageing conditions

6.5 Results and discussion

The application of the TTSP allowed to determine the critical condition, assessed as a point $(\dot{\gamma}, T)_{cr}$ using the brittleness master curves, for each strain rate and temperature following Eq. 4.6. The resulting curves are shown in Fig. 6.7. For the purpose of comparison, the temperature corresponding to the strain rate of 0.001 s^{-1} was defined as the MTL critical temperature $T_{cr,MTL}$ and inferred from Fig. 6.7, for all the materials in both ageing conditions. The so determined temperatures are reported in Fig. 6.8, in comparison with the $T_{cr,PG}$ assessed for each material as the highest critical temperature deriving from the PG grading of Table 6.4. The critical temperature assessed for the unaged materials is also shown in the bar graph of Fig. 6.8, to compare the different ageing conditions. As already explained in section 6.1 the data for binder B2 is missing.

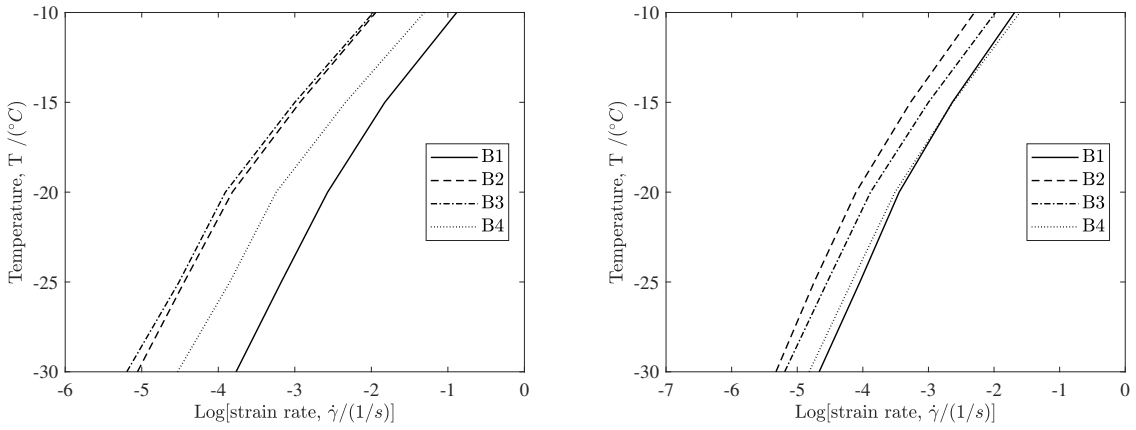

(a) RTFOT (b) PAV

Figure 6.7 Critical point as a function of temperature and strain rate

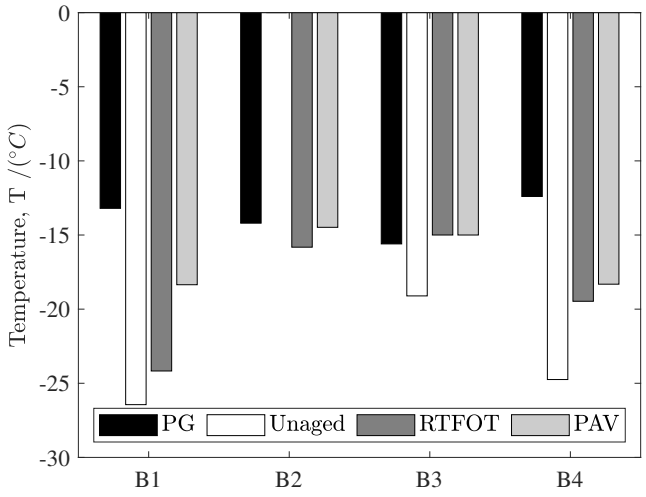

Figure 6.8 Comparison between the PG and the $T_{cr,MTL}$ assessed for RTFOT and PAV ageing conditions, for a fixed strain rate of 0.001 s^{-1}

It can observed from Fig. 6.8 that in general, for all the materials, the critical temperature increases as the ageing increases. The critical temperature for binder B1 was slightly affected by the RTFOT ageing whereas a significant increase was observed from the RTFOT to the PAV ageing condition. Conversely, the critical temperatures of binders B3 and B4 were affected more significantly from the RTFOT ageing. The highest PAV $T_{cr,MTL}$ resulted to be around $-18\,°C$ for both binders B1 and B4, which resulted to show the best performance in terms of thermal cracking in all the conditions investigated. The low temperature PG of $-22\,°C$ was not able to discriminate the different response of the materials. Considering the PG critical temperatures, it can be observed that it appeared to be similar to the MTL critical temperature for binders B2 and B3, but significantly lower for binders B1 and B4.
The results of this preliminary investigation led to think that different binders present a different response to the chemical ageing, in terms of low temperature performance. However, further investigations are needed for more precise conclusions. In particular, since the ageing affects the internal structure of binders, chemical analysis are needed to better understand the results.

Part III

Comparative analysis of results

Preamble

This part III is dedicated to the work carried out in collaboration with the "Université Gustave Eiffel" of Nantes (FR). The scope of the collaboration was to compare the MTL test procedure with the Local Fracture Test (LFT), developed in the Department of Materials and Structures of the Université Gustave Eiffel. The experimental investigation carried out involved four binders, which has been characterized for their low temperature failure response both using the MTL and the LFT test methods. The LFT allows to determine low temperature crack initiation and growth in a thin film of asphalt binder, placed between two steel hemispheric protuberances. The analysis of results involve numerical modelling, carried out using FREEFEM++. The referred chapter describes in details how the model was built, in terms of geometry and mesh, materials properties, load and boundary conditions. The LFT results are then reported and compared with that resulting from MTL approach.

Chapter 7

Experimental

7.1 Materials

The materials selected for the experimental investigation were the three binders B1, B3 and B4 (Table 3.1) and an additional fourth binder (labelled B5) supplied by the partner "Université Gustave Eiffel". The binder B5 has a PEN grade of 10/20. As a preliminary investigation, all the materials were tested unaged.
To characterize the linear viscoelastic response of binder B5, frequency sweep tests were performed, as for the other binders (see section 3.1). The tests were performed by means of the DSR, equipped with 8 mm parallel plates geometry for temperatures ranging from 34 °C to 4 °C and 4 mm parallel plates geometry for temperatures between 4 °C and −30 °C. The low temperature measurements were corrected for the compliance error, as explained in section 3.4. The experimental data are shown in the form of Black curve in Fig. 7.1a. Also for binder B5, the curve appeared to be continuous for the temperature range investigated, thus justifying the application of the TTSP. The slight discontinuity observed for phase angle values around 20° was linked to physical hardening effects arising for the change in the measurement system geometry, and do not indicate complex thermo-rheological response. The TTSP was applied and the data were shifted horizontally using the Kramers-Kronig relationship (Eq. 2.99) for a T_{ref} of −15 °C. The shift factors obtained, for each experimental temperature, are reported in Table 7.1. The master curves of the norm of the complex modulus and the phase angle are in Fig. 7.1b. Considering the cross over frequency, it appeared to reach the lowest value for binder B5, among the materials investigated, consistently with the lowest PEN. The shift factors assessed (Table 7.1) resulted to be higher for all the temperatures considered, with respect to the other binders (Table 3.2), indicating that binder B5 is the most sensitive to the variation in temperature.

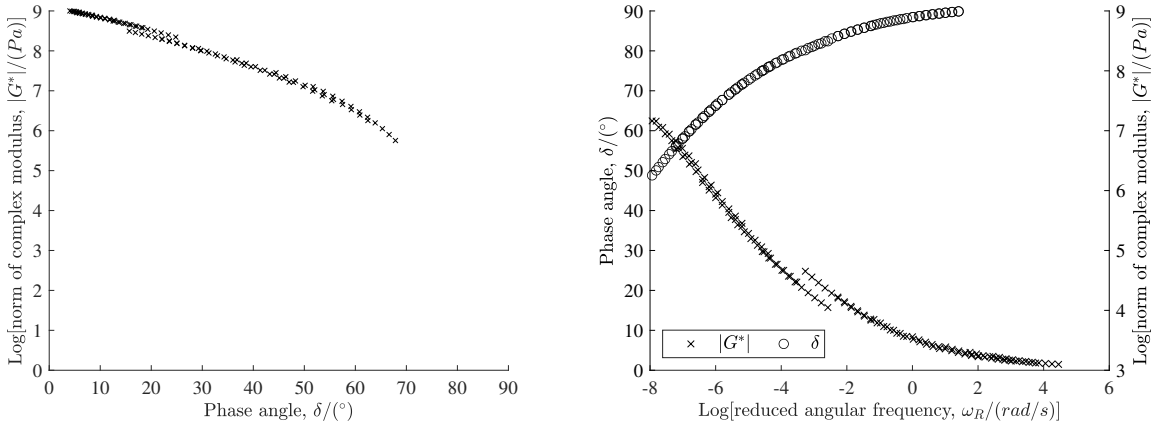

(a) Black diagram of binder B5

(b) Master curves for T_{ref} equal to -15 °C

Figure 7.1 LVE characterization of binder B5

Table 7.1 Shift factors of binder B5

Temperature ($°C$)	$log(a_T)$
-30	2.45
-25	1.75
-20	1.01
-15	0
-10	-1.17
-5	-2.28
0	-3.26
4	-4.58
10	-5.53
16	-6.40
22	-7.20
28	-7.94
34	-8.61

The T_g of binder B5 was assessed, both using the DMA and MDSC approach, following the same procedures described in section 1.3 and the results are shown in Table 7.2. Outcomes confirm the good correspondence found for the other materials between the two T_g values thus determined. It can be observed that binder B5 shows the highest T_g, considering both DMA and MDSC technique, as expected. The MDSC measurement didn't highlight the presence of any crystalline fraction for binder B5.

Table 7.2 Glass transition temperature assessed by means od DMA ($T_{g,DMA}$) and MDSC ($T_{g,MDSC}$) and wax content of binder B5

$T_{g,DMA}$(°C)	$T_{g,MDSC}$(°C)	Wax content (%)
-5	-6.5	-

7.2 Experimental plan

The experimental investigation aimed to evaluate the brittle-like response of the materials investigated, through the LFT methodology. The combinations of temperature and displacement rate were selected taking into account both material properties and experimental limits, to obtain a brittle or quasi-brittle response. The testing plan is summarized in Table 7.3. As a general framework, three displacement rates were selected (labelled d1, d2 and d3), differing from each other for the time in which the maximum elongation, fixed as 50 µm, was reached. This time was selected as 10 s, 50 s and 145 s, respectively for d1, d2 and d3. The temperatures were ranged from 0 °C to −15 °C for all the materials and the two additional higher temperatures of 5 °C and 10 °C were used for the harder binder B5.

Table 7.3 LFT experimental plan

Material	Temperatures (°C)	Displacement rate ($\mu m\,s^{-1}$)
B1	0, -5, -10, -15	d1, d2, d3
B3	0, -5, -10, -15	d1, d2, d3
B4	0, -5, -10, -15	d1, d2, d3
B5	0, -5, -10, -15	d1, d2, d3
	+5	d3
	+10	d1, d3

7.3 The Local Fracture Test

The Local fracture test (LFT) aims to evaluate crack initiation and growth of a thin film of asphalt binder, placed between two steel hemispheric protuberances, simulating two aggregates. The equipment is shown Fig. 7.2a and the test geometry in Fig. 7.2b. The two protuberances are placed inside a conditioning chamber, that allows to control the temperature. The test configuration is achieved by placing a cylindrical specimen on the lower protuberance and then lowering the upper protuberance, until the thickness in correspondence of the vertical axis of the protuberances reaches a selected value. This thickness value was fixed equal to 0.32 mm, in order to induce stress concentration in the centre of the specimen. To ensure the adhesion between the sample and the protuberances, the system is pre-heated up to temperatures close to

the binder softening point. The cylindrical specimen is prepared by means of a silicon mould and particular attention has to be paid to the presence of inhomogeneities and/or air bubbles that can affect the test results.

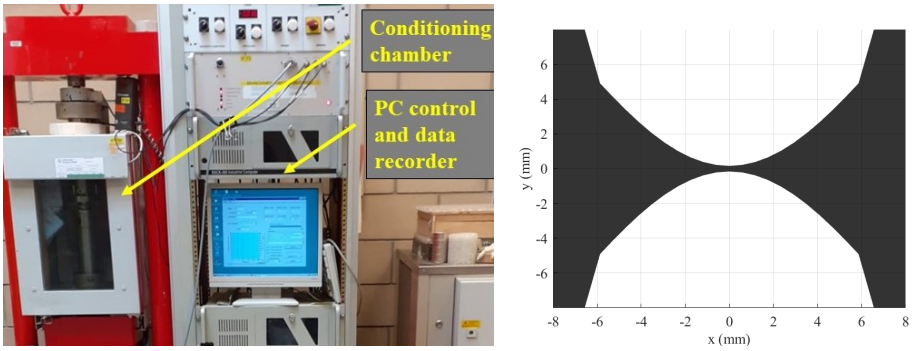

(a) Equipment (b) Test geometry

Figure 7.2 Local fracture test

The first phase of the test is the conditioning, during which the sample, placed inside the conditioning chamber, reaches the selected test temperature under controlled conditions. The whole conditioning process, including the cooling phase and the isothermal conditioning phase, is accomplished in 1 h and 45 min. When the sample reaches the test temperature, the test is started, which is composed by three subsequent phases shown in Fig. 7.3:

1. a slight compression of 20 N is applied for 20 s, that allows to give the reference geometry to the sample (Fig. 7.3a);

2. a controlled displacement is applied according to an exponential law as

$$d(t) = d_0 \left(\frac{d_f}{d_0} \right)^{t/t_f} \tag{7.1}$$

   where d_0 is the initial thickness, t is the loading time, d_f and t_f are the selected final displacement and time, respectively (Fig. 7.3b);

3. the two parts of the sample are separated at a high speed tension to visualize the fracture surface (Fig. 7.3c).

Further details about the test equipment and the procedure can be found elsewhere [16].

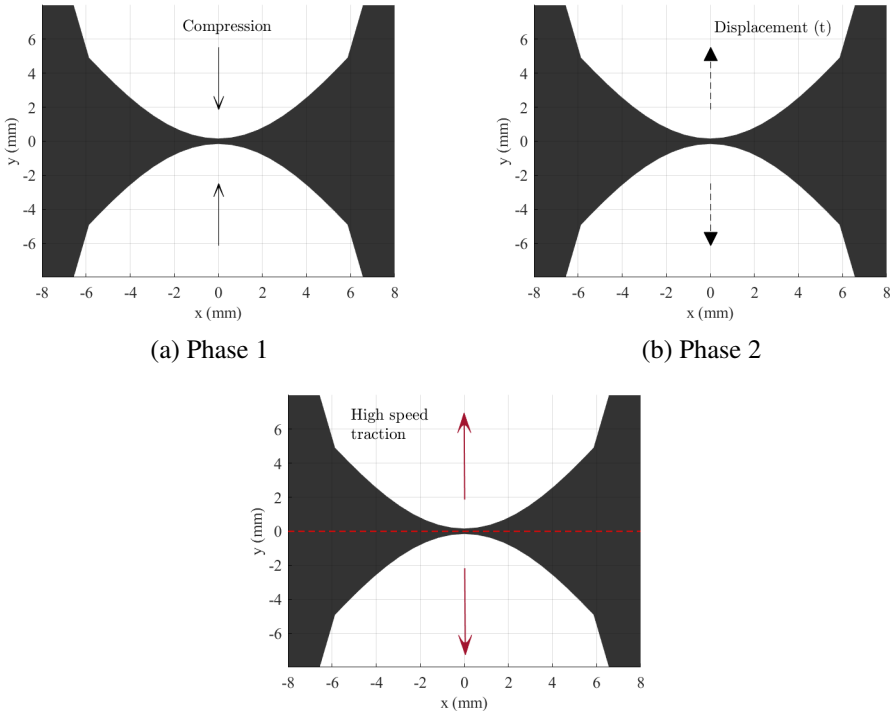

(a) Phase 1

(b) Phase 2

(c) Phase 3

Figure 7.3 Local fracture test protocol

7.3.1 Test results

The LFT test outputs are: (1) the force/displacement curve referred to elongation applied during the phase 2 of the test and (2) the crack area, visualized after the separation of phase 3. The fracture energy G can be calculated for each test as

$$G = \frac{W}{a}, \tag{7.2}$$

where W indicates the deformation energy per unit volume and a is the crack length. For the energy determination, two different situations has to be distinguished:

1. the crack propagates until the maximum diameter of the sample is reached and the material does not show a residual stiffness (Fig. 7.4);

2. the crack propagation stops before reaching the maximum diameter of the sample, which shows a residual stiffness (Fig. 7.5).

In the case (1) of complete fractured sample the energy W is simply the area under the force/displacement curve until the failure point, as shown in Fig. 7.4a. The crack length a corresponds to the sample diameter of 16 mm, as shown in Fig. 7.4b. Conversely, in the case (2) of partial fractured sample, the amount of energy referred to the residual stiffness needs to be subtracted to the total energy W calculation and then the response of the cracked specimen has to be modelled,

as shown in Fig. 7.4a. The crack length *a* is determined from the picture through image analysis. The software ImageJ [103] was used for the purpose.

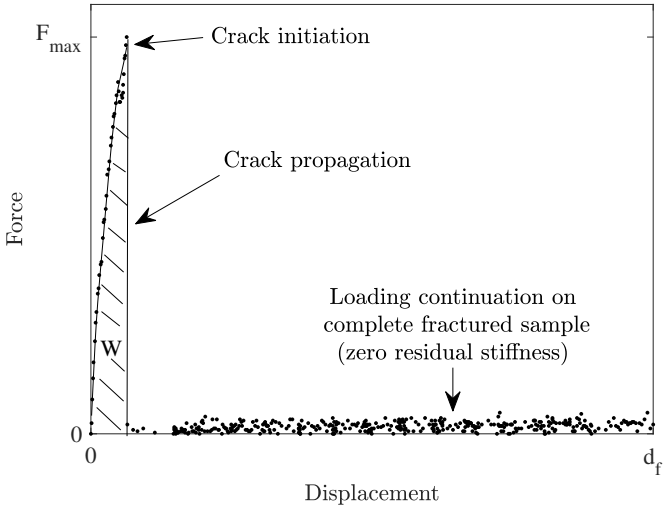

(a) Force/displacement curve

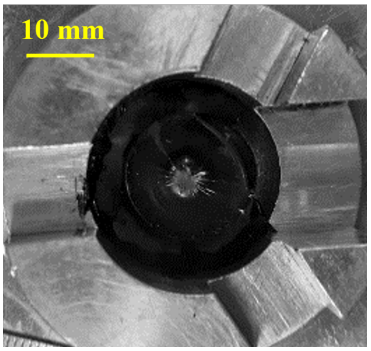

(b) Fracture morphology

Figure 7.4 Complete fractured sample

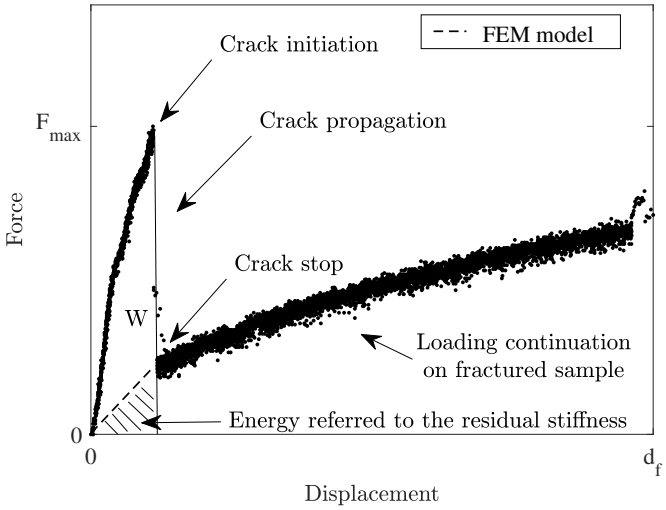

(a) Force/displacement curve

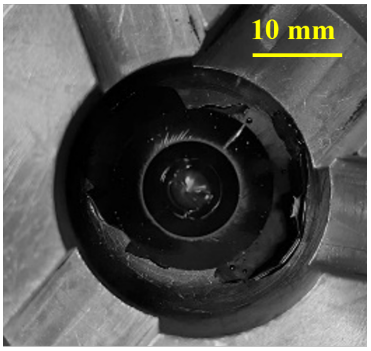

(b) Fracture morphology

Figure 7.5 Partial fractured sample

Chapter 8

Finite element modelling

The FEM model was built using the software FREEFEM++ [19], a freeware 2D and 3D partial differential equations (PDE) solver in C++ language.
The mesh adopted consists in 3332 triangular elements, with a finely discretization at the centre of the specimen to account for stress concentration, as shown in Fig. 8.1a. A second geometry was used to simulate for the cracked specimen. The crack was considered as a V-shaped crack of known dimensions d_f and a deriving from experiments, as it is represented in Fig. 8.1b.

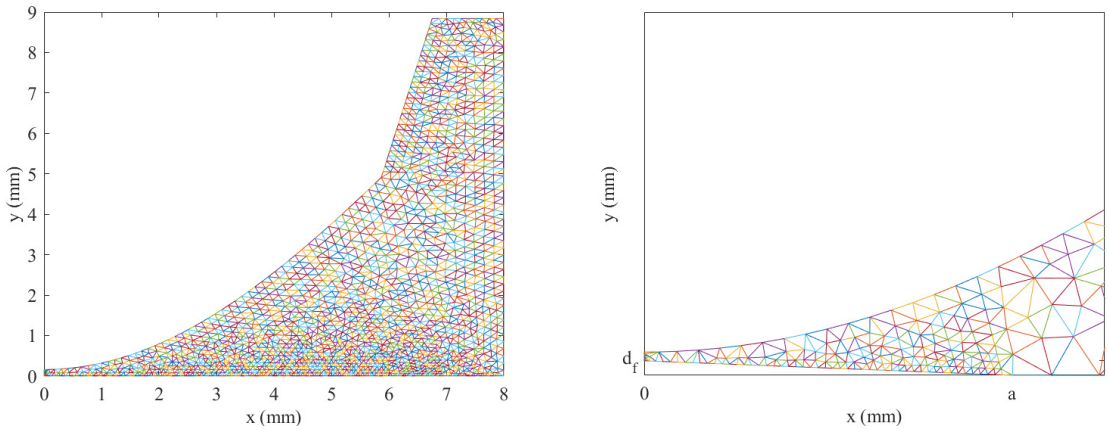

(a) Uncracked specimen

(b) V-shaped crack

Figure 8.1 Geometry and mesh

8.1 Material properties

The model requires the introduction of the material properties, which were given using the 1S2P1D model [104]. This mechanical model represents a modification of the Huet-Sayegh model [105] and is composed by a combination of 1 spring, 2 parabolic elements and 1 dashpot for rheodictic materials, as illustrated in Fig. 8.2. One spring is added in parallel, when the material is arrheodictic, leading to the more general 2S2P1D model. The creep function $J(t)$ is

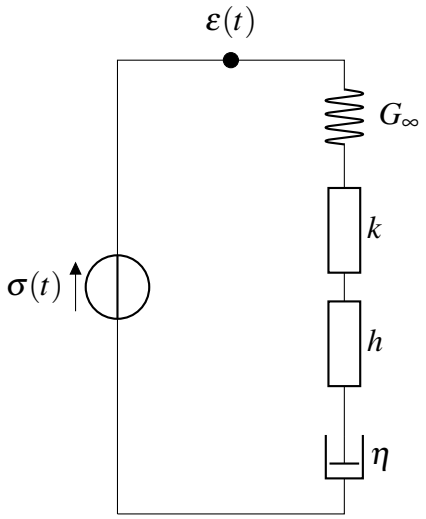

Figure 8.2 1S2P1D model

expressed through the model as

$$J(t) = \frac{1}{G_\infty}\left(1 + \delta_k \frac{(t/\tau)^k}{\Gamma(k+1)} + \delta_h \frac{(t/\tau)^h}{\Gamma(h+1)} + \frac{1}{\beta}(t/\tau)\right), \tag{8.1}$$

where G_∞, δ_k, δ_h, k, h, β and τ are the model parameters and $\Gamma(n)$ is a function defined as

$$\Gamma(n) = \int_0^\infty t^{n-1} e^{-t} dt, \tag{8.2}$$

with $n > 0$. The complex modulus G^* is expressed using the model as

$$G^*(i\omega\tau) = \frac{G_\infty}{1 + \delta_k (i\omega\tau)^{-k} + \delta_h (i\omega\tau)^{-h} + (i\omega\beta\tau)^{-1}}. \tag{8.3}$$

The model parameters were determined by fitting Eq. 8.3 on the experimental data, fixing δ_h equal to 1 to reduce the number of the parameters. The results obtained are reported in Table 8.1. Fig. 8.3 shows the experimental $|G^*|$ curves compared to curves reconstructed to the model, using the parameters assessed. A good fit was observed for all the materials investigated, except for the lower frequencies. However, this happens outside the range of the interest and therefore the parameters assessed were used to model the LVE response.

Table 8.1 2S2P1D model parameters

Material	G_∞(MPa)	δ_k	k	h	β	$\tau_{-15^\circ C}(s)$
B1	1487.9	3.08	0.21	0.49	805.5	0.53
B3	1263.4	2.25	0.23	0.54	82.8	0.86
B4	1140.9	2.29	0.17	0.44	728.2	2.19
B5	1392.3	0.81	0.13	0.34	1336.3	35.61

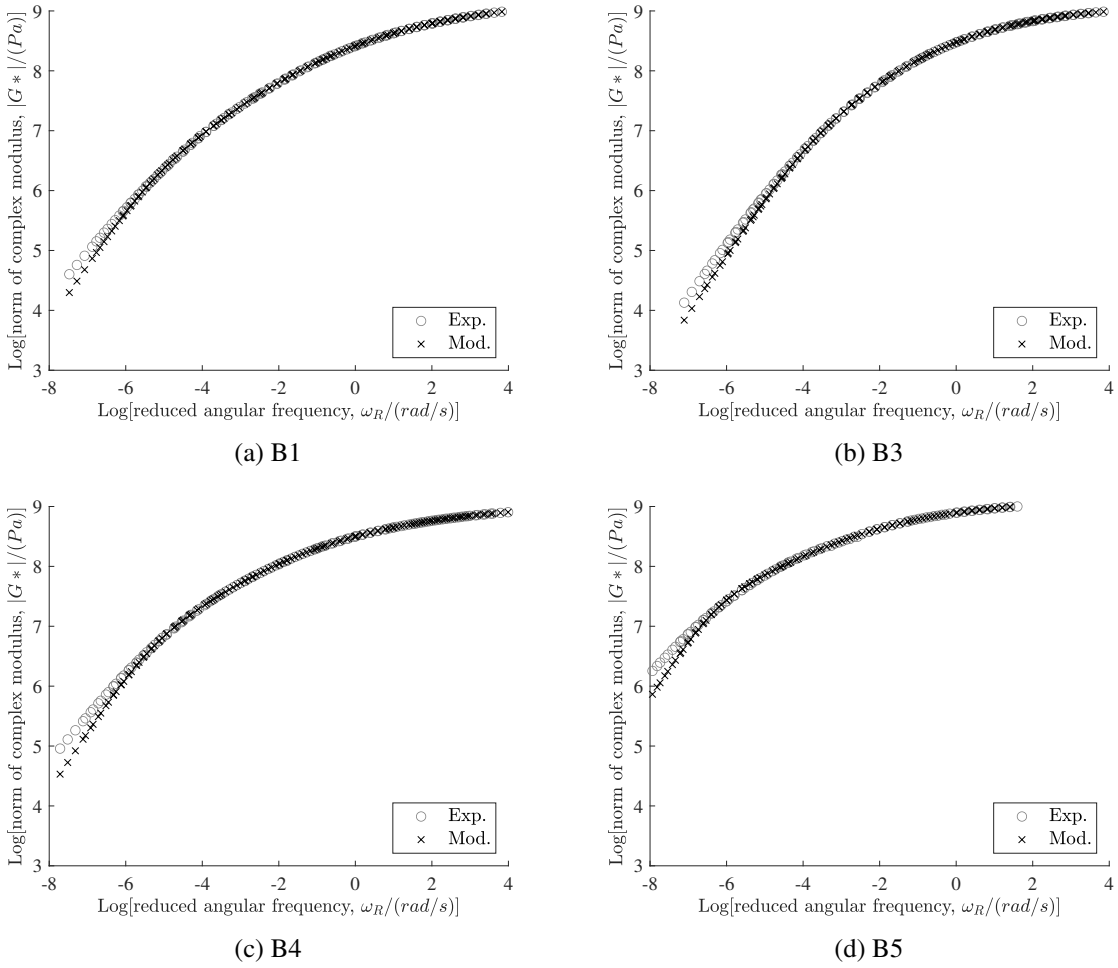

(a) B1

(b) B3

(c) B4

(d) B5

Figure 8.3 2S2P1D model compared with the experimental data coming from frequency sweep tests

The temperature dependence was described using the shift factors, previously assessed and reported in Table 3.2, for binders B1, B2 and B3, and in Table 7.1 for binder B5. A second order polynomial curve was used to describe the shift factors as a continuous function of temperature and the resulting fitting is reported in Fig. 8.4. As can be observed, the second order polynomial curve seems to successfully describe the temperature dependence of the binders investigated, for the range of temperature considered. The Poisson ratio was also necessary to build the model. Since the experimental determination of the viscoelastic Poisson ratio ν is extremely complex [106], it was calibrated iteratively, as shown in Fig. 8.5, to let the model to superimpose the experimental curves. For the calibration, the coefficient was assumed to be dependent only on the temperature, therefore neglecting the dependence on the loading time. This assumption was considered valid due to the small range of loading times investigated. However, it has to be underlined that the assessed coefficients do not represent the "real" material Poisson ratio, but an estimate, which can include different unknown factors.

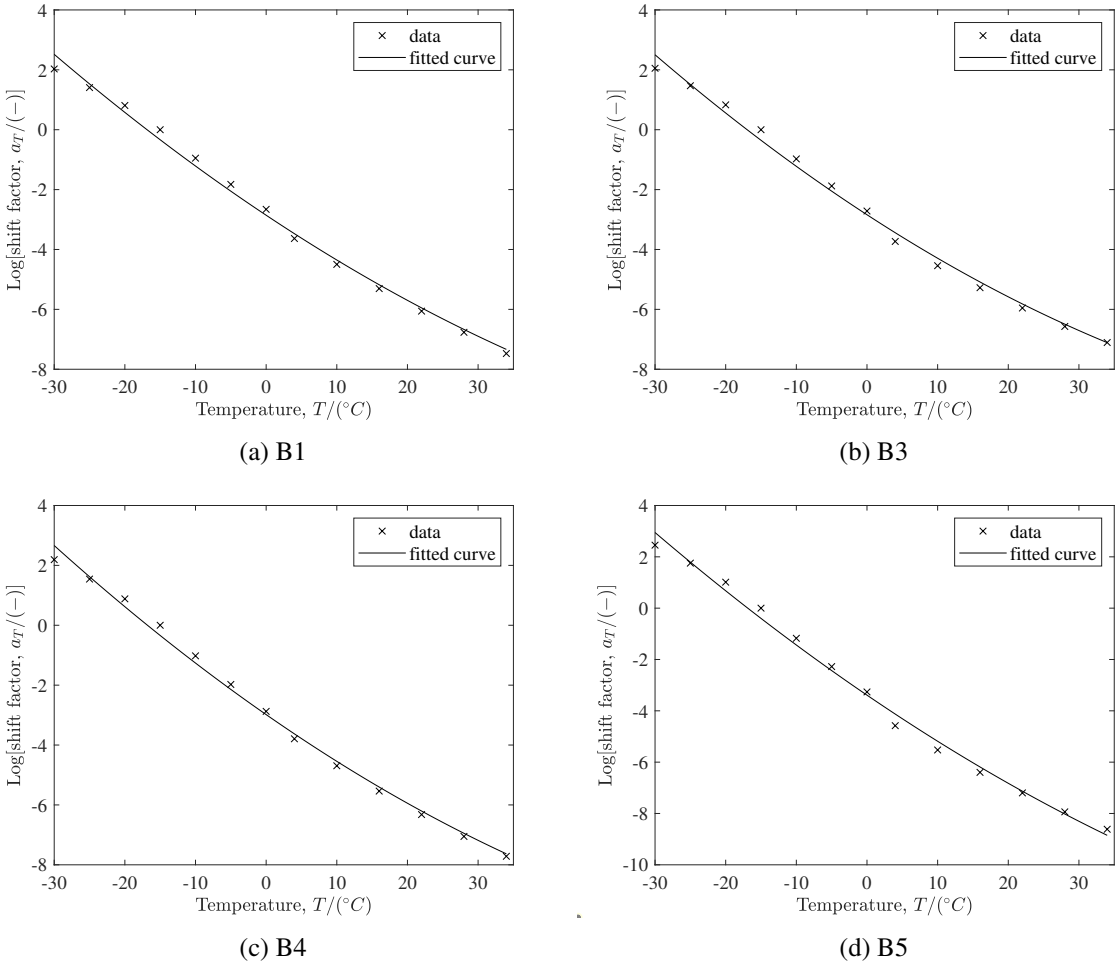

(a) B1 (b) B3

(c) B4 (d) B5

Figure 8.4 Shift factors fit using a second order polynomial curve

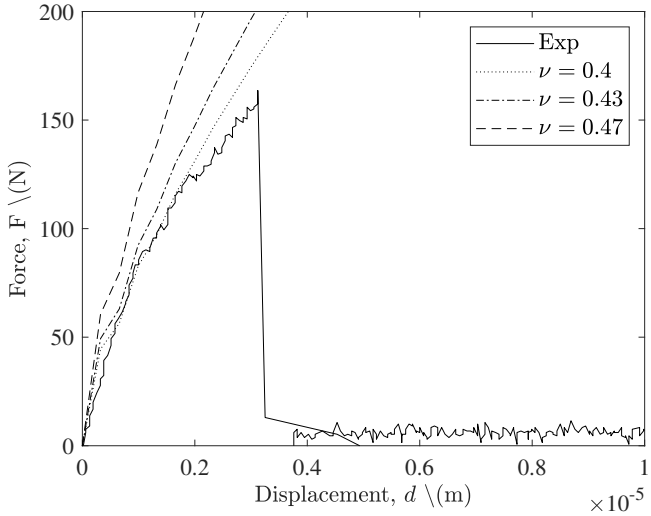

Figure 8.5 Calibration of the Poisson ratio ν

8.2 Problem formulation

The isothermal viscoelastic constitutive equations in three dimensions is written as

$$\boldsymbol{\varepsilon}(t) = \int_0^t J(t-\xi)\,[(1+\nu)\dot{\boldsymbol{\sigma}}(\xi) - \nu\, tr(\dot{\boldsymbol{\sigma}}(\xi))\boldsymbol{I}]\,d\xi \tag{8.4}$$

where J is the compliance function, ν is the Poisson coefficient, $\boldsymbol{\sigma}$ and $\boldsymbol{\varepsilon}$ are the stress and the strain tensor respectively and $\boldsymbol{I}$ is the second order identity tensor.
Discretizing the time interval $[0,t]$ such that $t_0 = 0$, $t_1 = \Delta t$, ..., $t_i = t_{i-1} + \Delta t$, ..., $t_n = t_{n-1} + \Delta t$, Eq. 8.4 becomes

$$\boldsymbol{\varepsilon}(t) = \sum_{i=1}^{n} \int_{t_{i-1}}^{t_i} J(t-\xi)\,[(1+\nu)\dot{\boldsymbol{\sigma}}(\xi) - \nu\, tr(\dot{\boldsymbol{\sigma}}(\xi))\boldsymbol{I}]\,d\xi. \tag{8.5}$$

The time derivative of the stress tensor can be approximated, if the stress is a continuous function of time, as

$$\dot{\boldsymbol{\sigma}} \approx \frac{\boldsymbol{\sigma}(t_i) - \boldsymbol{\sigma}(t_{i-1})}{\Delta t_i} = \frac{\boldsymbol{\sigma}_i - \boldsymbol{\sigma}_{i-1}}{\Delta t_i}. \tag{8.6}$$

Substituting Eq. 8.6 into Eq. 8.5 the relation becomes

$$\boldsymbol{\varepsilon}(t) = \sum_{i=1}^{n} \int_{t_{i-1}}^{t_i} J(t-\xi) \left[\frac{(1+\nu)(\boldsymbol{\sigma}_i - \boldsymbol{\sigma}_{i-1}) - \nu\, tr(\boldsymbol{\sigma}_i - \boldsymbol{\sigma}_{i-1})\boldsymbol{I}}{\Delta t_i} \right] d\xi. \tag{8.7}$$

The integral of Eq. 8.7 can be discretized using the trapezoidal rule as

$$\boldsymbol{\varepsilon}(t) \approx \sum_{i=1}^{n} \frac{J(t-t_i) + J(t-t_{i-1})}{2} \Delta t_i \left[\frac{(1+\nu)(\boldsymbol{\sigma}_i - \boldsymbol{\sigma}_{i-1}) - \nu\, tr(\boldsymbol{\sigma}_i - \boldsymbol{\sigma}_{i-1})\boldsymbol{I}}{\Delta t_i} \Delta t_i \right] \tag{8.8}$$

or equivalently

$$\boldsymbol{\varepsilon}(t) \approx \sum_{i=1}^{n} \bar{J}_i \left[\frac{(1+\nu)(\boldsymbol{\sigma}_i - \boldsymbol{\sigma}_{i-1}) - \nu\, tr(\boldsymbol{\sigma}_i - \boldsymbol{\sigma}_{i-1})\boldsymbol{I}}{\Delta t_i} \Delta t_i \right]. \tag{8.9}$$

The expression of Eq. 8.9 can be simplified for the numerical problem by introducing the tensor $\bar{\boldsymbol{\chi}}$ defined as

$$\begin{aligned} \bar{\boldsymbol{\chi}}_n =& \bar{J}_n\,[(1+\nu)\boldsymbol{\sigma}_{n-1} - \nu\, tr(\boldsymbol{\sigma}_{n-i}\boldsymbol{I})] + \\ & - \sum_{i=1}^{n-1} \bar{J}_i\,[(1+\nu)\boldsymbol{\sigma}_i - \nu\, tr(\boldsymbol{\sigma}_i\boldsymbol{I})] - [(1+\nu)\boldsymbol{\sigma}_{i-1} - \nu\, tr(\boldsymbol{\sigma}_{i-i}\boldsymbol{I})]\,. \end{aligned} \tag{8.10}$$

Eq. 8.9 can be rewritten considering Eq. 8.10 as

$$\boldsymbol{\varepsilon}(t) = \bar{J}_n\,[(1+\nu)(\boldsymbol{\sigma}(t) - \nu\, tr(\boldsymbol{\sigma}(t)))\boldsymbol{I}] - \bar{\boldsymbol{\chi}}_n. \tag{8.11}$$

Inverting the Eq. 8.11 the following expression can be obtained

$$\boldsymbol{\sigma}(t) = \frac{1}{(1+\nu)\bar{J}_n}\left[\boldsymbol{\varepsilon}(t) + \bar{\boldsymbol{\chi}}_n\right] + \frac{\nu}{(1+\nu)(1-2\nu)\bar{J}_n}\left[tr(\boldsymbol{\varepsilon}(t)) + tr(\bar{\boldsymbol{\chi}}_{\boldsymbol{n}})\boldsymbol{I}\right], \tag{8.12}$$

or equivalently

$$\boldsymbol{\sigma}(t) = 2\bar{\mu}\boldsymbol{\varepsilon}(t) + \bar{\lambda}_n tr(\boldsymbol{\varepsilon}(t))\boldsymbol{I} + 2\bar{\mu}_n\bar{\boldsymbol{\chi}}_n + \bar{\lambda}_n tr(\bar{\boldsymbol{\chi}}_{\boldsymbol{n}})\boldsymbol{I} \tag{8.13}$$

where

$$\bar{\mu}_n = \frac{1}{(1+\nu)\bar{J}_n} \tag{8.14}$$

and

$$\bar{\lambda}_n = \frac{\nu}{(1+\nu)(1-2\nu)\bar{J}_n}. \tag{8.15}$$

Consider a viscoelastic body with undeformed shape Ω, the principle of virtual work allows to find the displacement vector $\boldsymbol{u}$ such that the following expression is verified

$$\int_\Omega \boldsymbol{\sigma}(\boldsymbol{u}) : \boldsymbol{\varepsilon}(\boldsymbol{v})d\Omega = \int_\Omega \boldsymbol{f}\,\boldsymbol{v}d\Omega + \int_{\partial\Omega} \boldsymbol{\sigma}(\boldsymbol{u})\,\boldsymbol{n}\,\boldsymbol{v}d\Gamma \tag{8.16}$$

where $\boldsymbol{v}$ is the vector of virtual displacement and Γ are the boundaries of the body Ω. The problem can be written in its variational form by substituting Eq. 8.13 into the formulation of Eq. 8.16

$$\begin{aligned}&\int_\Omega \left[2\bar{\mu}_n\boldsymbol{\varepsilon}(t) + \bar{\lambda}_n tr(\boldsymbol{\varepsilon}(t))\boldsymbol{I} + \bar{\mu}_n\bar{\boldsymbol{\chi}}_n + \bar{\lambda}_n tr(\bar{\boldsymbol{\chi}}_n)\boldsymbol{I}\right] : \boldsymbol{\varepsilon}(\boldsymbol{v})d\Omega = \\ &= \int_\Omega \boldsymbol{f}\,\boldsymbol{v}d\Omega + \int_{\partial\Omega} \boldsymbol{\sigma}(\boldsymbol{u})\,\boldsymbol{n}\,\boldsymbol{v}d\Gamma.\end{aligned} \tag{8.17}$$

8.3 Solution

Fig. 8.6 shows some examples of the modelled curves, compared with that coming from the experiments. As can be observed, the model represented in a successful way the response, both for uncracked and cracked specimen. Observing Figs. 8.6b and 8.6d, it can be noticed that, for some combinations of temperature and strain rate, the model starts to diverge from the experimental curve, for a certain level of elongation. This result was addressed to the occurrence of a non linear response, due to non linear viscoelasticity and/or damage.

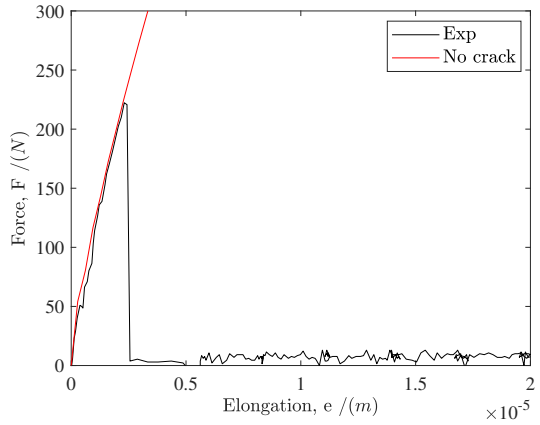

(a) Complete fractured sample: example 1

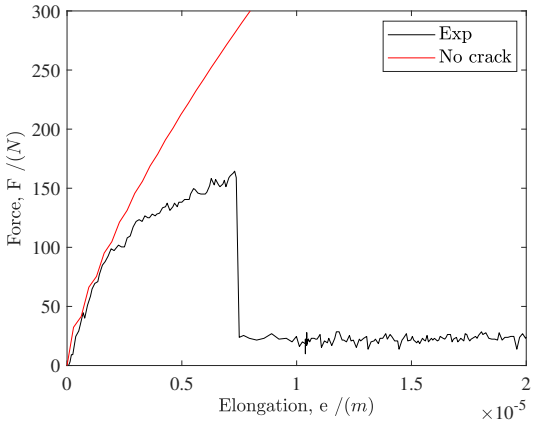

(b) Complete fractured sample: example 2

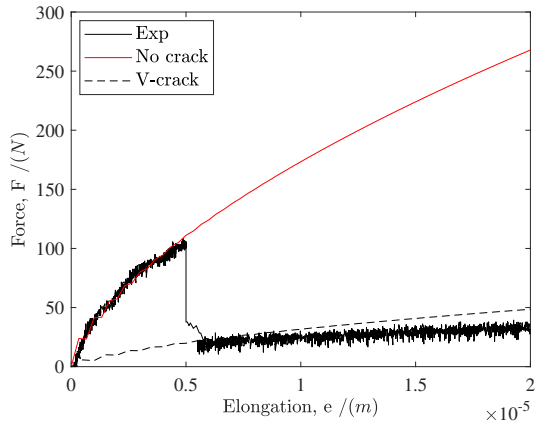

(c) Partial fractured sample: example 1

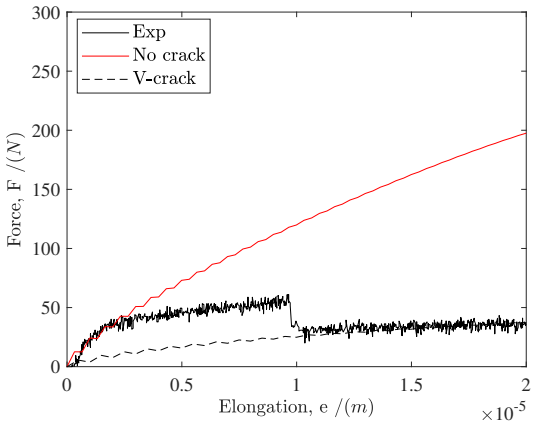

(d) Partial fractured sample: example 2

Figure 8.6 Example of FEM model results in terms of force/displacement curves, compared to the corresponding experimental curves

Chapter 9

Results and discussion

9.1 Methodology of interpretation

The fracture energy G was using Eq. 7.2, combined with the FEM model for the partial cracked samples, and the results obtained are shown in Fig. 9.1, as a function of temperature and loading rate. For all the materials investigated, it can be observed that G is temperature- and/or time-dependent. In particular it decreases as the temperature decreases or the loading rate increases. The rate of the energy reduction tends to diminish as the combination of temperature and time leads the material to reach an elastic-like response, corresponding to the minimum value of G. In this condition, the energy starts to be independent upon temperature and/or loading rate, since the viscoelastic component of the response becomes negligible. The results of Fig. 9.1 suggested the validity of the TTSP for the energy G. Therefore, by applying the same approach used for the brittleness index in section 4.2, the energy G was shifted along the logarithmic time axis by means of the shift factors coming from the LVE characterization (Table 3.2 and 7.1). The shifting procedure was referred to the strain rate, such that

$$log(\dot{\varepsilon}_r) = log(\dot{\varepsilon}) + log(a_T) \tag{9.1}$$

where a_T is the shift factor. The strain rate was assessed for each test, according to Eq. 7.1, as

$$\dot{\varepsilon} = \frac{1}{t_f} \ln(\frac{d_f}{d_0}) \tag{9.2}$$

where t_f and d_f are the selected final time and elongation of phase 2 and d_0 is the initial elongation. Since the specimen geometry is not regular, the elongation d_0 was assumed to be equal to the average value between the maximum and the minimum height of the specimen. The maximum height is reached at the external edges and is equal to 9 mm, whereas the minimum thickness appears at the centre and is equal to 0.32 mm. The master curves for the energy G were built, selecting -15 °C as the reference temperature T_{ref}, and are reported in Fig. 9.2. The master curves showed a continuous trend for all the materials tested, validating the use of the TTSP, which remains empirical [87]. The energy decreases as the strain rate increases, when the

temperature is constant and the trend of this energy reduction appeared to be similar for all the binders tested, except for the softer binder B3. In fact, binder B3 changed from a brittle response to fail for flow in a very narrow range of times, as can be observed from Fig. 9.2.

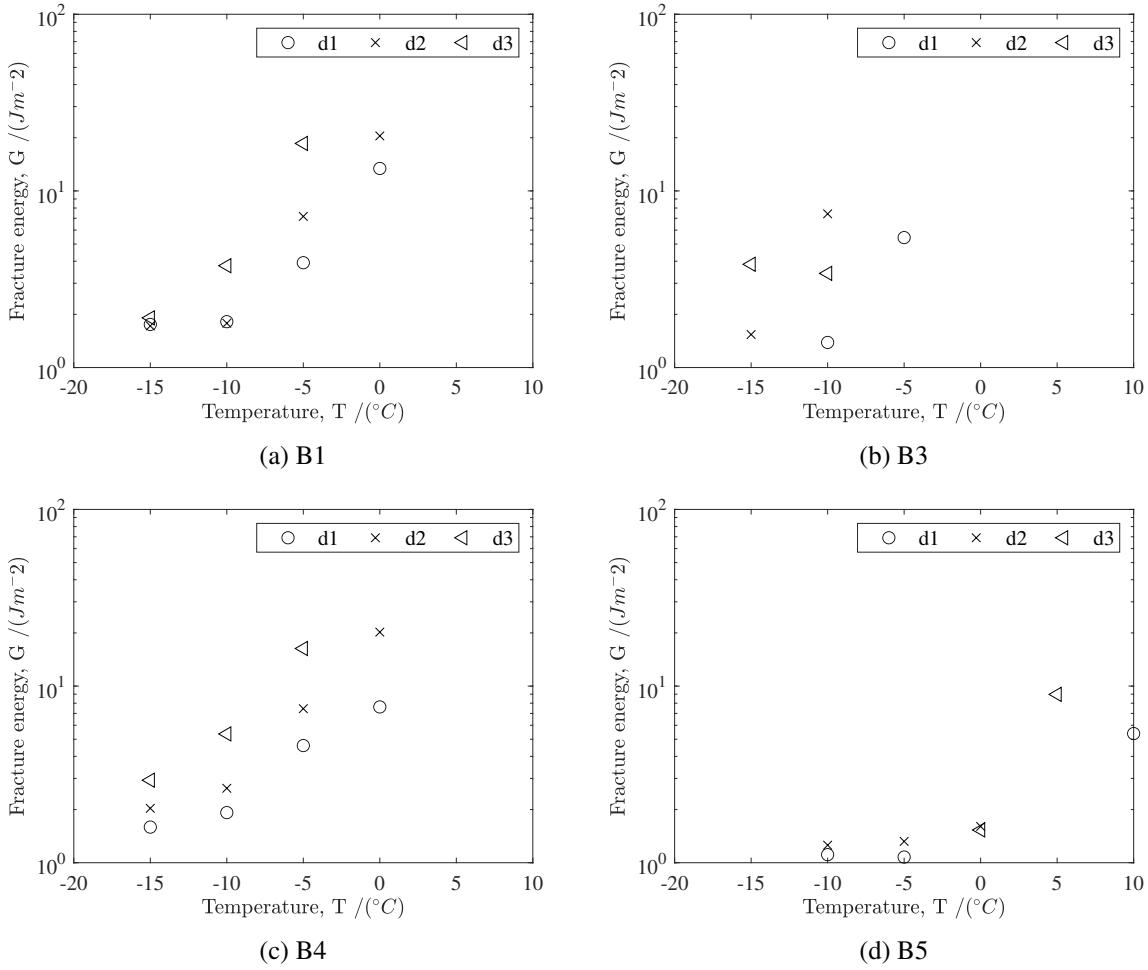

(a) B1

(b) B3

(c) B4

(d) B5

Figure 9.1 Fracture energy assessed as a function of temperature and loading rate

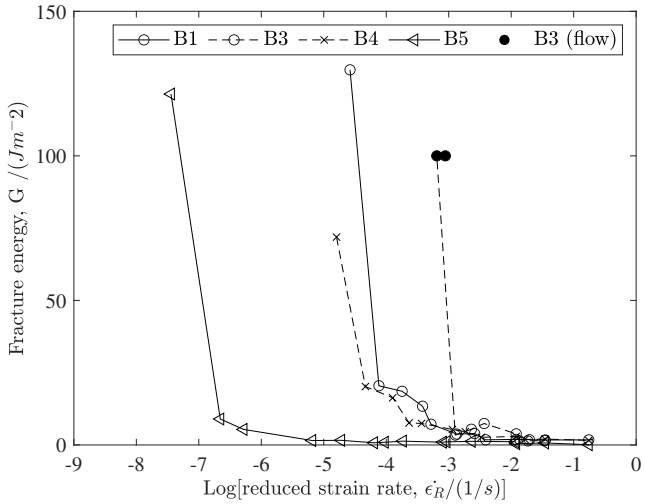

Figure 9.2 Fracture energy master curves for a T_{ref} of -15 °C

Three regions of response were identified based on the master curves of Fig. 9.2:

1. the ductile region;
2. the quasi-brittle region;
3. the brittle region.

The brittle region was easily detected from the master curves since the energy reaches its minimum value and starts to be time-independent. The ductile region was defined for energy values greater than $50\,\mathrm{J\,m^{-2}}$ and the quasi-brittle region as the transition between the other two regions. The starting point of the brittle region was considered as the LFT critical point and it was assessed as the interception point between the line fitted considering the experimental points of region 1 and that fitted on the experimental points of region 2. The procedure is shown in Fig. 9.3. For binder B3 were not detected, as mentioned, any points belonging to region 2 since it resulted to be so small that was complex to be investigated experimentally. Therefore in this case, the averaged time between the first point of the brittle response and the last point of the ductile response was defined as the starting point of the brittle region. The determination of these critical points, for all the materials considered, allows to build a curve, in the two variables time and temperature, representing the LFT critical conditions, using the LVE shift factors. The curves are shown in Fig. 9.4. The figure shows that binder B5 was the most prone to crack for low temperatures, over the complete range of strain rates and temperatures investigated, as expected, and a significant difference was observed compared to the other materials. Binder B1 resulted to have the best performance in terms of low temperature cracking, closed to that of binder B4, the SBS-modified.

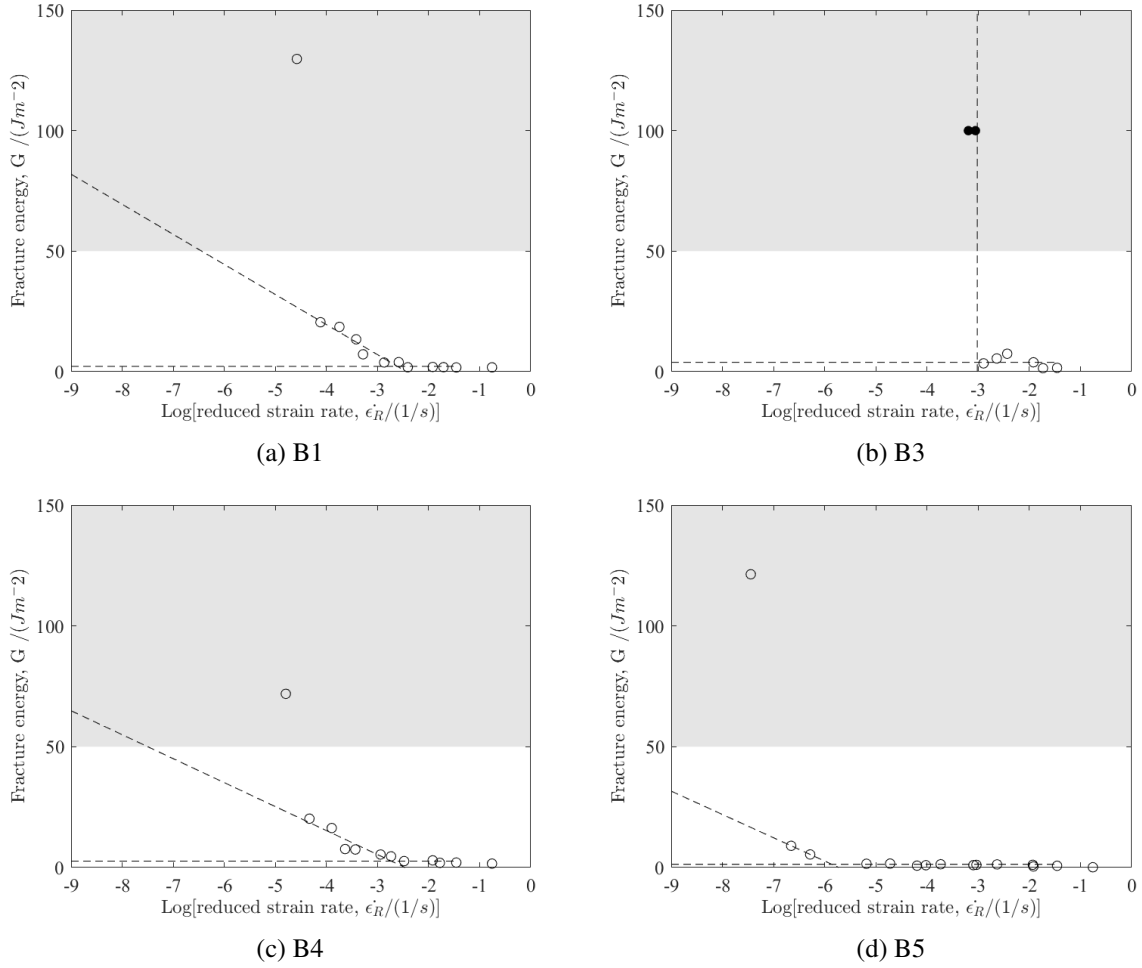

(a) B1 (b) B3

(c) B4 (d) B5

Figure 9.3 Determination of the critical strain rate for the reference temperature T_{ref} equal to -15 °C

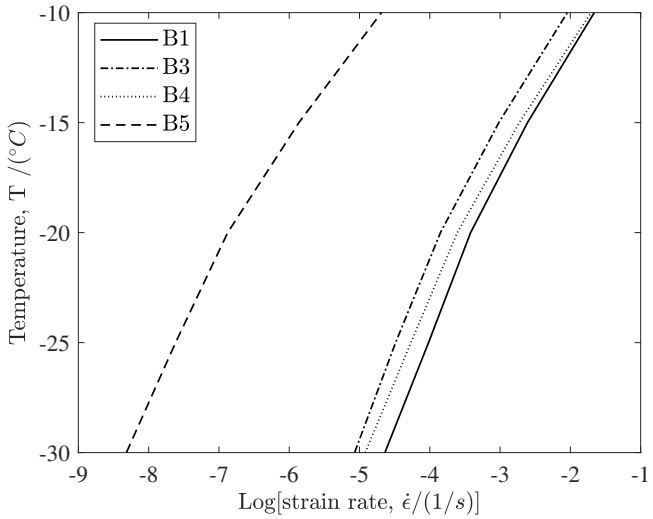

Figure 9.4 Critical LFT point as a function of temperature and strain rate

9.2 Comparison with the MTL test results

The results obtained were compared to that coming from the MTL approach. For the purpose, the MTL critical point was assessed for binder B5. The MTL tests were performed fixing the test temperatures as $-10\,°C$ and $-5\,°C$. Two rates of loading were tested for each temperature: 0.001 % and 0.0005 %. The brittleness index I_B was assesses for each test, as indicated in Eq. 4.4. The relaxation spectrum, needed for the I_B determination was inferred from the frequency sweep test data, using the algorithm described in section 4.1. The results are detailed in appendix A. The I_B values were shifted along the loading time axis, using the shift factors of Table 7.1 to build the brittleness master curve, for a reference temperature of $-15\,°C$. The critical point was assessed using the master curve as the interception point between the line interpolating the points referred to the quasi-brittle region and the value of I_B equal to one. The curve and the assessed critical point are shown in Fig. 9.5.

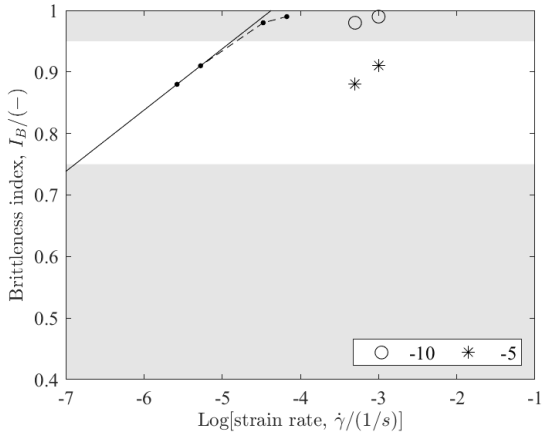

Figure 9.5 Determination of the MTL critical point for binder B5

The comparison between the critical conditions assessed using the LFT and that coming from the proposed MTL approach are shown in Fig. 9.6, for all the materials investigated, as a function of temperature and strain rate. The symbol $\dot{\gamma}$ is used to address the strain rate in Fig. 9.6, for graphical simplicity, although the symbol $\dot{\varepsilon}$ is more appropriate for LFT results, since it is a tensile test. It can be observed from Fig. 9.6 that the two different approaches led to rank in the same way the materials for thermal cracking performance. In fact, binder B1 showed, for both the methodologies, the lowest critical temperature over the entire range of loading rate, followed by the SBS modified binder B4. The soft binder B3 showed an intermediate critical temperature and the hard binder B5 appeared to be the most fragile, with a significant highest critical temperature regardless the loading rate selected. Although the two tests led to the same materials ranking, the LFT critical condition resulted always for higher temperatures than that coming from MTL. In other words, the response appeared to be more brittle when the material was tested by means of the LFT.
The temperatures corresponding to a fixed strain rate of 0.001 s^{-1} were selected for the purpose of comparison and the results are shown in Fig. 9.7. The LFT critical temperature resulted to be always higher than that coming from the MTL approach as already observed. However, a

linear correlation was found between the two temperatures, as can be observed from Fig. 9.7b, indicating the two methodologies led to the same materials ranking.
Referring to Table 1.1, the more brittle response the material shows when tested with the LFT can be explained considering:

1. geometry and size, since the volume of the LFT sample is greater than that of the MTL cylinder;

2. type of loading, since the LFT is a tensile test and the MTL is a torsion test.

Furthermore, the LFT conditioning phase presents a higher cooling rate and storage time that could lead the material to age for physical hardening. Further investigation would needed to evaluate the effect of the conditioning phase on the results.

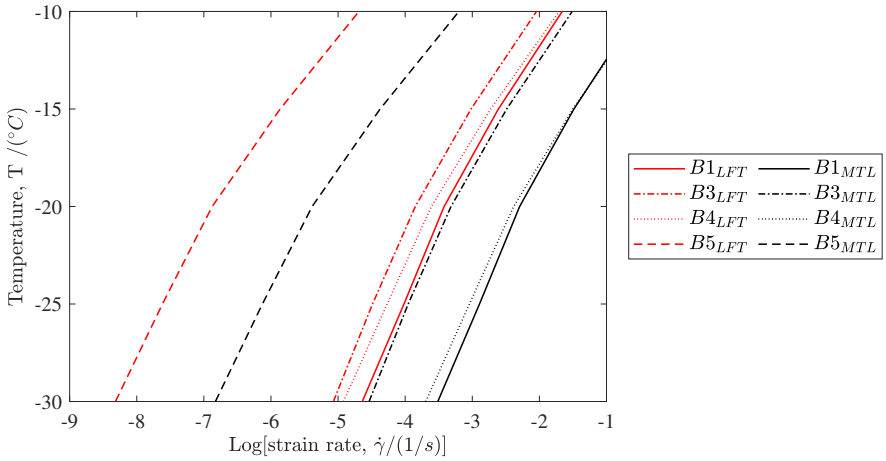

Figure 9.6 Comparison between the LFT and the MTL critical curves

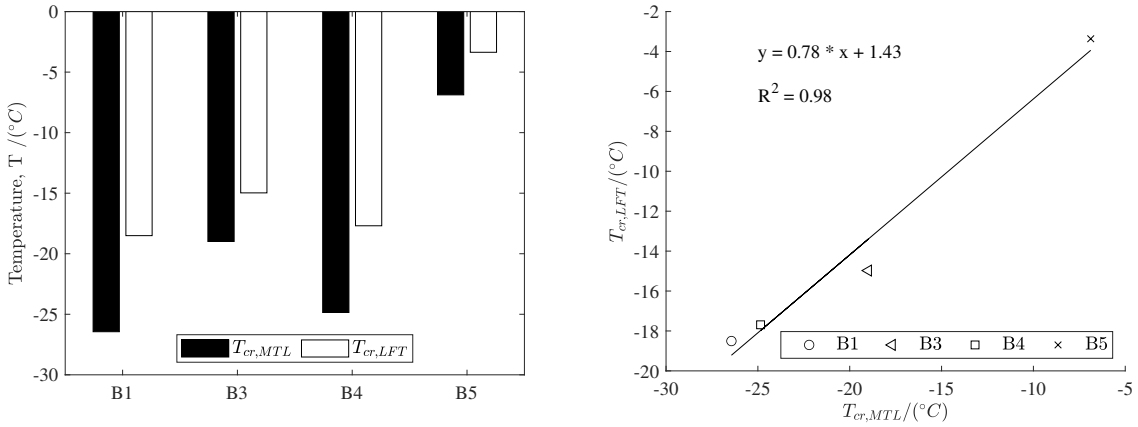

(a) Bar graph

(b) Linear correlation

Figure 9.7 Comparison between the critical temperature coming from the MTL and the LFT test, for a strain rate of 0.001 s^{-1}

Conclusions

The thesis aims to develop and propose a novel methodology to characterize low temperature failure properties of asphalt binders. The experimental investigation carried out involved a set of four unaged binders, three unmodified and one modified with SBS, which were preliminary characterized in their linear viscoelastic response. The MTL test proposed, involves to subject a cylindrical specimen to a monotonic torsional load until failure, by means of a fixed constant strain rate. The extended use of the DSR for failure tests would allow to completely characterize the binders by adopting the same experimental equipment. Several tests were performed for each material, considering different combinations of temperature and strain rate and the corresponding failure points were easily detected from the stress/strain curves. For each test, a synthetic index, termed as brittleness index was determined, considering the stress/pseudo strain domain, as the ratio between the pseudo strain energy density and the linear viscoelastic pseudo strain energy density. The brittleness index reaches its maximum value of 1 when the response is purely brittle, that means that the material is not able to dissipate more energy than that referred to the linear viscoelasticity. By applying the TTSP, brittleness master curves were built for a selected reference temperature. The master curves allowed the determination, for each material, of a critical point in terms of temperature and strain rate which refers to its critical condition of brittle response. Therefore, by fixing the strain rate, a critical temperature can be determined. Outcomes showed that the proposed approach can be an effective tool in evaluating and discriminating the low temperature failure properties of asphalt binders. Lastly, the MTL critical temperature was compared to that determined using the LFT methodology through a collaboration with the "université Gustave Eiffel" of Nantes. The two approaches resulted to be in good agreement concerning the materials ranking in terms of thermal cracking performance.
Specific conclusions of the study are here summarized.

- The failure stress increases as the temperature decreases (and/or the strain rate increases). Conversely, the failure strain decreases, as the temperature decreases (and/or the strain rate increases). Therefore, the binder strength increases, as well as its brittleness since the material becomes 'harder' and less capable to dissipate energy before rupture.

- The stress/pseudo strain curves show that the response, for some combinations of temperature and strain rate, deviates from the linearity for a certain level of deformation. This indicates that the material shows a further dissipation of energy, in addition to that linked to the linear viscoelasticity.

- The critical cracking temperature and the glass transition temperature were found to be in good agreement with each other in the case of unmodified asphalt binders. Conversely, for the considered modified binder, the glass transition temperature was significantly higher, thus suggesting that the MTL critical temperature captures more effectively the peculiar role played by polymer networks in improving the potential resistance to thermal cracking of binders.

- The proposed experimental protocol repeatability resulted to be consistent with other failure test methods for brittle materials, with a COV coefficient of 9.1 % for the failure stress and 13.1 % for the strain.

- The MTL and LFT approaches resulted to be in good agreement to rank the materials in terms of thermal cracking. However, the LFT critical temperature appeared to be always higher than that coming from the MTL. Several explanation may be found, as the different type of loading, conditioning or geometry.

The thesis proposes a promising methodology to characterize failure properties of binders at low temperature and further studies are certainly needed to improve the procedure. Some final remarks are here indicated.
The experimental procedure described is the result of several attempts which addressed mainly the specimen geometry, the conditioning phase and the testing parameters. However, further experimental work is certainly needed to evaluate and improve the experimental protocol, focusing on reducing the coefficient of variation of the results. The procedure validation requires an extended material database, including in particular newly modified binders. Lastly, the assessed thermal cracking response of binders needs to be correlated with the mixture performance, and then with the pavement response in the field.

List of Figures

List of Tables

List of Symbols

The following list reports only the symbols repeatadly used for the thesis discussion, and does not include those that are just mentioned. To avoid duplications, a viscoelastic material function is listed as the time-dependent response $F(t)$. The corresponding harmonic responses $F^*(\omega)$, $F'(\omega)$ and $F''(\omega)$ are not reported.

Roman Symbols

a_T	temperature shift factor
$D(t)$	stretch creep compliance
$E(t)$	stretch relaxation modulus
$G(t)$	shear relaxation modulus
I_B	brittleness index
$J(t)$	shear creep compliance
J_t	DSR machine compliance
$S(t)$	BBR stiffness
T_g	glass transition temperature
T_{ref}	reference temperature
w^R	pseudo strain energy density
w^R_{LVE}	LVE pseudo strain energy density
d	diameter
f	frequency
g	relaxation strength
H(t)	Heaviside unit step function
I	input

R response

r radius

W strain energy density

Greek Symbols

δ phase angle

δ_{ij} Kronecker's delta

$\dot{\gamma}$ shear strain rate

γ shear strain

γ^R pseudo strain

γ_F failure shear strian

ν Poisson ratio

ω angular frequency

ρ relaxation time

τ shear stress

τ_F failure shear stress

Superscripts

R pseudo quantity

' real part of a complex function

" imaginary part of a complex function

* complex function

Acronyms / Abbreviations

BBR bending beam rheometer

COV coefficient of variation

DMA dynamic mechanical analysis

DSC differential scanning calorimetry

DSR dynamic shear rheometer

DTT direct tension tester

E-VC elastic-viscoelastic correspondence principle

FEM finite element method

HI hardening index

HR hardening rate

LEFM linear elastic fracture mechanics

LFT local fracture test

LVE linear viscoelastic

MDSC modulated differential scanning calorimetry

MTL monotonic torsional loading test

NLVE non-linear viscoelastic

PAV pressurized ageing vessel

PDE partial differential equation

PEN penetration grade

PG performance-grade

PP04 4-mm parallel plates

RTFOT rolling thin film oven test

TMA thermo-mechanical analysis

TTSP time-temperature superposition principle

References

1. Bouldin, M. G., Dongré, R., Rowe, G. M., Sharrock, M. J. & Anderson, D. A. Predicting thermal cracking of pavements from binder properties: theoretical basis and field validation. *J. Assoc. Asph. Paving Technol.* **69,** 455–496 (2000).
2. Iliuta, S., Hesp, S. A. M., Marasteanu, M. O., Masliwec, T. & Tam, K. K. Field Validation Study of Low-Temperature Performance Grading Tests for Asphalt Binders. *J. Assoc. Asph. Paving Technol.* **1875,** 14–21 (2004).
3. Vinson, T. S., Janoo, V. C. & Haas, R. C. *Low Temperature and Thermal Fatigue Cracking, SHRP Summary Report No. A-003A* tech. rep. (1989).
4. Isacsson, U. & Zeng, H. Relationships between bitumen chemistry and low temperature behaviour of asphalt. *Constr. Build. Mater.* **11,** 83–91 (1997).
5. AASHTO M320-17. Standard Specification for Performance-Graded Asphalt Binder. *Stand. Specif. Transp. Mater. Methods Sampl. Test.* (2017).
6. European Committee for Standardization. Bitumen and bituminous binders. Specifications for paving grade bitumens. *EN 125912009,* 36 (2011).
7. Velasquez, R. & Bahia, H. Critical factors affecting thermal cracking of asphalt pavements: towards a comprehensive specification. *Road Mater. Pavement Des.* **14,** 187–200 (2013).
8. Sui, C., Farrar, M. J., Harnsberger, P. M., Tuminello, W. H. & Turner, T. F. New Low-Temperature Performance-Grading Method. *J. Assoc. Asph. Paving Technol.* **2207,** 43–48 (2011).
9. Laukkanen, O.-V. Small-diameter parallel plate rheometry: a simple technique for measuring rheological properties of glass-forming liquids in shear. *Rheol. Acta* **56,** 661–671 (2017).
10. Laukkanen, O.-V., Soenen, H., Winter, H. H. & Seppälä, J. Low-temperature rheological and morphological characterization of SBS modified bitumen. *Constr. Build. Mater.* **179,** 348–359 (2018).
11. Lu, X., Uhlback, P. & Soenen, H. Investigation of bitumen low temperature properties using a dynamic shear rheometer with 4 mm parallel plates. *Int. J. Pavement Res. Technol.* **10,** 15–22 (2017).
12. Wang, D. *et al.* An Alternative Experimental Method for Measuring the Low Temperature Rheological Properties of Asphalt Binder by Using 4mm Parallel Plates on Dynamic Shear Rheometer. *J. Assoc. Asph. Paving Technol.* **2673,** 427–438 (2019).

13. Carret, J.-c. *et al.* Comparison of rheological parameters of asphalt binders obtained from bending beam rheometer and dynamic shear rheometer at low temperatures. *Road Mater. Pavement Des.* **16,** 211–227 (2015).

14. Hajj, R., Filonzi, A., Rahman, S. & Bhasin, A. Considerations for using the 4 mm Plate Geometry in the Dynamic Shear Rheometer for Low Temperature Evaluation of Asphalt Binders. *J. Assoc. Asph. Paving Technol.* **2673,** 649–659 (2019).

15. Kim, S.-S., Wysong, Z. D. & Kovach, J. Low-Temperature Thermal Cracking of Asphalt Binder by Asphalt Binder Cracking Device. *J. Assoc. Asph. Paving Technol.* **1962,** 28–35 (Jan. 2006).

16. Hammoum, F. *et al.* Experimental and Numerical Analysis of Crack Initiation and Growth in Thin Film of Bitumen. *Road Mater. Pavement Des.* **10,** 39–61 (2009).

17. Mitchell, M. R., Link, R. E., Zofka, A. & Marasteanu, M. Development of Double Edge Notched Tension (DENT) Test for Asphalt Binders. *J. Test. Eval.* **35** (2007).

18. Lee, N. K. & Hesp, S. A. M. Low-temperature fracture toughness of polyethylene-modified asphalt binders. *J. Assoc. Asph. Paving Technol.* **62,** 54–59 (1994).

19. Hecht, F. ., Pironneau, O. ., Hyaric, A. L. & Ohtsuka, K. FREEFEM++, version 2.3-3, 2008. *Softw. avaible http//www. Free. org* (2012).

20. European & Committee for Standardization. Bitumen and bituminous binders- Determination of the Fraass breaking point. *EN 125932015,* 18 (2015).

21. FEHRL. *BitVal - Analysis of Available Data for Validation of Bitumen Tests. Report on Phase 1.* tech. rep. (2006).

22. AASHTO R49-09. Standard Practice for Determination of Low- Temperature Performance Grade (PG) of Asphalt Binders. *Stand. Specif. Transp. Mater. Methods Sampl. Test.* (2013).

23. AASHTO T313-05. Standard Method of Test for Determining the Flexural Creep Stiffness of Asphalt Binder Using the Bending Beam Rheometer (BBR). *Stand. Specif. Transp. Mater. Methods Sampl. Test.* (2005).

24. Readshaw, E. E. Asphalt specifications in British Columbia for low temperature performance. *J. Assoc. Asph. Paving Technol.* **41,** 562–81 (1972).

25. Anderson, D. A. & Kennedy, T. W. Development of SHRP binder specification. *J. Assoc. Asph. Paving Technol.* **62,** 481–507 (1993).

26. AASHTO T314-12. Standard Method of Test for Determining the Fracture Properties of Asphalt Binder in Direct Tension (2015).

27. Marasteanu, M. O. & Cannone Falchetto, A. Review of experimental characterisation and modelling of asphalt binders at low temperature. *Int. J. Pavement Eng.* **19,** 279–291 (2018).

28. Hoare, T. R. & Hesp, S. A. M. Low-Temperature Fracture Testing of Asphalt Binders: Regular and Modified Systems. *J. Assoc. Asph. Paving Technol.* **1728,** 36–42 (2000).

29. Man Sze Ho, S. & Zanzotto, L. Sample Preparation for Direct Tension Testing: Improving Determination of Asphalt Binder Failure Stress and Test Repeatability. *J. Assoc. Asph. Paving Technol.* **1766,** 15–23 (2001).

30. Marasteanu, M. *et al. Investigation of Low Temperature Cracking in Asphalt Pavements National Pooled Fund Study-Phase I* tech. rep. (2007).

31. Marasteanu, M., Buttlar, W., Bahia, H., Williams, C. & Al., E. *Investigation of Low Temperature Cracking in Asphalt Pavements, National Pooled Fund Study -Phase II* tech. rep. (2012).

32. Hesp, S. A. M., Iliuta, S. & Shirokoff, J. W. Reversible Aging in Asphalt Binders. *Energy & Fuels* **21,** 1112–1121 (2007).

33. Evans, M., Marchildon, R. & Hesp, S. A. M. Effects of Physical Hardening on Stress Relaxation in Asphalt Cements. *J. Assoc. Asph. Paving Technol.* **2207,** 34–42 (2011).

34. Basu, A., Marasteanu, M. O. & Hesp, S. A. M. Time-Temperature Superposition and Physical Hardening Effects in Low-Temperature Asphalt Binder Grading. *Transp. Res. Rec. J. Transp. Res. Board* **1829,** 1–7 (2003).

35. Marasteanu, M. O., Basu, A., Hesp, S. A. & Voller, V. Time–Temperature Superposition and AASHTO MP1a Critical Temperature for Low-temperature Cracking. *Int. J. Pavement Eng.* **5,** 31–38 (2004).

36. Schröter, K., Hutcheson, S. A., Shi, X., Mandanici, A. & McKenna, G. B. Dynamic shear modulus of glycerol: Corrections due to instrument compliance. *J. Chem. Phys.* **125,** 214507 (2006).

37. Wulpi, D. J. *Understanding How Components Fail* (1985).

38. Marasteanu, M., Ghosh, D., Cannone Falchetto, A. & Turos, M. Testing protocol to obtain failure properties of asphalt binders at low temperature using creep compliance and stress-controlled strength test. *Road Mater. Pavement Des.* **18,** 352–367 (2017).

39. Griffith, A. A. The phenomena of rupture and flow in solids. *Philos. Trans. R. Soc. London. Ser. A, Contain. Pap. a Math. or Phys. Character* **221,** 163–198 (1921).

40. Inglis, C. Stresses in a Plate Due to the Presence of Cracks and Sharp Corners. *Trans. Inst. Nav. Achitects* **55,** 219–241 (1913).

41. Olard, F. & Di Benedetto, H. in *Fifth Int. RILEM Conf. Reflective Crack. Pavements* 359–366 (RILEM Publications, 2004).

42. Roy, S. D. & Hesp, S. A. M. Low-Temperature Binder Specification Development: Thermal Stress Restrained Specimen Testing of Asphalt Binders and Mixtures. *J. Assoc. Asph. Paving Technol.* **69,** 7–14 (2001).

43. Velasquez, R., Tabatabaee, H. & Bahia, H. Low Temperature Cracking Characterization of Asphalt Binders by Means of the Single-Edge Notch Bending (SENB) Test. *J. Assoc. Asph. Paving Technol.* **80,** 583–614 (2011).

44. Gauthier, G. & Anderson, D. A. Fracture mechanics and asphalt binders. *Road Mater. Pavement Des.* **7,** 9–35 (2006).

45. ASTM E399-20a. Standard Test Method for Linear-Elastic Plane-Strain Fracture Toughness of Metallic Materials. *ASTM Int.* (2020).

46. ASTM E1142-15. Standard Terminology Relating to Thermophysical Properties. *ASTM Int.* (2015).

47. Kovacs, A. J. Transition vitreuse dans les polymères amorphes. *Fortschritte der Hochpolym.* **3,** 394–507 (1963).

48. Reading, M., Luget, A. & Wilson, R. Modulated differential scanning calorimetry. *Thermochim. Acta* **238,** 295–307 (1994).

49. Reading, M., Luget, A. & Wilson, R. Modulated differential scanning calorimetry. *Thermochim. Acta* **238,** 295–307 (1994).

50. Harrison, I. R., Wang, G. & Hsu, T. C. A Differential Scanning Calorimetry Study of Asphalt Binders. *Strateg. Highw. Res. Program, Natl. Res. Counc. DC* (1992).

51. Elwardany, M. D., Planche, J.-P. & Adams, J. J. Determination of Binder Glass Transition and Crossover Temperatures using 4-mm Plates on a Dynamic Shear Rheometer. *J. Assoc. Asph. Paving Technol.* **2673,** 247–260 (2019).

52. Bahia, H. U. & Anderson, D. A. Glass transition behaviour and physical hardening of asphalt binders. *J. Assoc. Asph. Paving Technol.* **62,** 93–129 (1993).

53. Santagata, E., Tozzi, C., Baglieri, O. & Dalmazzo, D. in *Proc. RILEM Int. Symp. Bitum. Mater.* 405–411 (Springer International Publishing, 2022).

54. Yee, P., Aida, B., Hesp, S. A. M., Marks, P. & Tam, K. K. Analysis of Premature Low-Temperature Cracking in Three Ontario, Canada, Pavements. *J. Assoc. Asph. Paving Technol.* **1962,** 44–51 (2006).

55. Struik, L. C. E. *Physical aging in amorphous polymers and other materials* PhD thesis (Delft University of Technology, 1977).

56. Petersen, J. C. *et al. Binder Characterization and Evaluation Volume 4: Test Methods* 197 (1994).

57. Anderson, D. A. & Marasteanu, M. O. Physical Hardening of Asphalt Binders Relative to Their Glass Transition Temperatures. *J. Assoc. Asph. Paving Technol.* **1661,** 27–34 (1999).

58. Kriz, P., Stastna, J. & Zanzotto, L. Glass Transition and Phase Stability in Asphalt Binders. *Road Mater. Pavement Des.* **9,** 37–65 (2008).

59. Lu, X. & Isacsson, U. Laboratory study on the low temperature physical hardening of conventional and polymer modified bitumens. *Constr. Build. Mater.* **14,** 79–88 (2000).

60. Laukkanen, O.-V., Winter, H. H. & Seppälä, J. Characterization of physical aging by time-resolved rheometry: fundamentals and application to bituminous binders. *Rheol. Acta* **57,** 745–756. ISSN: 0035-4511 (Nov. 2018).

61. Baglieri, O., Dalmazzo, D., Barazia, M., Tabatabaee, H. A. & Bahia, H. U. Influence of Physical Hardening on the Low-Temperature Properties of Bitumen and Asphalt Mixtures. *Procedia - Soc. Behav. Sci.* **53,** 504–513 (2012).

62. Tabatabaee, H. A., Velasquez, R. & Bahia, H. U. Predicting low temperature physical hardening in asphalt binders. *Constr. Build. Mater.* **34,** 162–169 (2012).

63. Tozzi, C., Dalmazzo, D., Baglieri, O. & Santagata, E. Experimental Evaluation and Modeling of Physical Hardening in Asphalt Binders. *Materials (Basel).* **15,** 19 (2021).

64. Christensen, R. M. *Theory of Viscoelasticity* (Elsevier, 1982).

65. Findley, W. N., Lai, J. S., Onaran, K. & Christensen, R. M. Creep and Relaxation of Nonlinear Viscoelastic Materials With an Introduction to Linear Viscoelasticity. *J. Appl. Mech.* **44,** 364–364 (1977).

66. Tschoegl, N. W. *The Phenomenological Theory of Linear Viscoelastic Behavior* (Springer Berlin Heidelberg, Berlin, Heidelberg, 1989).

67. Marasteanu, M. O. *Inter-conversions of the linear viscoelastic functions used for the rheological characterization of asphalt binders* PhD thesis (Pennsylvania State University, 1999).

68. Schapery, R. A. Correspondence principles and a generalized J integral for large deformation and fracture analysis of viscoelastic media. *Int. J. Fract.* **25,** 195–223 (1984).

69. Simo, J. & Hughes, T. *Computational Inelasticity* (Springer-Verlag, New York, 1998).

70. Schapery, R. A. *A simple collocation method for fitting viscoelastic models to experimental data* tech. rep. (1961).

71. Cost, T. L. & Becker, E. B. A multidata method of approximate Laplace transform inversion. *Int. J. Numer. Methods Eng.* **2,** 207–219 (1970).

72. Baumgaertel, M. & Winter, H. H. Determination of discrete relaxation and retardation time spectra from dynamic mechanical data. *Rheol. Acta* **28,** 511–519 (1989).

73. Baumgaertel, M. & Winter, H. Interrelation between continuous and discrete relaxation time spectra. *J. Nonnewton. Fluid Mech.* **44,** 15–36 (1992).

74. Honerkamp, J. & Weese, J. Determination of the relaxation spectrum by a regularization method. *Macromolecules* **22,** 4372–4377 (1989).

75. Elster, C. & Honerkamp, J. Modified maximum entropy method and its application to creep data. *Macromolecules* **24,** 310–314 (1991).

76. Elster, C., Honerkamp, J. & Weese, J. Using regularization methods for the determination of relaxation and retardation spectra of polymeric liquids. *Rheol. Acta* **31,** 161–174 (1992).

77. Emri, I. & Tschoegl, N. W. Generating line spectra from experimental responses. Part I: Relaxation modulus and creep compliance. *Rheol. Acta* **32,** 311–322 (1993).

78. Tschoegl, N. W. & Emri, I. Generating line spectra from experimental responses. Part II: Storage and loss functions. *Rheol. Acta* **32,** 322–327 (1993).

79. Tschoegl, N. W. & Emri, I. Generating Line Spectra from Experimental Responses. III. Interconversion between Relaxation and Retardation Behavior. *Int. J. Polym. Mater.* **18,** 117–127 (1992).

80. Emri, I. & Tschoegl, N. W. Generating line spectra from experimental responses. Part IV: Application to experimental data. *Rheol. Acta* **33,** 60–70 (1994).

81. Kim, Y. R., LEE, H.-J. & Little, D. Fatigue characterization of asphalt concrete using viscoelasticity and continuum damage theory. *J. Assoc. Asph. Paving Technol.* **66,** 520–569 (1997).

82. Lee, H.-J. & Kim, Y. R. Viscoelastic Constitutive Model for Asphalt Concrete under Cyclic Loading. *J. Eng. Mech.* **124,** 32–40 (1998).

83. AASHTO TP 107-14. Determining the damage characteristic curve of asphalt mixtures from direct tension fatigue tests. *Stand. Specif. Transp. Mater. Methods Sampl. Test.* (2016).

84. Emri, I. Rheology of Solid Polymers. *Rheol. Rev.* **2005,** 49–100 (2005).

85. Schwarzl, F. & Staverman, A. J. Time-Temperature Dependence of Linear Viscoelastic Behavior. *J. Appl. Phys.* **23,** 838–843 (1952).

86. Markovitz, H. Superposition in rheology. *J. Polym. Sci. Polym. Symp.* **50,** 431–456 (2007).

87. Leaderman, H. *Elastic and creep properties of filamentous materials and other high polymers* PhD thesis (Massachusetts Institute of Technology, 1941).

88. Ferry, J. D. *Viscoelastic properties of polymers* 3rd (John Wiley & Sons, New York, 1980).

89. Williams, M. L., Landel, R. F. & Ferry, J. D. The Temperature Dependence of Relaxation Mechanisms in Amorphous Polymers and Other Glass-forming Liquids. *J. Am. Chem. Soc.* **77,** 3701–3707 (1955).

90. Yusoff, N. I. M., Chailleux, E. & Airey, G. D. A comparative study of the influence of shift factor equations on master curve construction. *Int. J. Pavement Res. Technol.* **4,** 324–336 (2011).

91. Chailleux, E., Ramond, G., Such, C. & de La Roche, C. A mathematical-based master-curve construction method applied to complex modulus of bituminous materials. *Road Mater. Pavement Des.* **7,** 75–92 (2006).

92. AASHTO T315-12. Standard Test Method for Determining the Rheological Properties of Asphalt Binder Using a Dynamic Shear Rheometer. *Stand. Specif. Transp. Mater. Methods Sampl. Test.* (2016).

93. Airey, G. D. Use of Black Diagrams to Identify Inconsistencies in Rheological Data. *Road Mater. Pavement Des.* **3,** 403–424 (2002).

94. Christensen, D. W. & Anderson, D. A. Interpretation of dynamic mechanical test data for paving grade asphalt cements. *J. Assoc. Asph. Paving Technol.* **61,** 67–116 (1992).

95. Chailleux, E. *et al.* Bitumen fractionation: Contribution of the individual fractions to the mechanical behavior of road binders. *Constr. Build. Mater.* **271,** 121528 (2021).

96. Baglieri, O., Tozzi, C., Dalmazzo, D., Tsantilis, L. & Santagata, E. A novel methodology for the evaluation of low temperature failure properties of asphalt binders. *Mater. Struct.* **54,** 22 (2021).

97. ASTM E456-13a. Standard Terminology Relating to Quality and Statistics. *ASTM Int.* (2017).

98. Haldar, A. & Mahadevan, S. *Probability, Reliability, and Statistical Methods in Engineering Design* (ed WILEY INDIA) (1999).

99. Chambers, J. M., Cleveland, W. S., Kleiner, B. & Tukey, P. A. *Graphical Methods for Data Analysis* (Chapman and Hall/CRC, 2018).

100. ASTM C670-15. Standard Practice for Preparing Precision and Bias Statements for Test Methods. *ASTM Int.*

101. AASHTO T240-13. Effect of Heat and Air on a Moving Film of Asphalt Binder (Rolling Thin-Film Oven Test) (2016).

102. AASHTO R28-12. Accelerated Aging of Asphalt Binder Using a Pressurized Aging Vessel (PAV) (2013).

103. Schneider, C. A., Rasband, W. S. & Eliceiri, K. W. NIH Image to ImageJ: 25 years of image analysis. *Nat. Methods* **9,** 671–675 (2012).

104. Olard, F. & Di Benedetto, H. General "2S2P1D" Model and Relation Between the Linear Viscoelastic Behaviours of Bituminous Binders and Mixes. *Road Mater. Pavement Des.* **4,** 185–224 (2003).

105. Huet, C. *Etude par une méthode d'impédance du comportement viscoélastique des matériaux hydrocarbonés* PhD thesis (Université de Paris, 1963).

106. Tschoegl, N. W., Knauss, W. G. & Emri, I. Poisson's Ratio in Linear Viscoelasticity – A Critical Review. *Mech. Time-Dependent Mater.* **6,** 3–51 (2002).

107. MATLAB. *MATLAB R2020b* 2020.

Appendix A

Determination of the discrete relaxation spectrum

The following code was implemented using MATLAB [107] to determine the relaxation spectrum of each binder. The input data used were the frequency sweep test results, shifted along the logarithmic time axis. The variable called "redomega" is the vector of the reduced angular frequencies ω, whereas the variables "g1" and "g2" are the corresponding vectors of the storage and loss modulus (G' and G"), respectively. The tolerance was fixed as 0.01, based on the data noise of the frequency sweep tests.

```
%time window
rM=1/min(redomega);
r1=1/max(redomega);
%tolerance
tol=0.01;

%pm
for N=2:50
    rm=logspace(log10(r1),log10(rM),N);
    for m=1:length(redomega)
        for n=1:length(rm)
            g1_m(m,n)=(rm(n)^2*redomega(m)^2)/(rm(n)^2*redomega(m)^2+1);
            g2_m(m,n)=(rm(n)*redomega(m))/(rm(n)^2*redomega(m)^2+1);
        end
    end
b=[g1_m;g2_m];
g_data=[g1;g2];
gm=mldivide(b,g_data);
g_mod=b*gm;
SD1=0;
SD2(N)=1/m.*(sum(abs(g_mod./g_data-1).^2));
if gm>0&SD2(N)<tol
    break
end
```

The determined spectra for the investigated unaged binders B1, B2, B3 and B4 are reported in the following Table A.1. The number of modes is indicated as N, and the relaxation Prony coefficients as ρ_i and g_i. The comparison between the experimental data and the curves reconstructed using the assessed coefficients is shown in Fig. A.1 to Fig. A.4, from which the success of the fitting can be evaluated.

Table A.1 Relaxation spectrum of unaged binders B1, B2, B3 and B4 for a reference temperature T_{ref} of $-15\,^{\circ}\mathrm{C}$

N	B1		B2		B3		B4	
	ρ_i (s)	g_i (Pa)	ρ_i (s)	g_i (Pa)	ρ_i (s)	g_i (Pa)	ρ_i (s)	g_i (Pa)
1	9.36e-05	2.00e+08	6.80e-05	1.092e+08	8.89e-05	1.32e+08	6.43e-05	1.07e+08
2	1.10e-03	2.16e+08	4.51e-04	1.094e+08	0.001	1.70e+08	6.77e-04	1.15e+08
3	1.35e-02	2.22e+08	0.003	1.32e+08	0.012	2.09e+08	0.0071	1.33e+08
4	0.16	1.90e+08	0.020	1.43e+08	0.13	2.14e+08	0.075	1.40e+08
5	1.95	1.36e+08	0.13	1.48e+08	1.51	1.72e+08	0.79	1.32e+08
6	23.38	7.90e+07	0.87	1.38e+08	17.26	1.02e+08	8.30	1.08e+08
7	280.77	3.44e+07	5.80	1.17e+08	197.09	4.01e+07	87.36	7.27e+07
8	3.37e+03	1.33e+07	38.52	9.13e+07	2.25e+03	1.06e+07	919.35	3.95e+07
9	4.04e+04	3.42e+06	255.59	5.38e+07	2.57e+04	1.56e+06	9.67e+03	1.84e+07
10	4.86e+05	5.44e+05	1.70e+03	3.29e+07	2.94e+05	1.54e+05	1.02e+05	5.82e+06
11	5.84e+06	1.32e+05	1.13e+04	1.93e+07	3.35e+06	2.36e+04	1.07e+06	9.38e+05
12			7.47e+04	8.31e+06			1.13e+07	3.01e+05
13			4.96e+05	2.90e+06				
14			3.29e+06	3.09e+05				
15			2.18e+07	3.42e+05				

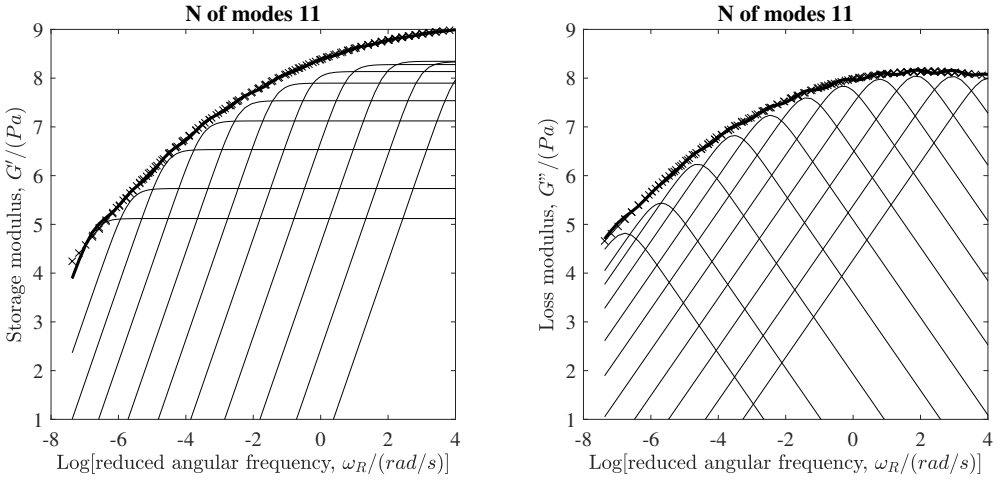

Figure A.1 Relaxation spectrum of binder B1 for a reference temperature T_{ref} of $-15\,°C$

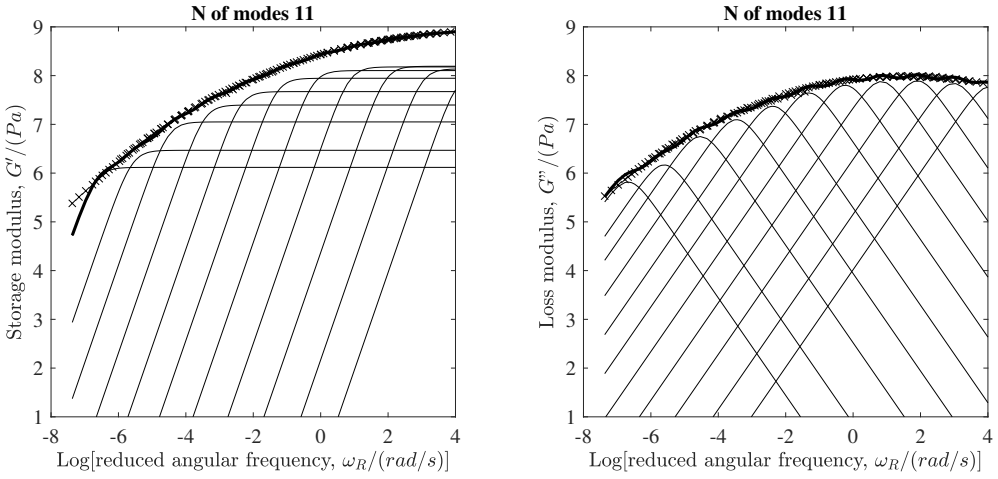

Figure A.2 Relaxation spectrum of binder B2 for a reference temperature T_{ref} of $-15\,°C$

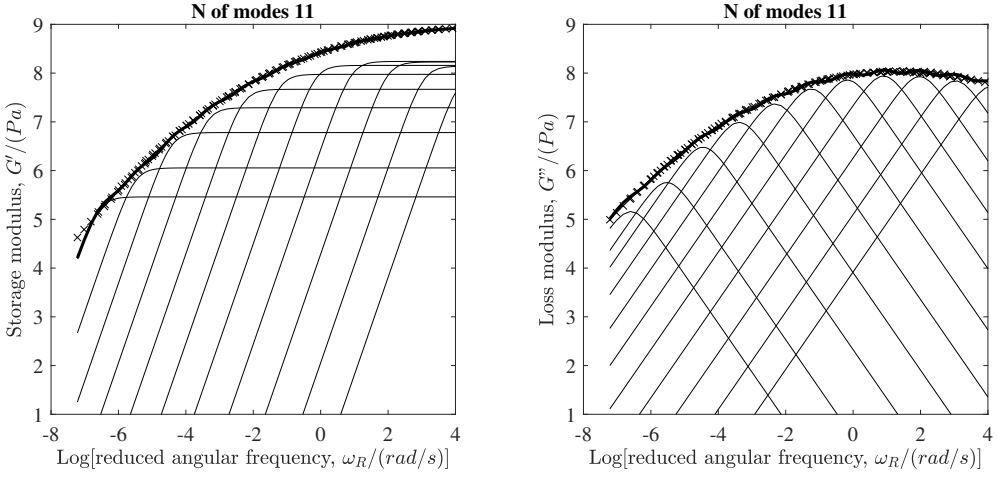

Figure A.3 Relaxation spectrum of binder B3 for a reference temperature T_{ref} of $-15\,°C$

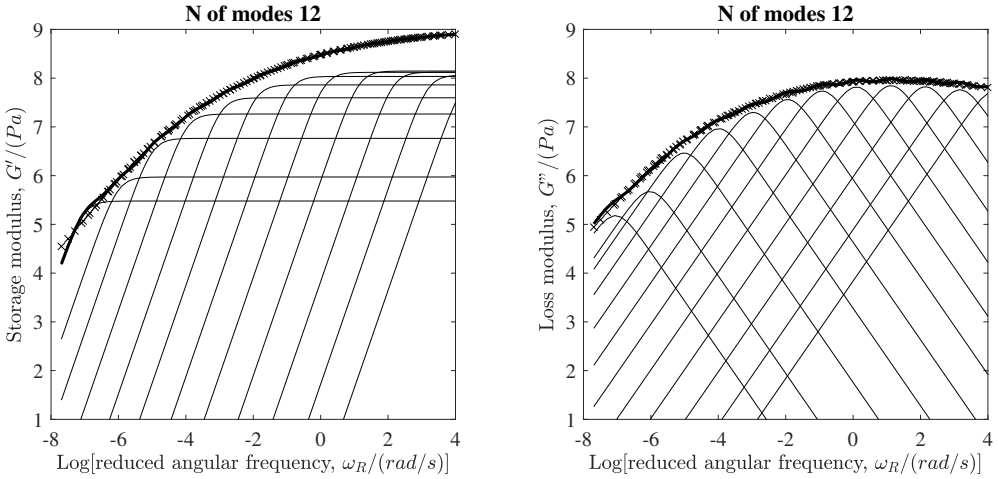

Figure A.4 Relaxation spectrum of binder B4 for a reference temperature T_{ref} of $-15\,°C$

The determined spectrum for the unaged binder B5 is reported in Table A.2. The comparison between the experimental data and the curves reconstructed using the assessed coefficients is shown in Fig. A.5.

Table A.2 Relaxation spectrum of unaged binder B5 for a reference temperature T_{ref} of $-15\,°C$

N	ρ_i (s)	g_i (Pa)
1	3.51e-05	4.79e+07
2	2.87e-04	5.63e+07
3	0.0024	7.82e+07
4	0.019	1.01e+08
5	0.16	1.29e+08
6	1.29	1.54e+08
7	10.57	1.73e+08
8	86.49	1.77e+08
9	708.05	1.25e+08
10	5.80e+03	9.03e+07
11	4.74e+04	6.38e+07
12	3.88e+05	3.38e+07
13	3.18e+06	5.96e+06
14	2.60e+07	5.38e+06

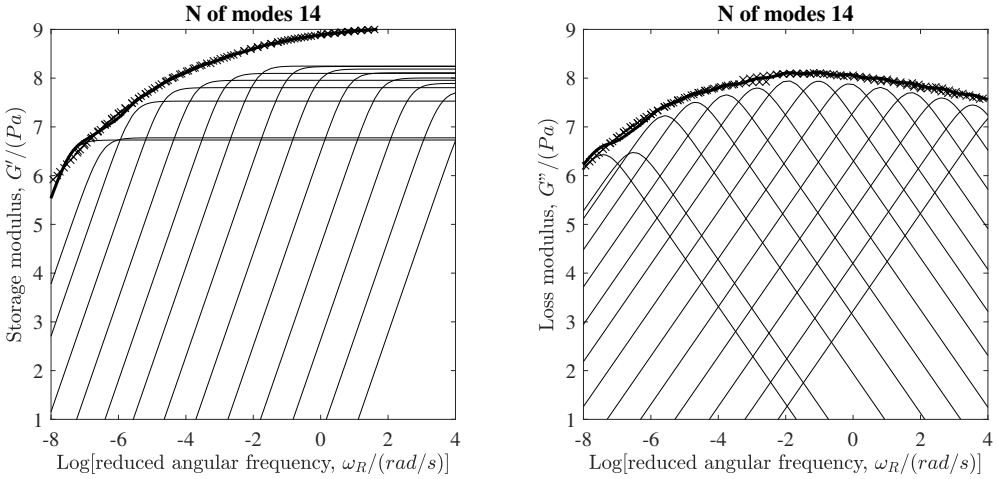

Figure A.5 Relaxation spectrum of binder B5 for a reference temperature T_{ref} of $-15\,°C$

The determined spectra for the RTFOT aged binders B1, B2, B3 and B4 are reported in the following Table A.3, whereas Table A.4 refers to the same materials in their PAV aged condition. The comparison between the experimental data and the curves reconstructed using the assessed coefficients is shown in Fig. A.6 to Fig. A.9 for the RTFOT binders and Fig. A.10 to Fig. A.13 for the PAV binders.

Table A.3 Relaxation spectrum for RTFOT aged materials

N	B1		B2		B3		B4	
	ρ_i (s)	g_i (Pa)	ρ_i (s)	g_i (Pa)	ρ_i (s)	g_i (Pa)	ρ_i (s)	g_i (Pa)
1	2.97e-05	1.49e+08	2.08e-05	1.02e+08	7.53e-05	1.12e+08	6.37e-05	8.57e+07
2	3.87e-04	1.72e+08	2.71e-04	1.28e+08	1.10e-03	1.51e+08	6.17e-04	9.14e+07
3	5.00e-03	1.87e+08	3.50e-03	1.54e+08	1.54e-02	1.87e+08	6.00e-03	1.05e+08
4	0.07	1.71e+08	4.59e-02	1.61e+08	0.22	1.85e+08	5.78e-02	1.10e+08
5	0.86	1.34e+08	0.60	1.40e+08	3.16	1.33e+08	0.56	1.06e+08
6	11.09	8.64e+07	7.80	9.88e+07	45.16	6.65e+07	5.42	9.01e+07
7	144.41	4.42e+07	101.65	5.33e+07	646.10	2.19e+07	52.47	6.75e+07
8	1.88e+03	1.94e+07	1.32e+03	2.13e+07	9.24e+03	4.60e+06	507.98	4.19e+07
9	2.45e+04	6.87e+06	1.73e+04	6.28e+06	1.32e+05	5.25e+05	4.92e+03	2.14e+07
10	3.18e+05	1.50e+06	2.25e+05	1.09e+06	1.89e+06	7.77e+04	4.76e+04	8.45e+06
11	4.14e+06	4.58e+05	2.93e+06	2.50e+05			4.61e+05	1.74e+06
12							4.46e+06	7.71e+05

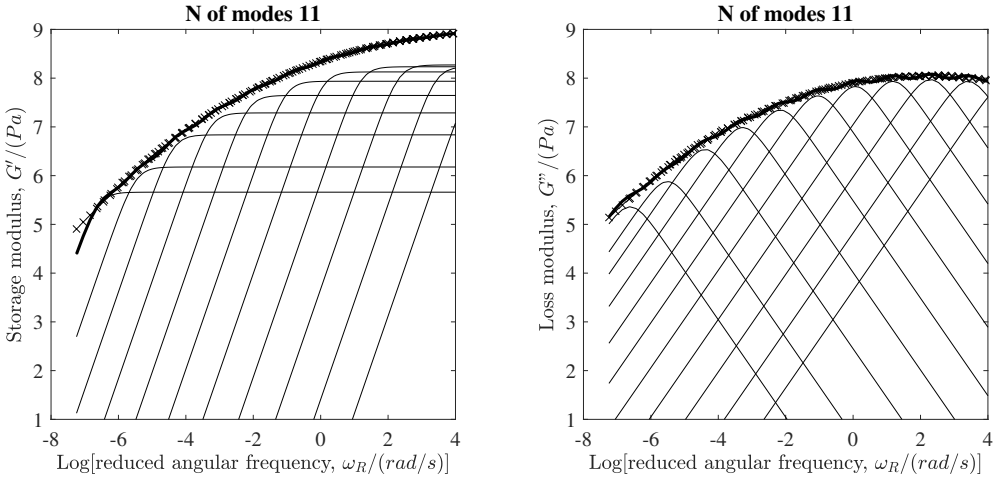

Figure A.6 Relaxation spectrum of RTFOT binder B1 for a reference temperature T_{ref} of −15 °C

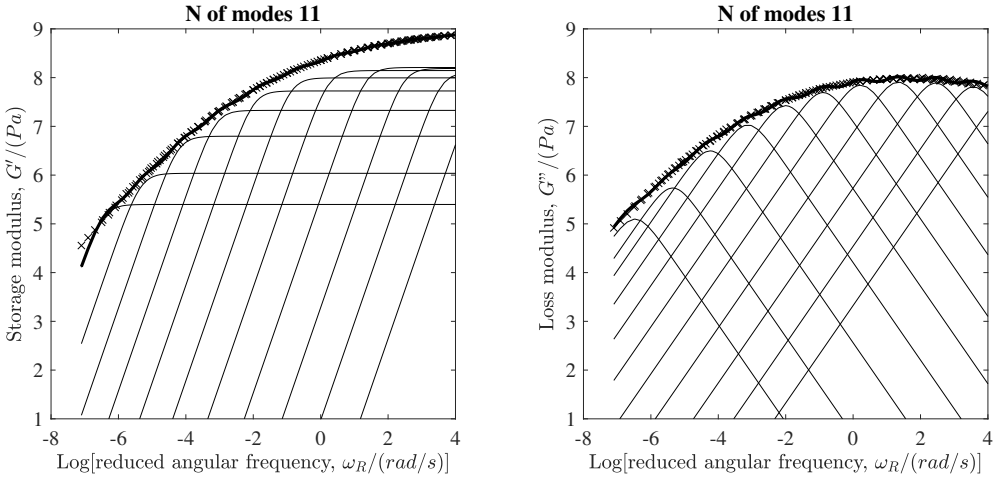

Figure A.7 Relaxation spectrum of RTFOT binder B2 for a reference temperature T_{ref} of −15 °C

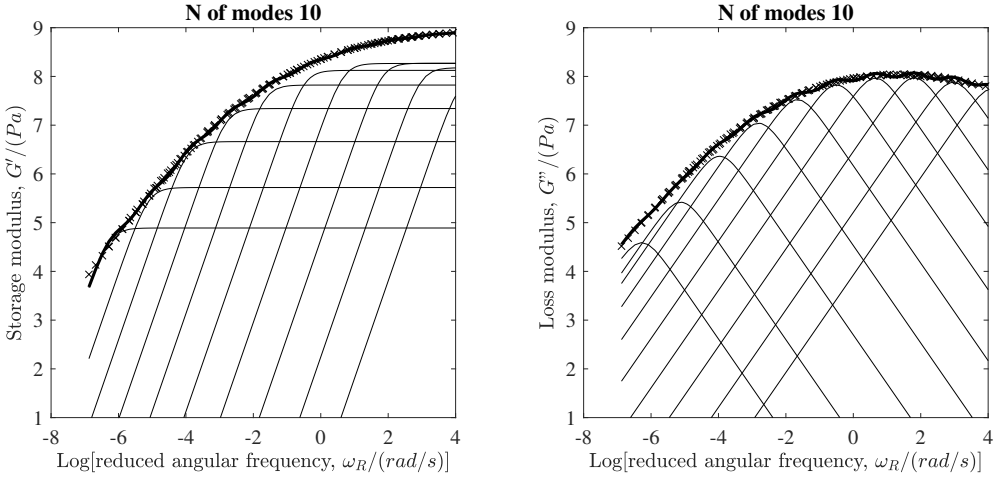

Figure A.8 Relaxation spectrum of RTFOT binder B3 for a reference temperature T_{ref} of −15 °C

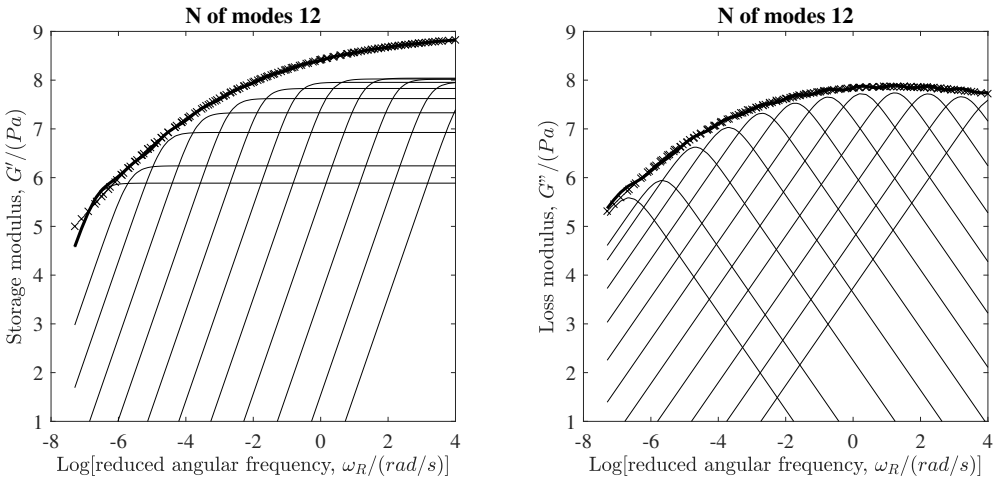

Figure A.9 Relaxation spectrum of RTFOT binder B4 for a reference temperature T_{ref} of -15 °C

Table A.4 Relaxation spectrum for PAV aged materials

N	**B1**		**B2**		**B3**		**B4**	
	ρ_i (s)	g_i (Pa)	ρ_i (s)	g_i (Pa)	ρ_i (s)	g_i (Pa)	ρ_i (s)	g_i (Pa)
1	1.01e-04	1.69e+08	2.18e-05	9.91e+07	7.72e-05	1.08e+08	6.57e-05	1.11e+08
2	0.0012	1.74e+08	2.34e-04	1.19e+08	9.08e-04	1.38e+08	7.13e-04	1.19e+08
3	0.014	1.76e+08	2.50e-03	1.42e+08	1.07e-02	1.69e+08	7.70e-03	1.36e+08
4	0.18	1.54e+08	2.70e-02	1.50e+08	0.13	1.73e+08	8.39e-02	1.42e+08
5	1.99	1.20e+08	0.29	1.39e+08	1.48	1.44e+08	0.91	1.30e+08
6	23.59	8.14e+07	3.11	1.15e+08	17.43	9.42e+07	9.88	1.08e+08
7	279.70	4.64e+07	33.39	7.61e+07	205.16	4.65e+07	107.17	7.40e+07
8	3.31e+03	2.56e+07	358.55	4.05e+07	2.41e+03	1.94e+07	1.16e+03	4.41e+07
9	3.93e+04	1.26e+07	3.85e+03	2.22e+07	2.84e+04	6.02e+06	1.26e+04	2.58e+07
10	4.66e+05	3.86e+06	4.13e+04	9.97e+06	3.35e+05	1.13e+06	1.37e+05	1.20e+07
11	5.53e+06	2.14e+06	4.44e+05	2.58e+06	3.39e+06	2.88e+05	1.49e+06	3.16e+06
12			4.76e+06	1.32e+06			1.61e+07	1.53e+06

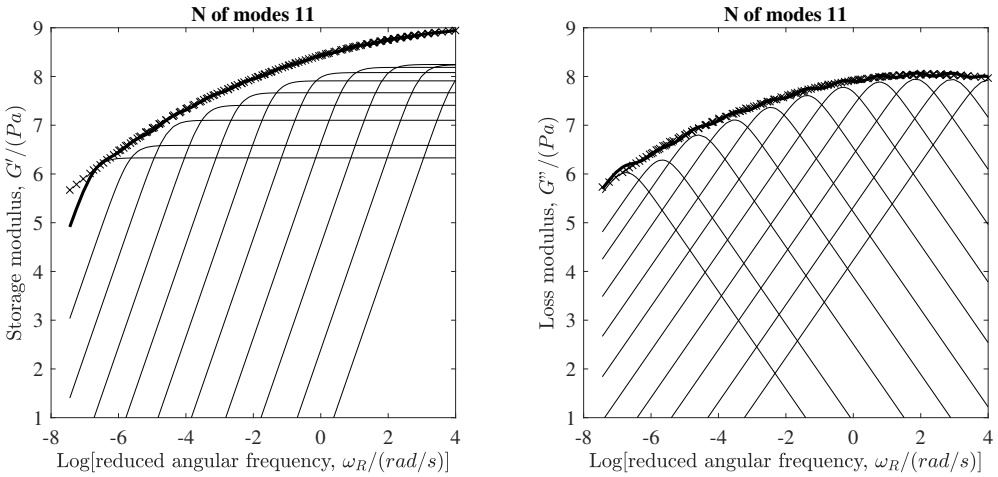

Figure A.10 Relaxation spectrum of PAV binder B1 for a reference temperature T_{ref} of -15 °C

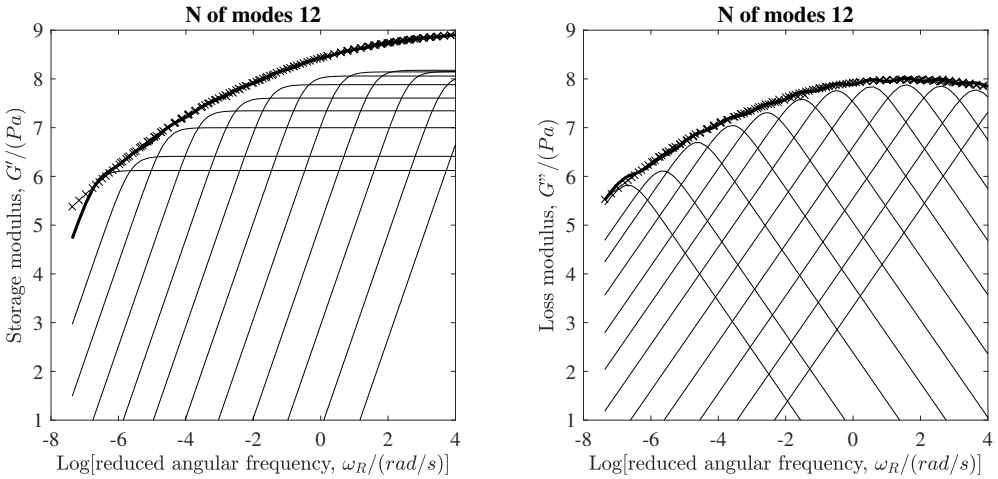

Figure A.11 Relaxation spectrum of PAV binder B2 for a reference temperature T_{ref} of -15 °C

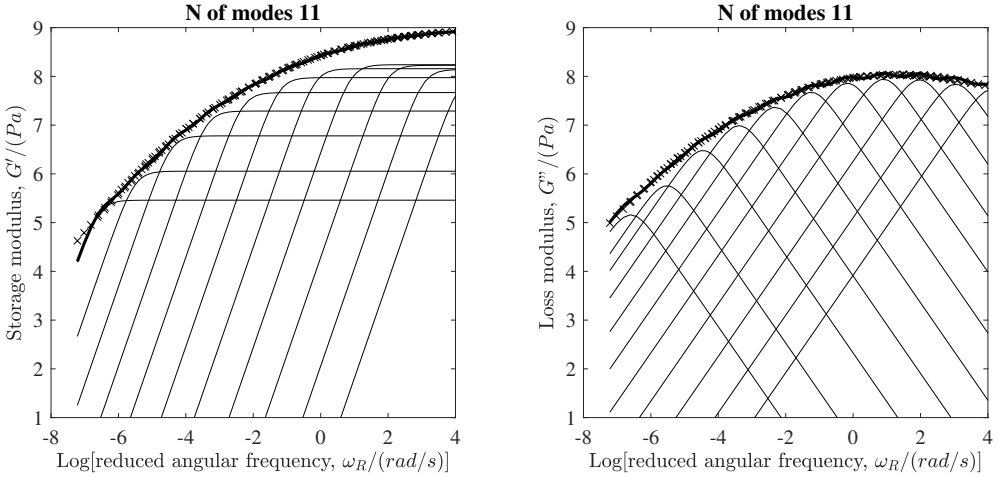

Figure A.12 Relaxation spectrum of PAV binder B3 for a reference temperature T_{ref} of -15 °C

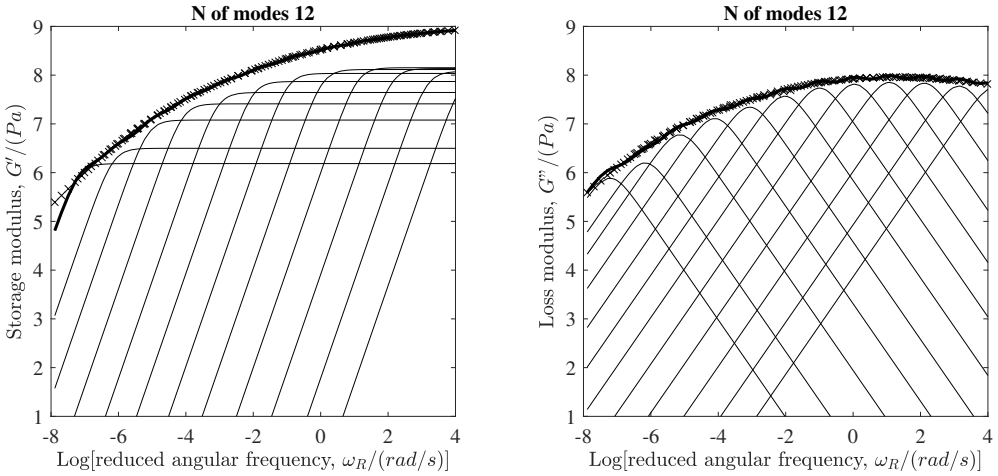

Figure A.13 Relaxation spectrum of PAV binder B4 for a reference temperature T_{ref} of -15 °C

Appendix B

Statistical distributions of results

The box plots of the sample X_1, X_2, X_3 and X_4 of chapter 5 are shown in Figs. B.1 to B.4.

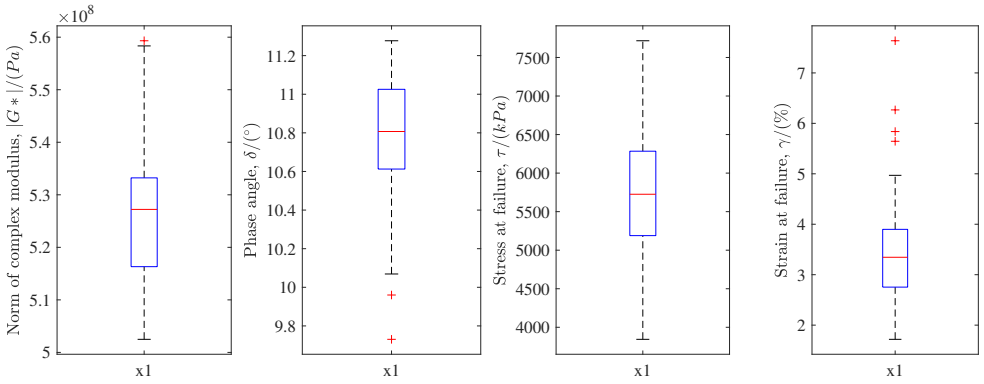

Figure B.1 Box plot of sample X_1

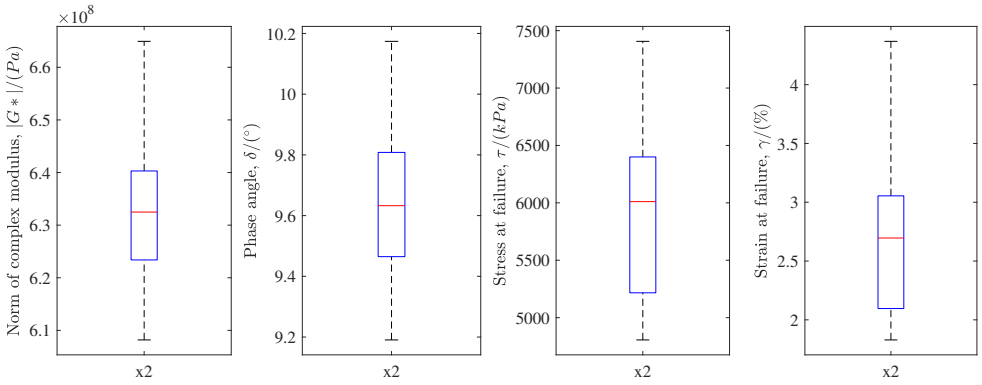

Figure B.2 Box plot of sample X_2

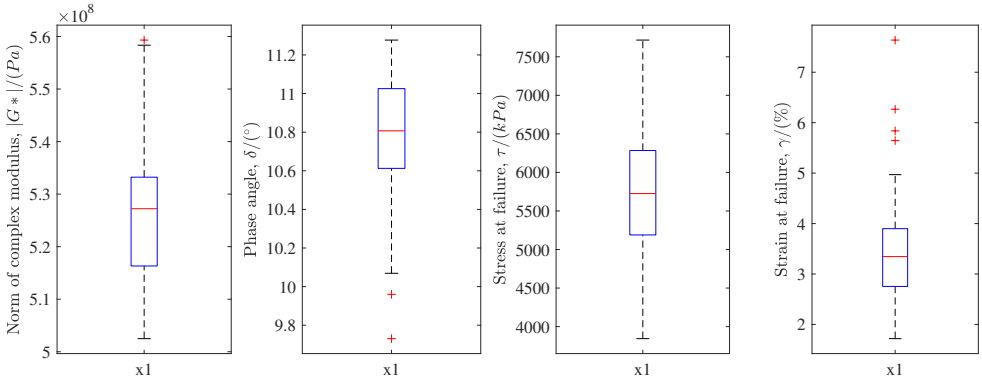

Figure B.3 Box plot of sample X_3

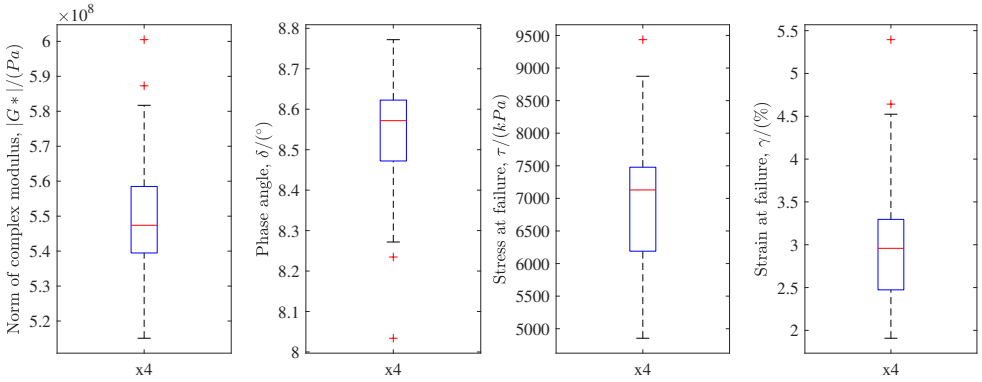

Figure B.4 Box plot of sample X_4

The CDF referred to the sample X_1, X_2, X_3 and X_4 for the variables $|G^*|$, δ and τ_F are reported in the following figures.

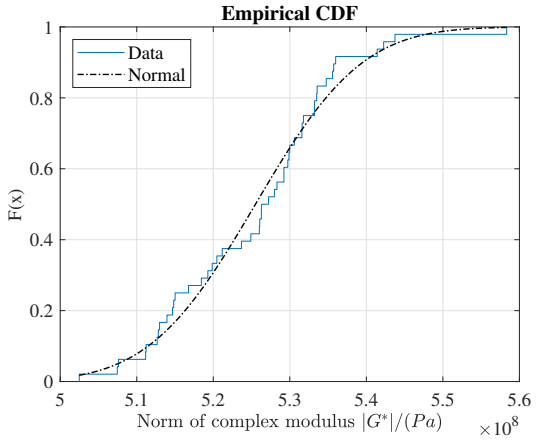

(a) Norm of complex modulus

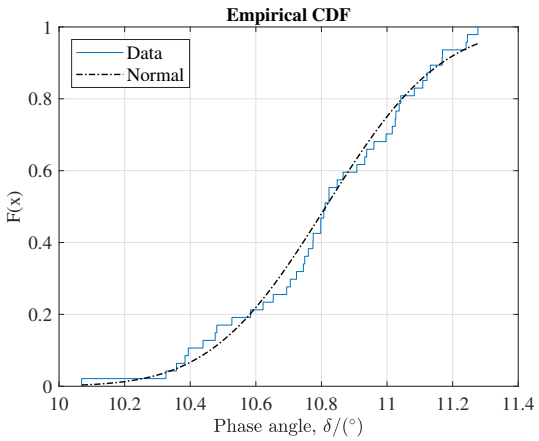

(b) Phase angle

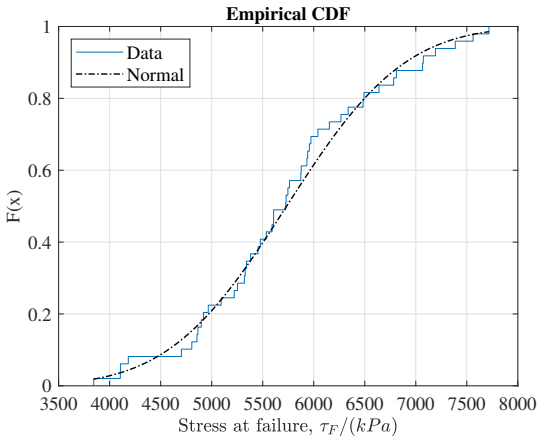

(c) Failure stress

Figure B.5 CDF for sample X_1

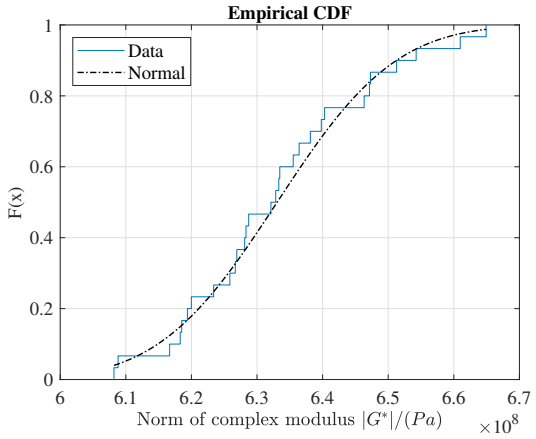

(a) Norm of complex modulus

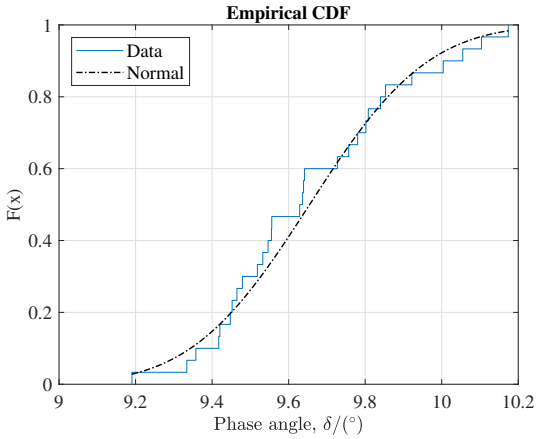

(b) Phase angle

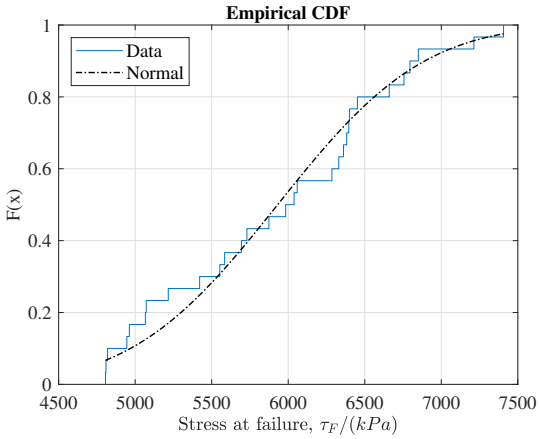

(c) Failure stress

Figure B.6 CDF for sample X_2

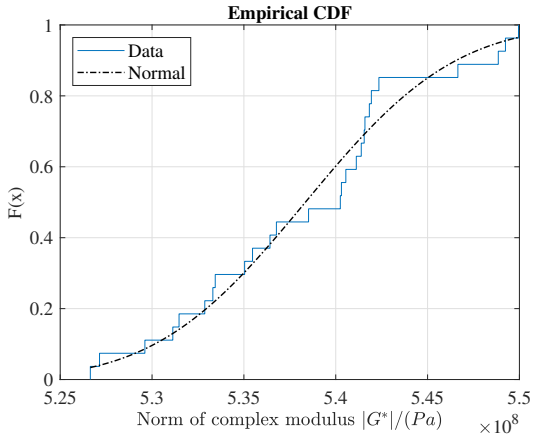

(a) Norm of complex modulus

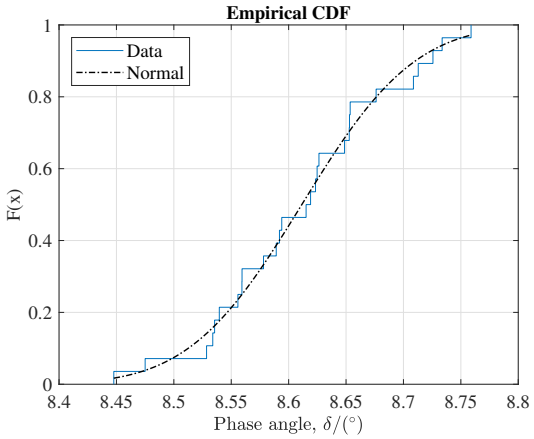

(b) Phase angle

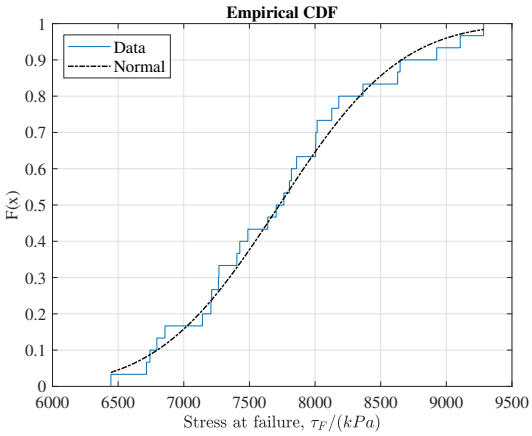

(c) Failure stress

Figure B.7 CDF for sample X_3

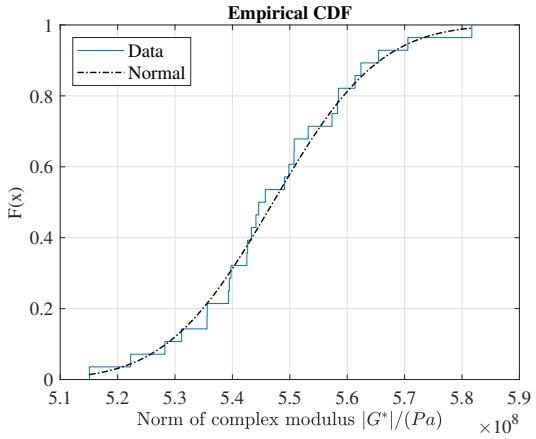

(a) Norm of complex modulus

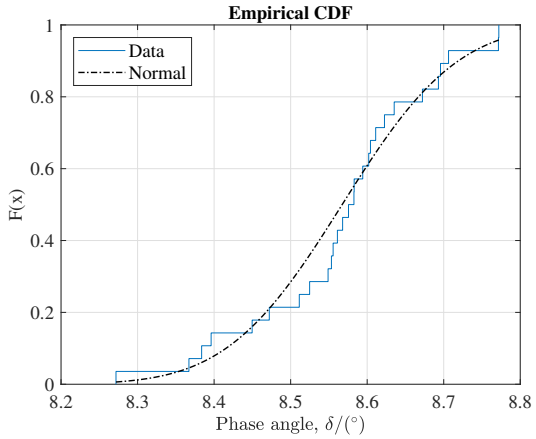

(b) Phase angle

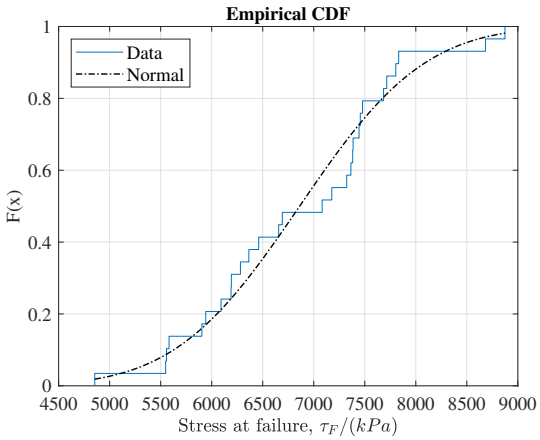

(c) Failure stress

Figure B.8 CDF for sample X_4

The probability plots referred to the sample X_1, X_2, X_3 and X_4 for the variables $|G^*|$, δ and τ_F are reported in the following figures.

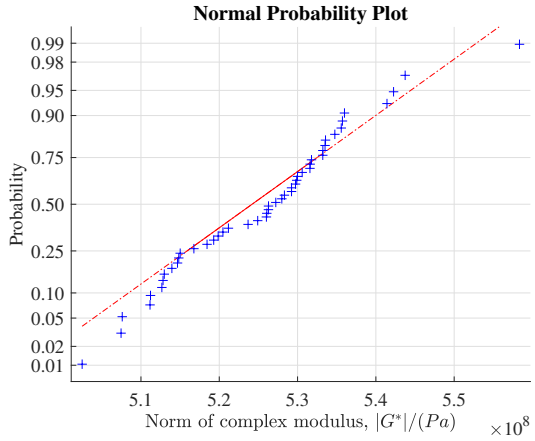

(a) Phase angle

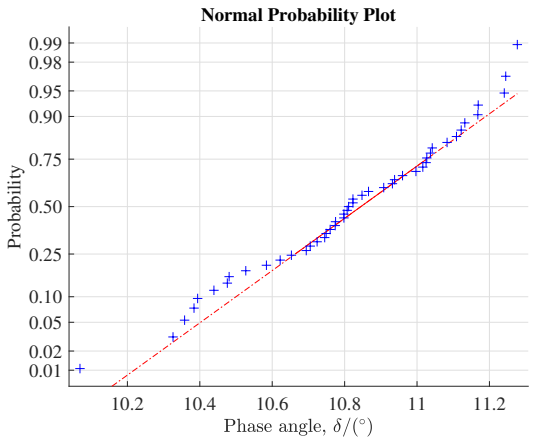

(b) Norm of complex modulus

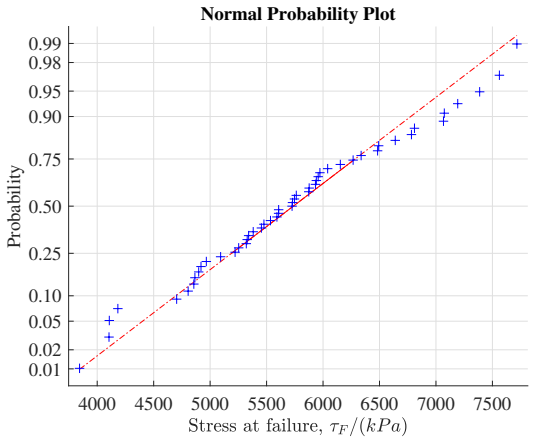

(c) Failure stress

Figure B.9 Probability plots for sample X_1

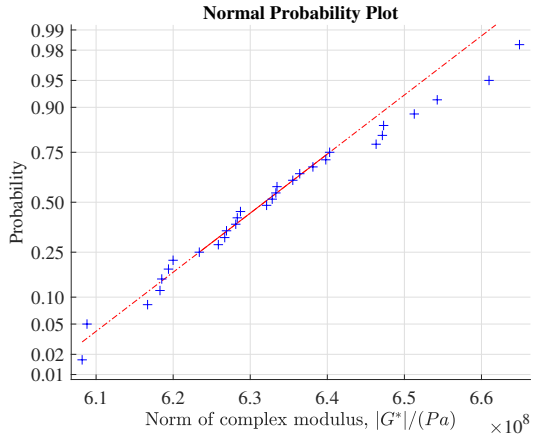

(a) Phase angle

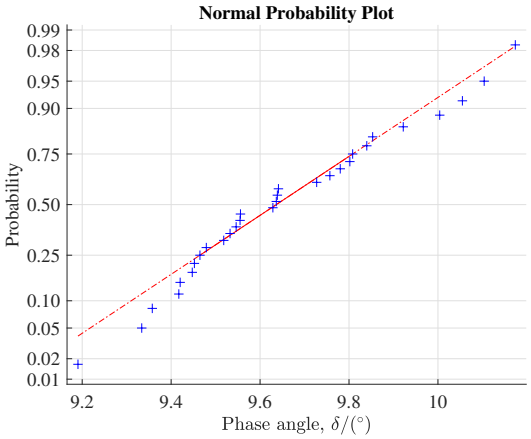

(b) Norm of complex modulus

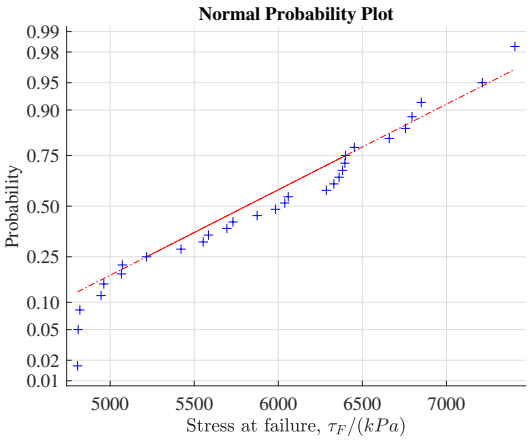

(c) Failure stress

Figure B.10 Probability plots for sample X_2

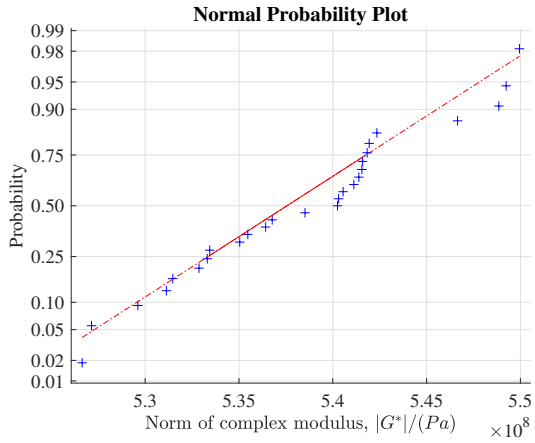

(a) Phase angle

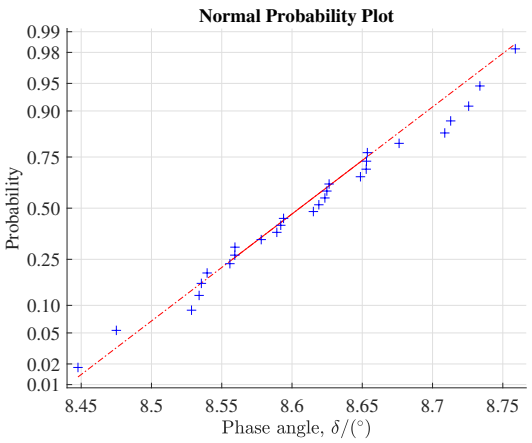

(b) Norm of complex modulus

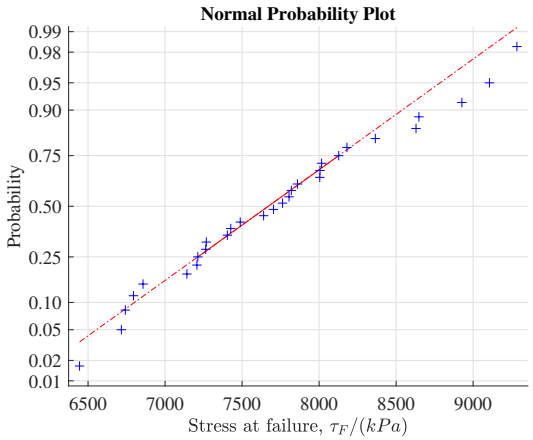

(c) Failure stress

Figure B.11 Probability plots for sample X_3

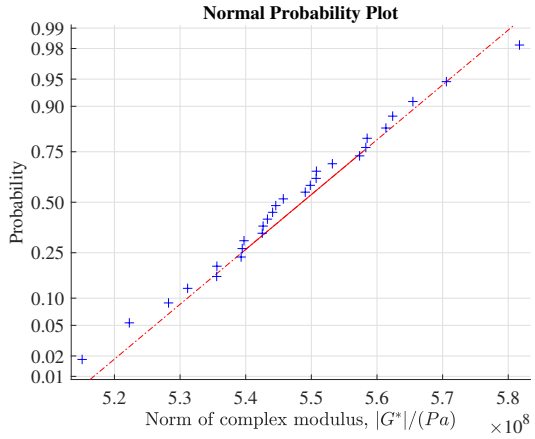

(a) Phase angle

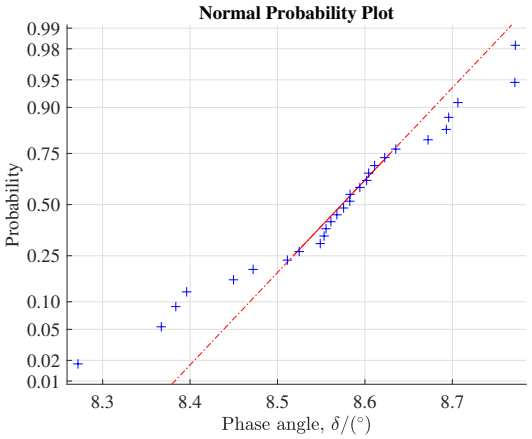

(b) Norm of complex modulus

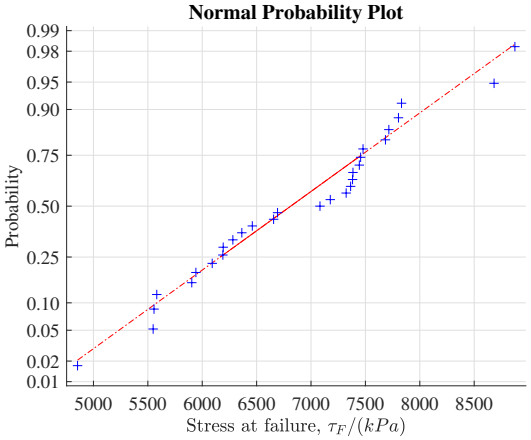

(c) Failure stress

Figure B.12 Probability plots for sample X_4